Strangeness Photoproduction Polarization Observables from g8

C A Paterson, D G Ireland, K Livingston and B McKinnon[*]

SUPA, School of Physics and Astronomy,

University of Glasgow, Glasgow G12 8QQ, United Kingdom

Abstract

This analysis note presents measurements of several polarization observables for the reactions $\overrightarrow{\gamma}p \to K^+\Lambda^0$ and $\overrightarrow{\gamma}p \to K^+\Sigma^0$. The data were collected during the g8b experimental run, using a linearly polarized photon beam, resulting in measurements in the energy range $1.71\,\text{GeV} < W < 2.19\,\text{GeV}$ and angular range $-0.75 < \cos\theta_K < +0.85$. The observables extracted in the analysis for both reactions are: photon beam asymmetry Σ, target asymmetry T and the double polarization observables O_x and O_z. All results will increase the precision of the current world datasets, and will extend the angular and energy coverage.

[*] David.Ireland@glasgow.ac.uk

CONTENTS

56 **I.   INTRODUCTION**

57   This note describes in detail the analysis of the reactions $\vec{\gamma}p \rightarrow K^+\Lambda$ and $\vec{\gamma}p \rightarrow K^+\Sigma^0$
58 in CLAS for data taken during the g8b run period, where the hyperon is reconstructed
59 from the missing mass recoiling against the kaon. The methods used to correctly identify
60 the particles of interest in CLAS, and the procedures used to extract the various polar-
61 ization observables are described. The handling of the photon polarization will also be
62 described, including an overview of how it was calculated and then used in the analysis.
63 Results will then be presented for the polarization observables $\{\Sigma, T, O_x, O_z\}$ as angu-
64 lar distributions ($\cos \theta_K$) for bins in hadronic mass W, and as W distributions for bins in
65 $\cos \theta_K$.

66   In this analysis, the polarization observables to be published have been extracted using
67 an event-by-event maximum likelihood method. However, many of the initial checks and
68 tests were carried out using a binned fitting methodology. A detailed description of these
69 two methods is included.

70   **A.   Formalism**

71   The coordinate system and kinematical variables used in the description of kaon pho-
72 toproduction are shown for the centre-of-mass reference frame in figure 1. Several coor-
73 dinate systems are commonly used in the literature. The *unprimed* coordinate system is
74 chosen where the z-axis is orientated along the momentum axis of the incoming photon;
75 the *primed* system is where the z-axis is orientated along the direction of the outgoing K^+
76 meson. In terms of unit vectors:

$$\hat{z} = \frac{\vec{k}}{\left|\vec{k}\right|}; \quad \hat{y} = \frac{\vec{k} \times \vec{q}}{\left|\vec{k} \times \vec{q}\right|}; \quad \hat{x} = \hat{y} \times \hat{z} \tag{1}$$

$$\hat{z}' = \frac{\vec{q}}{\left|\vec{q}\right|}; \quad \hat{y}' = \hat{y}; \quad \hat{x}' = \hat{y}' \times \hat{z}' \tag{2}$$

77   Note that one frame can transform into another by a simple rotation of θ_K^{CM} about the
78 y-axis. For this analysis the unprimed coordinate system was chosen to be consistent
79 with previous CLAS measurements [1].

⁸⁰   The differential cross section for the reaction, assuming that photon and recoil polar-

⁸¹ ization can be determined reads

$$
\frac{d\sigma}{d\Omega} \equiv \sigma\left(\phi, \cos\theta_x, \cos\theta_y, \cos\theta_z\right) = \sigma_0 \{ 1 - P^\gamma \Sigma \cos 2\phi \\
- \alpha \cos\theta_x P^\gamma O_x \sin 2\phi \\
+ \alpha \cos\theta_y P - \alpha \cos\theta_y P^\gamma T \cos 2\phi \\
- \alpha \cos\theta_z P^\gamma O_z \sin 2\phi \},
\tag{3}
$$

⁸² where σ_0 represents the unpolarised cross-section, P^γ is the photon polarization, ϕ is the

⁸³ azimuthal angle between the scattering plane and the photon polarization direction, α is

⁸⁴ the Λ weak decay asymmetry and everything else is a polarization observable.

⁸⁵   The variation of the cross section as a function of the variables $\phi, \cos\theta_x, \cos\theta_y, \cos\theta_z$

⁸⁶ allows one to extract the observables Σ, O_x, O_z, T and P. Use of asymmetries further

⁸⁷ allows one to supress the effects of experimental acceptance.
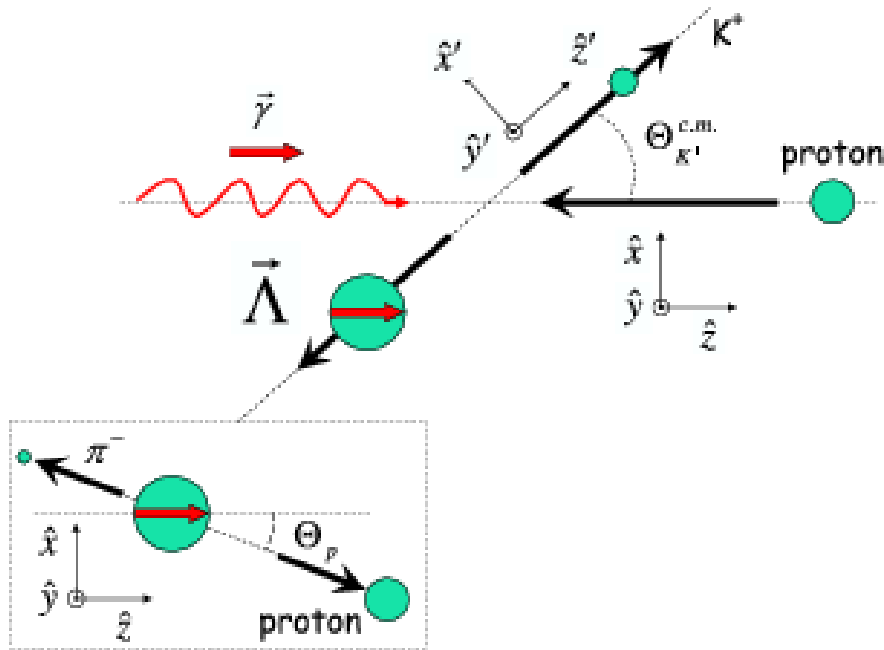

Figure 1. Kinematics of the $\gamma p \rightarrow K\Lambda$ reaction. Picture taken from [1].

₈₈   **B.   Experiment Overview**

₈₉   The g8b experiment used the coherent bremsstrahlung facility to produce linearly po-

₉₀ larized photons [2]. A schematic is shown in figure 2. This technique produces a "coher-

₉₁ ent peak" at a selected position in the photon energy spectrum, where the photons have

₉₂ a high degree of linear polarization. Five separate coherent peak positions were selected

₉₃ to span the required photon energy range. Full details are given in section III.

₉₄   **C.   Synopsis**

₉₅   The note is organised as follows: event selection (section II), discussion of photon

₉₆ beam polarization (section III) and observable extraction (section IV). Appendices con-

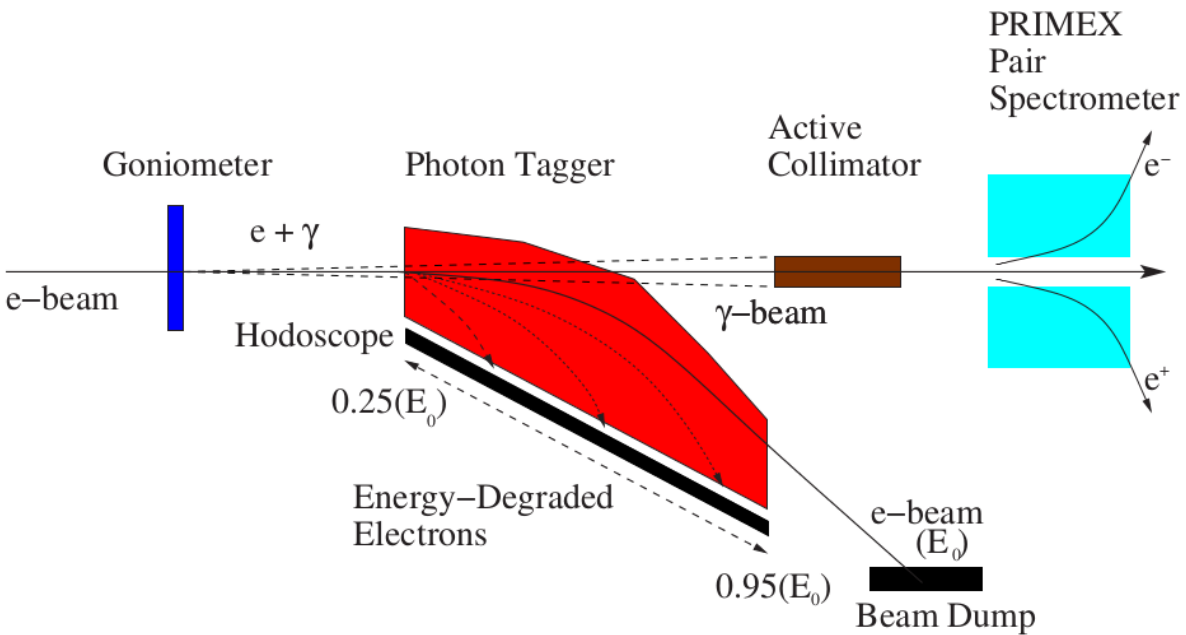₉₇ taining additional detail relevant to the analysis are included for completeness.

Figure 2. Schematic layout of coherent bremsstrahlung facility within Hall B [2]. The incident electron beam scatters off a diamond held by the goniometer to produce linearly polarized photons. The energy degraded electrons are bent on to the tagger hodoscope while the photons pass through the active collimator.

98 **II.   DATA ANALYSIS: EVENT SELECTION**

99   This section describes in detail the event selection process used to identify the follow-
100 ing reactions in CLAS:

$$\vec{\gamma} p \to K^+ \Lambda \to K^+ p \pi^-$$

$$\vec{\gamma} p \to K^+ \Sigma^0 \to K^+ \gamma \Lambda \to K^+ \gamma p \pi^-$$

101 In these reactions the Λ decays into a p and π^- with a 64% branching ratio, while the
102 Σ^0 radiatively decays decays into a Λ. The methods used to correctly identify the par-
103 ticles of interest in CLAS will be described, focusing on a semi-inclusive determination
104 of the reactions through the identification of the K^+ and decay p. The Λ and Σ^0 are then
105 reconstructed from the K^+ missing mass before the final yields are extracted. All proce-
106 dures and cuts used in the particle identification are discussed in the order in which they
107 were used in the event selection. The complete analysis of the g8b data set was carried
108 out on five different photon energy ranges, corresponding to the coherent peak settings,
109 as well as on unpolarized data that was taken periodically throughout the run. The fol-
110 lowing sections will detail the analysis of the 1.5 GeV linearly polarized photon data set.
111 The cuts and procedures used for this analysis, however, are the same for all the photon
112 settings.

113   After the data was calibrated and cooked, a selection of runs based on quality control
114 criteria was produced. These "golden" runs are those which the g8b group have flagged
115 as being of sufficient quality (such as stable run conditions during data taking and the
116 effectiveness of applied calibrations). The full list is given in A.

117   **A.   Photon Energy bins (Coherent Peak Settings)**

118   This analysis is carried out for five coherent peak positons in the data. In order to
119 achieve this, the first cut made in the analysis is one that bins the data in photon energy.
120 The polarised photons for each setting are found in a 200 MeV wide bin with an upper
121 limit at the coherent edge position. The nominal bins are defined in table 1. During data
122 taking the coherent edge position drifts by up to $\sim$ 50 MeV, resulting in an overlap region
123 (in W) between settings. These overlaps were studied, and are discussed in section III.

Setting Label	Photon Energy Range (GeV)	
	Lower Limit	Upper Limit
1300	1.1	1.3
1500	1.3	1.5
1700	1.5	1.7
1900	1.7	1.9
2100	1.9	2.1

Table I. The definition of the nominal coherent peak settings

B.   Initial Event Filter

For the g8b run a fairly loose trigger condition was used during data acquisition, which accepted a variety of particle events that could be used in multiple proposed analyses. The end result of this was a data set of 11,475 files totalling ~ 25 TBytes of disk space, of which $K - \Lambda/\Sigma^0$ events contribute only a small percentage. This data was stored on the Jlab tape silo and simply retrieving it in its original form for analysis would not only use up a large amount of disk space but would also be very time consuming. Instead the dataset was skimmed using the ROOTBEER software package [3], into Data Summary Tapes (DSTs) that were specific to the $K^+\Lambda$ and $K^+\Sigma^0$ reaction channels. These skims reduced the data set down to $\sim$2% of the original size.

Hit Multiplicity and TOF Mass Cuts

The filtering process initially required a loose determination of the reaction products that identify the $K^+\Lambda$ and $K^+\Sigma^0$ channels. The efficiency of CLAS for detecting photons of $\sim$70MeV radiated from the Σ^0 is low, so although the possibility of a photon being in the data was retained it was not explicitly required for the identification of the Σ^0. In addition the field settings used for g8b meant that the acceptance within CLAS for the negatively charged pion is lower than for the positively charged kaon and proton. For this reason events with a kaon and a proton only were chosen as the best way of selecting the hyperon events, with the pion being determined from the missing mass

143 $MM(pK^+)$. However, if a negatively charged pion is detected we retain its momentum,
144 thereby allowing for the possibility of analysing these 3-track events.

145   The first step in the filtering was to only select events where 2, 3 or 4 particles were
146 recorded in CLAS along with a valid tagger hit. Once an event had satisfied these criteria
147 an initial identification of the particles was made using the mass calculated from the
148 drift chambers and time-of-flight system (TOF mass). The following criteria were used to
149 make the initial identification:

150   • Any particles with mass zero and charge zero were identified as photons

151   • All particles with non-zero mass and zero charge were removed

152   • All particles of non-zero charge must have a valid hit in the drift chamber and either
153   TOF or EC

154   • For positive charge particles the following TOF mass windows were used for iden-
155   tification:

156   − $0.1 < M^2 < 0.49 \, GeV^2/c^4$ for K^+
157   − $0.49 < M^2 < 1.44 \, GeV^2/c^4$ for protons

158   • For negative charge particles the following TOF mass windows were used for iden-
159   tification:

160   − $0.0 < M^2 < 0.1 \, GeV^2/c^4$ for π^-

161 Events were then retained which contained a proton and a kaon, and one or no pions as
162 well as one or no photons (from the Σ decay).

163   Figure 3 shows the TOF mass for positively charged particles, along with the hit mul-
164 tiplicity for events which satisfy the initial selection criteria. As can be seen only events
165 with either 2, 3 or 4 particles were retained, with the number of events decreasing as the
166 number of requested particles increases. From figure 3 it is evident that the proton can
167 be reasonably identified at this stage with a simple mass cut. It should be noted that the
168 TOF mass resolution increases at lower momentum as shown in figure 4. However, it is
169 clear that the mass window used in the proton selection is large enough so that no good
170 proton events are discarded, even at low momentum.
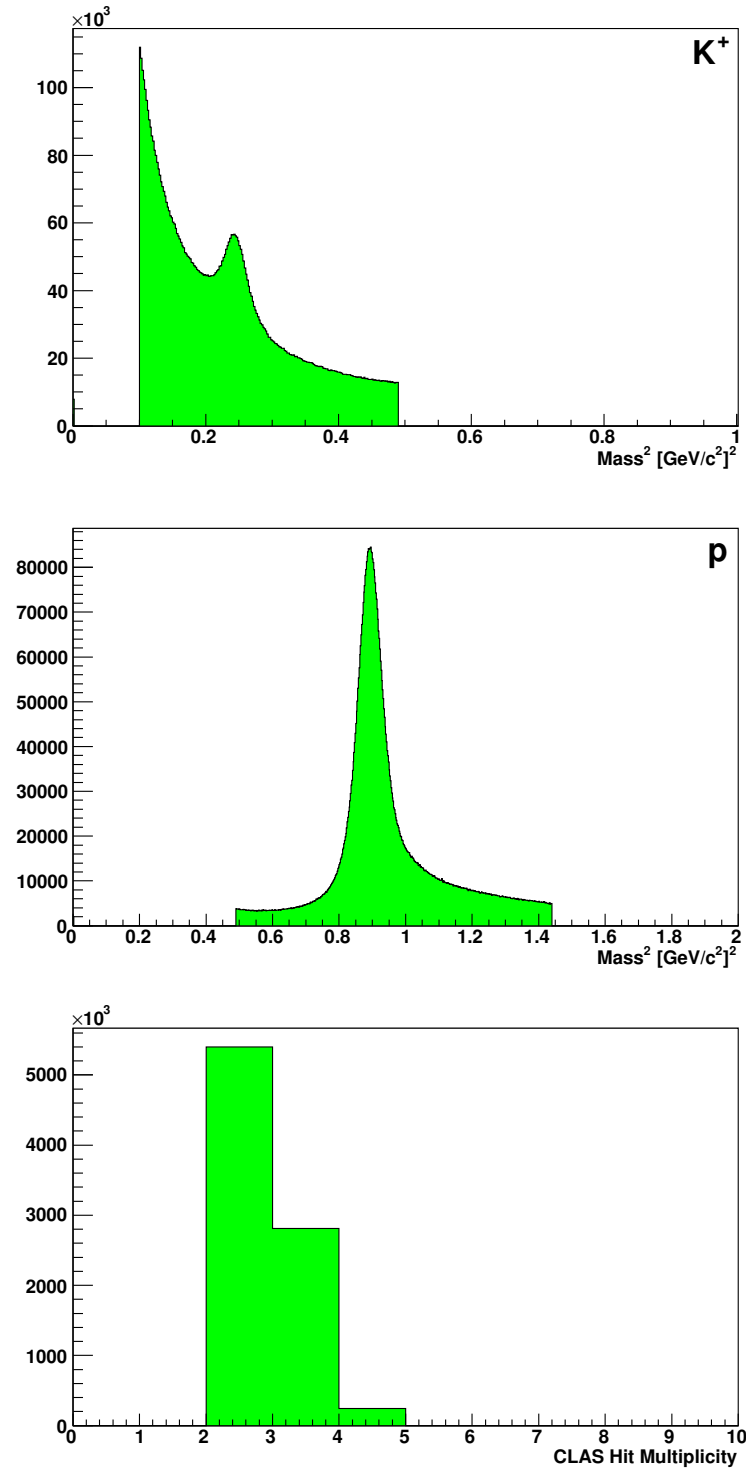
Figure 3. TOF mass of K^+ (top left) and proton (top right) after simple selection criteria on number of particle events allowed. The multiplicity of hits (bottom) shows that only 2, 3 or 4 particle events are retained at this stage.
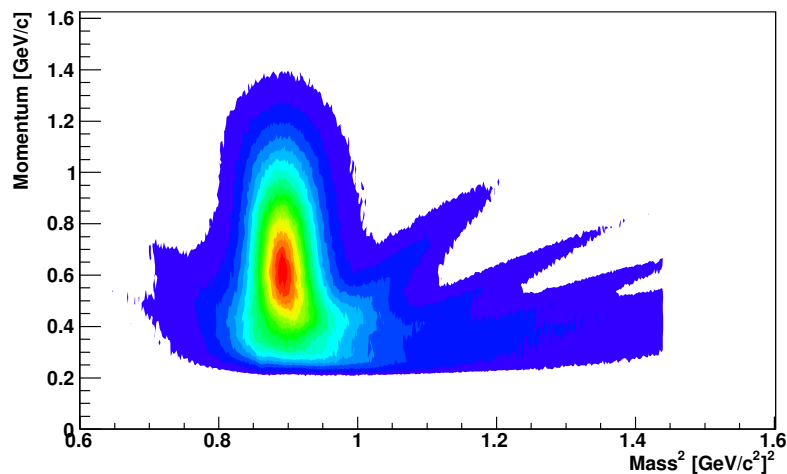
Figure 4. Mass vs Momentum in the region of the proton TOF mass. Despite the TOF mass resolution increasing at lower momenta, it is still well within the initial proton mass selection criteria of $0.49 < M(p) < 1.44\, GeV/c^2$.

171   The identification of the kaon is still preliminary at this stage as there is no clear dis-
172 tinction between positive kaons and pions. This issue of kaon-pion mis-identification
173 provides one of the major difficulties with the analysis of CLAS data and will be ad-
174 dressed in section II C.

175   **C.   Particle Identification**

176   *Z-Vertex Cut*

177   The first step in the particle identification was to cut on the z-vertex distribution of
178 each particle to be within the target geometry. For g8b this meant a cut of between 0 and
179 -40 cm, which represents a relatively tight cut. Figure 5 shows the z-vertex distributions
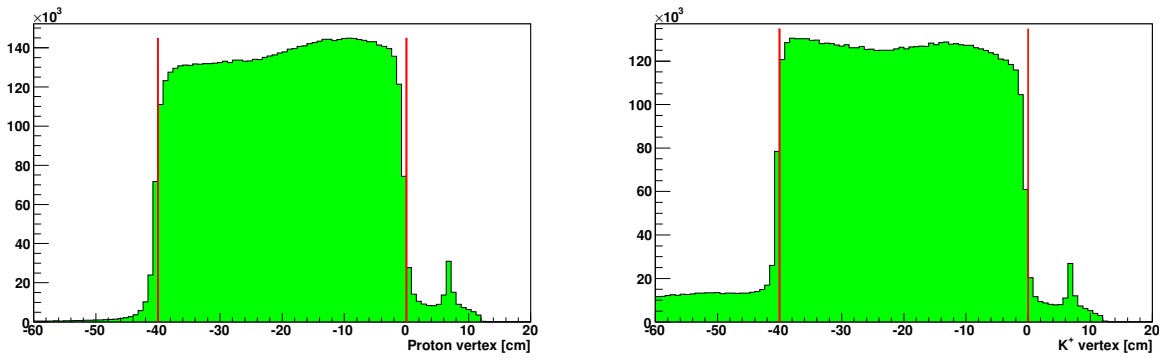180 for the proton and kaon respectively with lines superimposed to show the cuts.

Figure 5. Z-vertex distributions of the proton (left) and K^+ (right) showing the target geometry
along with the applied cuts (red lines).

181

182   *Photon Selection*

183   The next stage in the selection process was to determine the time at which a physics
184 event took place by matching photons to the hadronic tracks within CLAS. To achieve
185 this, information on the hadronic vertex time provided by the TOF was used. The timing
186 information from charged particles detected by the TOF was extrapolated backwards to
187 provide information on when the event occurred. If the TOF and tagger timing calibra-
188 tions are well defined then the tagger and TOF vertex times are expected to be identical.
189 This is shown to be the case in figure 6 (left) where the majority of events have the ver-
190 tex timing difference between tagger and TOF centered on zero. The 2 ns beam bucket
191 structure corresponds to hadrons that have been miscorrelated with random photons.
192 This mismatching of certain hadrons will be addressed in section II C where momentum

193 dependent timing cuts will be applied to reject the out-of-time combinations. A major
194 area of ambiguity in the selection of the real interaction photons is that for many physics
195 events there are multiple photons recorded. In order to select the actual photon cor-
196 responding to the event, the photon whose time is closest to the hadronic vertex time
197 is chosen. The identification of this "best" photon involves minimizing the difference
198 ($Diff$) between the proton vertex time and the photon time using the relation:

$$Diff = (TOFtime(p) - (TOFpath(p)/c \times \beta_c(p))) - (\gamma_{time} + (z(p)/c)) \tag{4}$$

199   where:

$$\beta_c(p) = p(p)/\sqrt{p^2(p) + m_{pdg}^2(p)} \tag{5}$$

200   using the PDG mass for the proton and the measured momentum.

201   Where:

202 $TOFtime(p)$ = proton TOF time

203 $TOFpath(p)$ = proton path length to the TOF

204 γ_{time} = event photon vertex time

205 $z(p) = z - vertex$ position of the proton

206 c = speed of light

207   Figure 6 (right) shows the timing difference after the selection of the best photons us-
208 ing the process outlined above. The plots show a slight asymmetry in the distribution
209 which is due to the proton vertex time having a momentum dependence. This asymmet-
210 ric distribution will also be resolved when momentum dependent timing cuts are made
211 for the proton and kaon. It should be noted that events with more than one best pho-
212 ton are removed at this stage of the analysis since their identification cannot be acheived
213 unambiguously.
214   Once the "best" photon of the event has been identified, the photon energy correction
215 is applied. This correction arises from the physical sag of the tagger which leads to the

216 misalignment of the E-counter scitillator bars. As a consequence of this effect, the elec-
217 tron energy is mis-measured (and therefore the associated photon energy) and requires
218 correction by an energy dependent multiplicative factor to the energy obtained from the
219 TAGR bank. A detailed description of the algorithm can be found in [4].
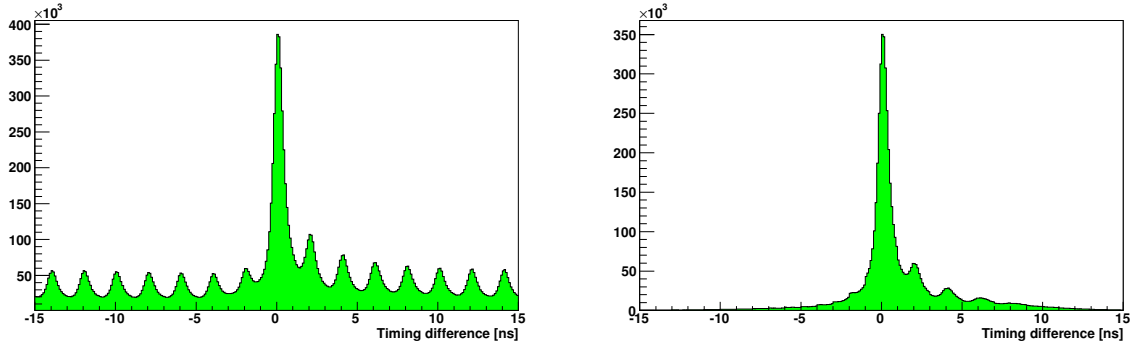

Figure 6. Tagger vertex time subtracted from the time-of-flight vertex time. The plot on the left
displays events before best photon selection with the 2 ns beam bucket structure clearly evident.
The plot on the right displays the vertex time after the photon selection. The asymmetric structure
on the right side of the vertex timing peak will be dealt with when momentum dependent timing
cuts are applied later in the analysis.

220   *Hadron - Photon Vertex Timing Cuts*

221   The next stage of the analysis involved imposing timing cuts on the hadron-photon
222 vertex time. As outlined in section 4.3.2, a well defined set of calibrations should provide
223 good agreement between the photon vertex time from the tagger and the hadronic vertex
224 time from the TOF. Figures 7 and 8 show that the hadron-photon vertex time distribution
225 for the proton and kaon respectively have a substantial momentum dependence. After
226 selecting the best photon, a fairly loose ± 2 ns cut was used to remove events from other
227 beam buckets which could act to dilute the final hyperon yield. Now however, a more
228 rigorous series of momentum dependent $\pm 3\sigma$ cuts are applied to the vertex times when
229 fitted in 100 MeV/c momentum bins.

230   Figure 7 shows the proton-photon vertex and its dependence on the proton momen-
231 tum. It also shows the vertex time after the momentum dependent cuts have been ap-
232 plied, along with the mean and sigma values from the fits. The fits themselves were

233 simple gaussians on top of a first degree polynomial. The momentum dependence of the

234 kaon vertex time is shown in figure 8, with the final vertex after the application of the

235 $\pm 3\sigma$ cuts.
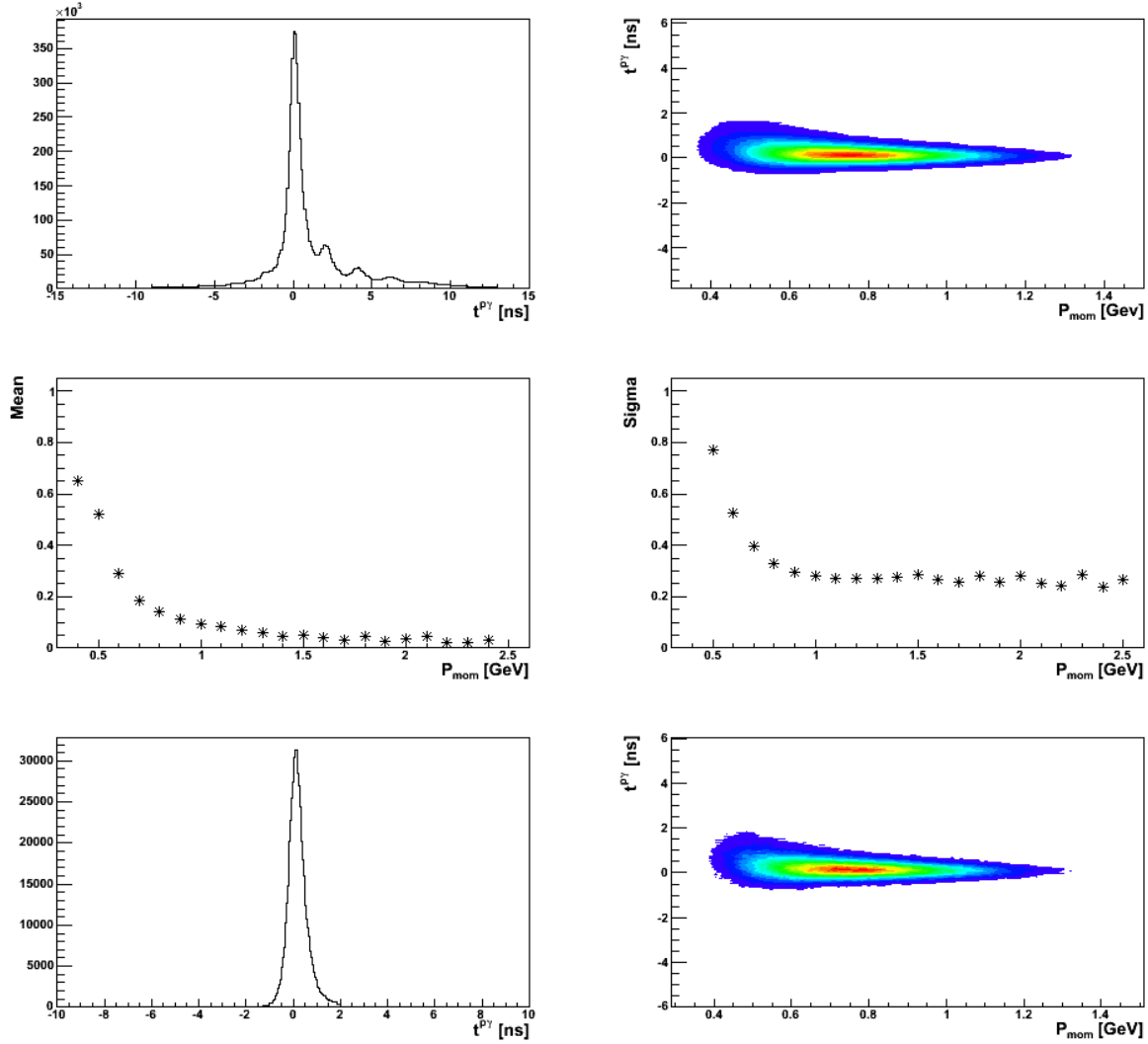

Figure 7. $t_v^{p\gamma}$ plotted on the top left showing some asymmetric 2 ns structure with its momentum dependence plotted on the top right. $t_v^{p\gamma}$ and its momentum dependence are then plotted on the bottom row after 100 MeV/c momentum cuts have been applied. The momentum dependence of the mean (left) and sigma (right) of the vertices are shown quantitatively in the middle row.
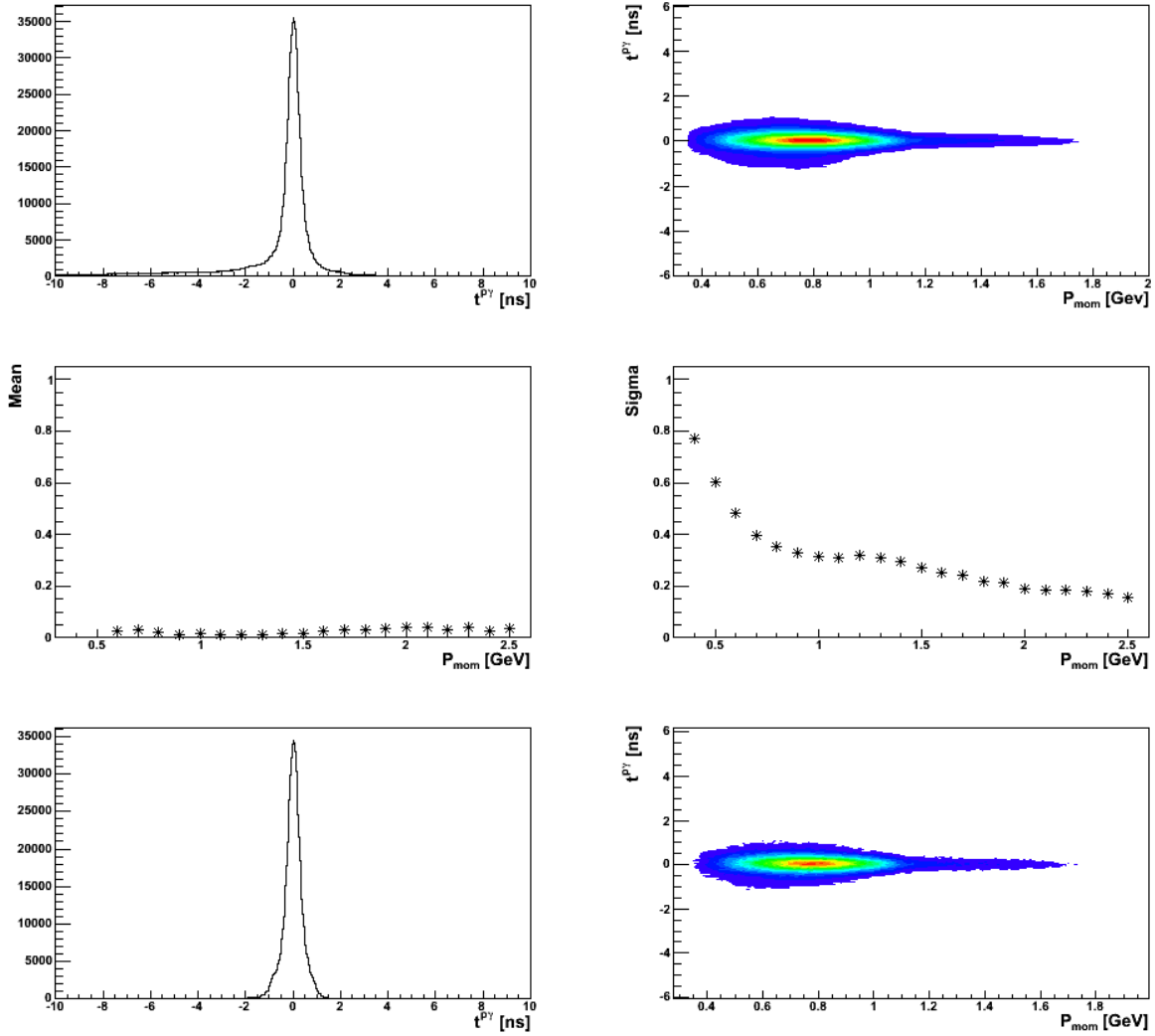
Figure 8. $t_v^{K\gamma}$ plotted on the top left with its momentum dependence plotted on the top right. $t_v^{K\gamma}$ and its momentum dependence are then plotted on the bottom row after 100 MeV/c momentum cuts have been applied. The momentum dependence of the mean (left) and sigma (right) of the vertices are shown quantitatively in the middle row.

236   *Minimum Momentum Cut*

237   At this stage a cut was made on the minimum momentum of any track that would be
238 considered as an event in the particle selection process. This cut was selected to be the
239 same for all charged particles - 300 MeV/c which corresponds to the minimum detection
240 momentum in CLAS.

241   *Energy Loss Corrections*

242   Energy losses in the target and surrounding material were corrected by the ELOSS
243 package [5]. The package operates by taking the 4-vector of the particle of interest, and
244 running it through a series of subroutines to find the pathlength of the particle in each of
245 the materials along the track. The software determines the momentum of the particle at
246 the reaction vertex and can be used for any charged particle heavier than an electron.

247   The energy losses for the kaon and proton in this analysis are shown in figure 9. As
248 can be seen, the energy losses are most significant for low momentum particles, resulting
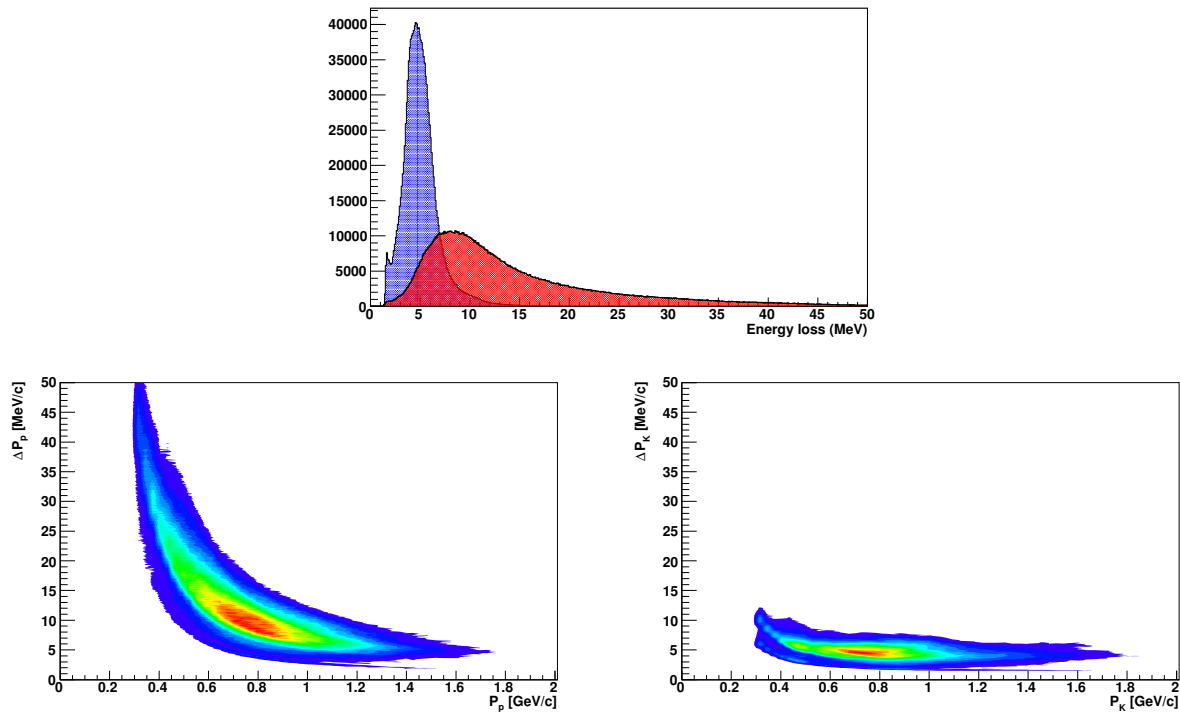249 in the the greatest correction required.

Figure 9. Top: Momentum correction distributions for the K^+ (blue) and the proton (red). Middle: Δp v p for the proton. Bottom: Δp v p for the K^+.

250

251   *Fiducial Cuts*

252   For this analysis a relatively loose fiducial cut on the azimuthal distributions of $\pm 4^0$
253 at each sector division in CLAS was used. This cut was chosen to be the same for both
254 protons and kaons, and its effect is shown in figure 10.
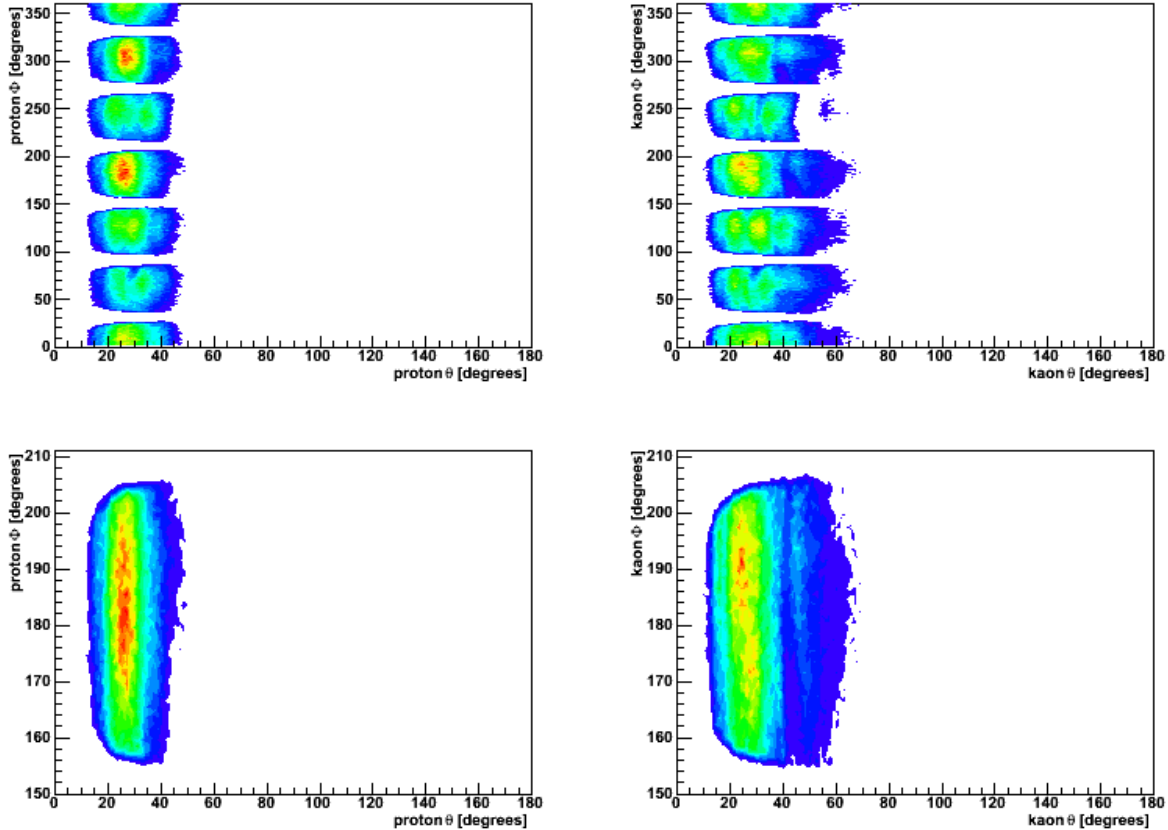
Figure 10. Top row shows θ versus Φ in the lab frame for the proton and kaon respectively before the application of any fiducial cuts. Bottom row shows θ versus Φ for one sector for both the proton and K^+ after the application of fiducial cuts.

255

256   *Misidentification of Charged Particles*

257    $p(\gamma, \pi^+ p)X$ - *Missing Mass*   Another procedure to correct for particle misidentifica-
258 tion is to explicitly make the assumption that pions have wrongly been identified as

259 kaons. In order to remove these events for the K^+p final state the 4-vector for each parti-

260 cle is re-calculated using the measured momenta and by allocating the PDG value of the

261 mass. The missing mass of the K^+p is then plotted, assuming correct particle identifica-

262 tion, against the missing mass assuming misidentification. For misidentified events the

263 correct particle momentum is retained in the 4-vector but the mass is changed to the PDG

264 mass of the assumed misidentified particle.

265 Explicitly the $MM(K^+p)$ is assumed to have one possible misidentification permuta-

266 tion where the identified K^+ is in fact a π^+. Therefore what we are in fact reconstructing is

267 the missing mass $MM(\pi^+p)$. The plot in figure 11 shows $MM(K^+p)$ versus $MM(\pi^+p)$.

268 The 2 horizontal bands correspond to the missing π^- and $\pi^-\gamma$ from correctly identi-

269 fied $K\Lambda$ and $K\Sigma^0$. The vertical band around $0.135\,GeV/c^2$ corresponds to the missing

270 π^- from $(p\pi^+\pi^-)$ events in which the π^+ was wrongly indentified as a kaon. A rela-

271 tively loose cut of $MM(p\pi^+) > 0.17\,GeV/c^2$ was applied to remove these misidentied

272 events. The subsequent cut in the next section was applied in parallel in order to clean

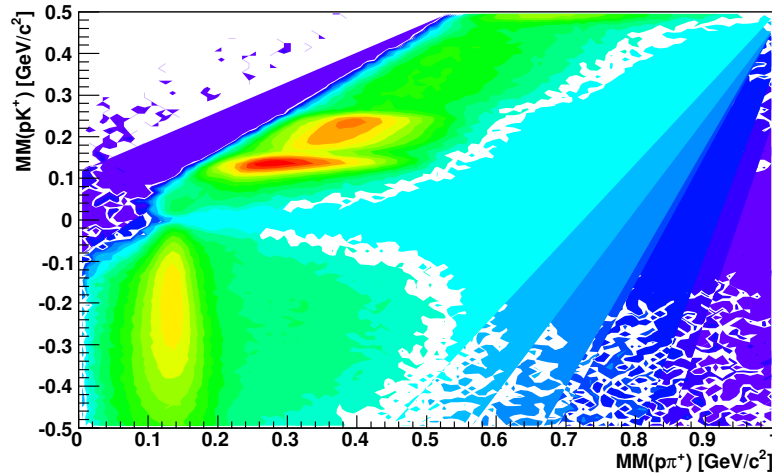273 the $(MM(pK^+))$ distribution further and again represents a fairly loose cut.

Figure 11. $MM(pK^+)$ versus $MM(p\pi^+)$ where the K^+ has been assigned the PDG mass of a π^+. The vertical band at around $0.135\,GeV/c^2$ corresponds to the mass of a missing π^- from the mis-identified $p\pi^+\pi^-$ final state. A cut is made to select $MM(p\pi^+) > 0.17\,GeV/c^2$ to reject these events.

274

275    $p(\gamma, K^+ p)\pi^-$ - *Missing Mass Cut*

276   At this point a cut was applied to the $p(\gamma, K^+ p)\pi^-$ missing mass to select 2-track
277 events that were consistent with a missing pion (3-track events are always accepted even
278 when this cut is applied). As the reactions are exclusive, the missing mass $MM(pK^+)$
279 calculated from the 4-vectors of the proton and kaon should correspond to the mass of
280 a π^- or $\pi^-\gamma$ for Λ and Σ^0 respectively. The actual cut was carried out on the missing
281 mass squared which is plotted in figure 12. A peak can clearly be seen corresponding to
282 the π^- from the $K^+\Lambda$ channel with a mass squared of $0.0185 GeV^2/c^4$. The peak for the
283 π^- from the $K^+\Sigma^0$ channel is shifted to a slightly higher mass squared of $0.045 GeV^2/c^4$
284 due to there being an undetected photon in this reaction. A third peak can also be seen
285 corresponding to the mass squared of a K^- corresponding to $\Lambda(1520)$ production. At this
286 stage a fairly loose cut was placed on the $MM^2(pK^+)$:

287   ● $-0.2 < MM^2(pK^+) < 0.3\ GeV^2/c^4$.

288 This cut was originally much tighter but studies demonstrated that a large number of
289 good $K^+\Lambda$ and $K^+\Sigma^0$ events were being rejected. It was therefore decided that the cut
290 should be loosened slightly to allow for a more liberal selection of events. Although this
291 loosening of the cut would allow more background through at this stage it was felt that
292 subsequent analysis procedures would compensate for this.

293

294

295   *Invariant Mass Selection*

296   One of the major sources of dilution of extracted particle yields from CLAS is the
297 misidentification of charged particles - in particular pions that have been identified as
298 kaons. This problem was illustrated in figure 3 where the kaon mass peak sits on a large
299 pion shoulder. One method of separating these mesons involves looking at a two dimen-
300 sional plot of the $MM(K^+)$ against the invariant mass of the proton and pion from the
301 hyperon decay. Since the pion is not explicitly detected in this analysis we use the 4-
302 vector calculated by subtracting the 4-vectors of the kaon and proton from the target and
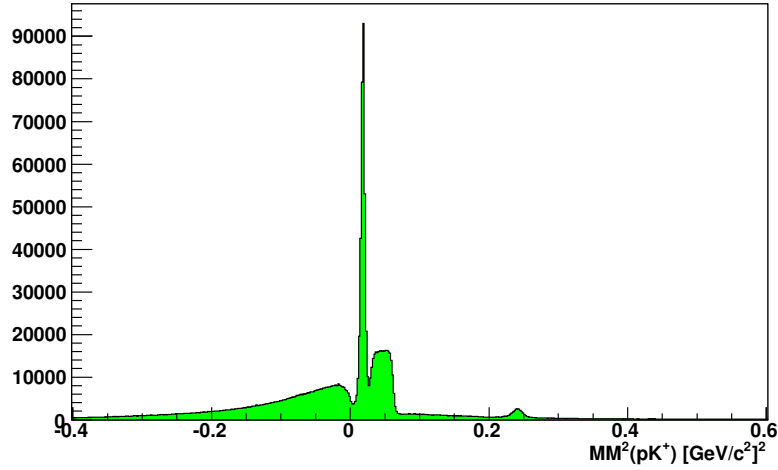
Figure 12. $MM^2(pK^+)$. A peak corresponding to the missing mass squared of the π^- is clearly evident at $0.0185 GeV^2/c^4$ with the π^- from the Σ^0 decay shifted to a slightly higher mass due to the presence of an undetected photon. A peak is also evident for the K^- at a squared mass of $0.240 GeV^2/c^4$. A cut is applied to only accept events with a missing mass squared between -0.2 and 0.3 GeV^2.

Figure 13. $MM(K^+)$ versus Invariant Mass $(p\pi^-)$ showing two clear peaks corresponding to Λ and Σ^0 events and the emergence of the $\Sigma(1385)$. A cut is made in the range $1.06 < M(p\pi^-) < 1.2 GeV/c^2$.

303 photon. In the case of a perfect exclusive particle determination this would correspond
304 to the pion 4-vector. We thus assume perfect particle identification and give this 4-vector
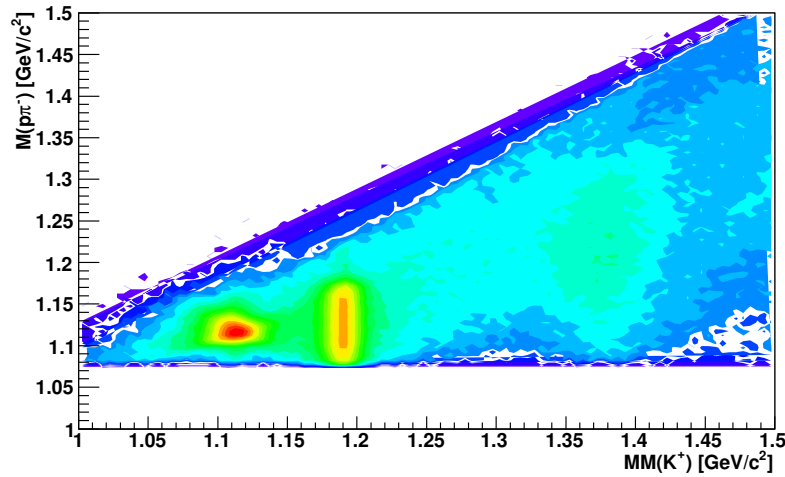305 the π^- PDG mass before plotting it against the $MM(K^+)$ as shown in figure 13.

306   In the two-dimensional plot there is good agreement for the mass of the Λ^0 and Σ^0,
307 with the Σ^0 mass slightly smeared due to the undetected photon from its radiative de-
308 cay. In the plot it should be noted that the clean opening of phase space shows that the
309 removal of misidentified pions had been successful since any remaining would show as
310 a clear diagonal band structure as the $MM(K^+)$ increases. At this stage events with a
311 corresponding invariant mass $M(p\pi^+)$ between 1.06 and 1.20GeV are selected.

312   **D. Hyperon Regions**

313   After the application of the particle identification procedure described, we can exam-
314 ine the final kaon missing mass, $MM(K^+)$, spectra for each of the coherent peak settings
315 as shown in figure 14. The Λ^0 and Σ^0 (and an increasing $\Sigma(1385)$ signal) can be clearly
316 seen with a small background contribution of the order a few percent. This background
317 will be accounted for in the subsequent analysis to determine any dilution to the ex-
318 tracted observables which may occur. Table 2 shows a summary of the cuts applied in
319 the described analysis procedure along with the number of events after each for the 1.5
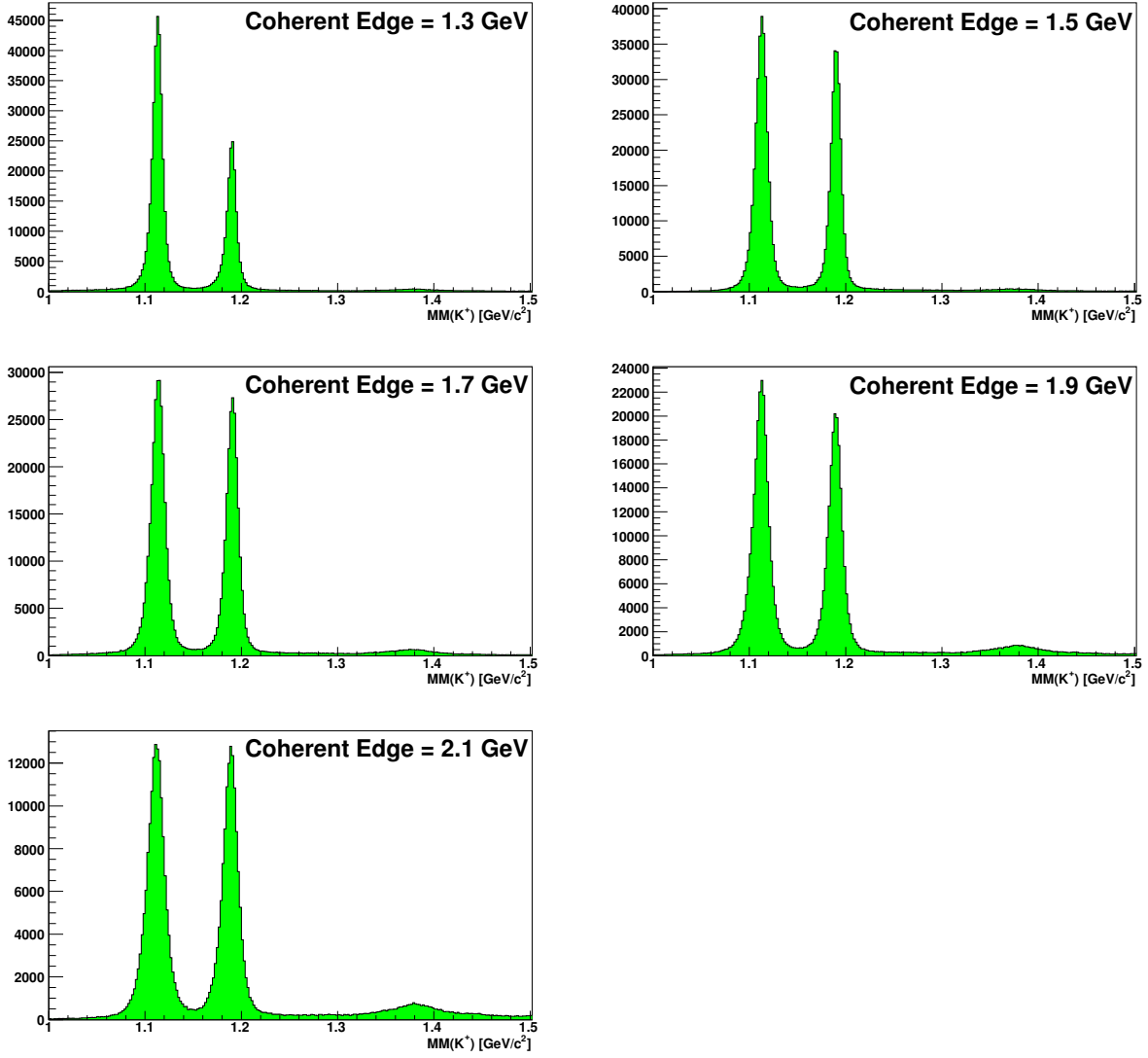320 GeV coherent peak setting.

322

Figure 14. $MM(K^+)$ for all five coherent edge settings (left to right, top to bottom, 1.3, 1.5, 1.7, 1.9, and 2.1 GeV). The final identification of both the Λ and Σ^0 are clearly seen with the background contribution which will be accounted for in the subsequent analysis.

323   **E.   Summary**

Applied Cut	Details	# of Events
Initial skim	TOF mass from EVNT	7082147
z-vertex cut	$-40 \rightarrow 40\,cm$	6003559
γp and γK^+ vertex timing	3σ momentum dependent	1658605
P_p and P_{K^+} cut	$> 300\,MeV/c$	1423313
Fiducial	$\pm\,4^o$ at sector division	1418350
$p(\gamma, \pi^+ p)\pi^-$ Miss-ID and $p(\gamma, K^+ p)\pi^-$ Missing mass	$> 0.17\,GeV/c^2, -0.2 <$ $MM^2(pK^+) < 0.3\,GeV^2/c^4$	841649
Invariant Mass $p\pi^-$	$1.06 < M(p\pi^-) <$ $1.2\,GeV/c^2$	633143

Table II. Analysis cuts applied and resulting number of events for $1.5\,GeV$ coherent peak setting.

324   An analysis algorithm was developed to allow for the identification of the particles of
325 interest and the extraction of final yields for $\overrightarrow{\gamma}\text{p} \rightarrow K^+\Lambda$ and $\overrightarrow{\gamma}p \rightarrow K^+\Sigma^0$. Initial filters
326 based on simple TOF mass cuts were used to skim the dataset down to a manageable size
327 for full analysis. Various cuts were then implemented to reduce the background and cor-
328 rectly identify kaons, without discarding too many good events. The final hyperon mass
329 plots demonstrate the success of these procedures with a background of a few percent
330 between the two hyperon yields.

III.   PHOTON BEAM POLARIZATION

Linearly polarized photons at CLAS are produced using the coherent bremsstrahlung technique [6, 7]. In brief, the electron beam scatters coherently from a crystal radiator (diamond), resulting in some enhancement over the $\sim 1/E_\gamma$ photon energy spectrum observed with an amorphous bremsstrahlung radiator. Figure 15, top panel, shows an example of a coherent bremsstrahlung distribution. It is common practice to plot the *enhancement*, which is the photon energy spectrum obtained with the crystal divided by the same spectrum obtained with an amorphous radiator. This eliminates the channel to channel fluctuations caused by variations in the widths and efficiencies of the detectors (here the focal plane counters of the tagger spectrometer) and also removes the $\sim 1/E_\gamma$ shape, highlighting the coherent contributions. The orientation of the scattering plane is adjusted by setting the azimuthal angle (ϕ) of the crystal lattice in the lab coordinate system, and the relative position of the main coherent peak on the photon energy axis is set by adjusting the small angles between the crystal lattice and the electron beam direction. The photons in the coherent peak are linearly polarized and have an angular spread which is much narrower than that of the unpolarized, incoherent background (ie the characteristic angle $\sim 1/E_\gamma$). So by collimating tightly (less than half the characteristic angle) the ratio of polarized to unpolarized photons is increased, and a greater degree of polarization achieved. At typical Jlab beam settings (eg. coherent peak ~ 1.3 GeV, primary beam ~ 4.5 GeV) the degree of linear polarization can be as high as 90%. A description of the linearly polarized photon beam is given in a CLAS note [2].

Coherent bremsstrahlung theory is well developed, and it is possible to measure the degree of polarization by comparing the enhancement obtained from the tagging spectrometer with a coherent bremsstrahlung calculation. Figure 15, top panel, shows the comparison between the data and calculation, and figure 15, bottom panel, shows the corresponding polarization obtained from the calculation. In an ideal situation, the coherent peak would remain stable and have the same profile for the whole beam time, resulting in a fixed relationship between photon energy and degree of polarization - ie a single lookup table to be used in data analysis. However the significant small angle between the beam and the crystal for typical Jlab conditions is ~ 1 mrad, so even very small
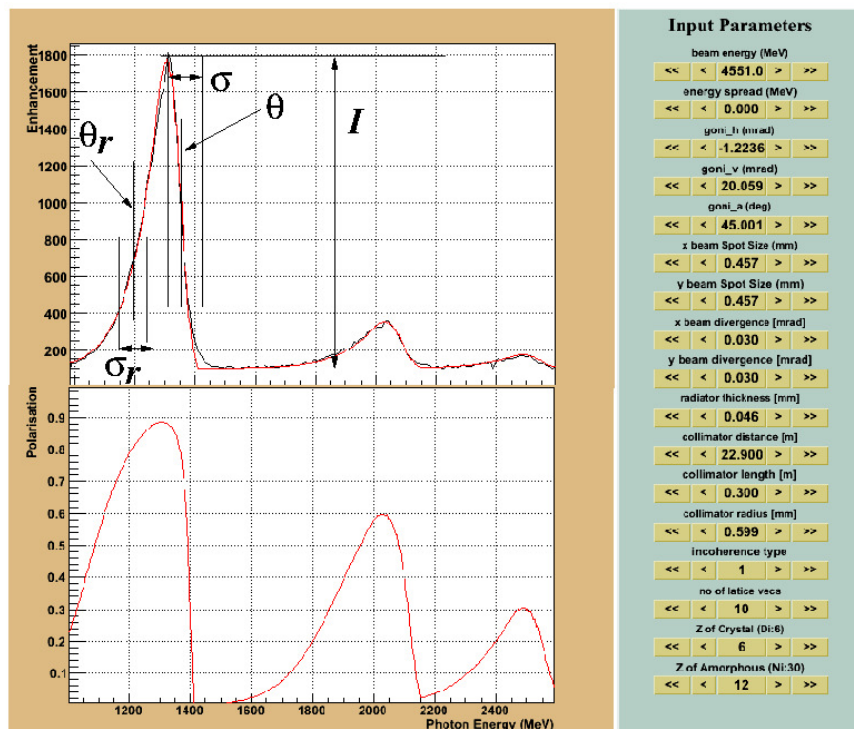
Figure 15. Example of coherent bremsstrahlung spectrum from g8b run period at CLAS

changes in this angle can result in a non-negligible movement of the coherent peak position. An indication of how much movement needs to be accounted for is shown in figure 16, which illustrates the typical variation in the coherent peak position obtained during the whole g8b beam time, where the coherent edge was nominally set at 1.3, 1.5, 1.7, 1.9 and 2.1 GeV. To handle this, a series of fits were made to the enhancement data for each coherent peak position, covering the spread in coherent edge values around the nominal edge energy. Corresponding polarization tables were created in 1 MeV increments of coherent edge position. In the data stream the coherent edge position was recorded as an EPICS variable at 2 s intervals, allowing the appropriate polarization table to be selected for each 2 s worth of data in the analysis. With the correct polarization lookup table loaded the polarization of the photon for every event could be determined. The coherent bremsstrahlung fitting function and method for generating the lookup tables are described in refs [8, 9].

A detailed study of the consistency of the polarization tables has been made, using the
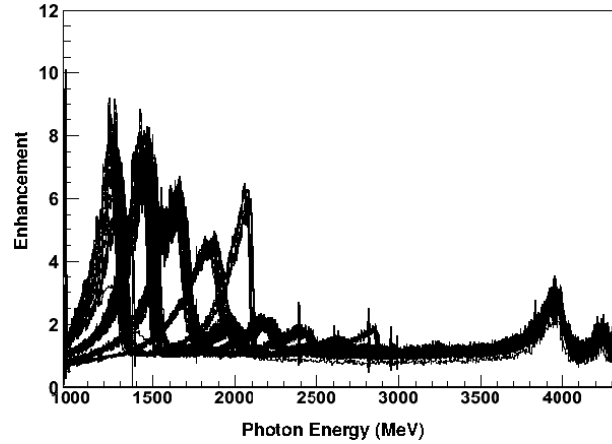
Figure 16. Typical movement in the coherent peak position of g8b data

377 reaction $\gamma p \rightarrow p\pi^0$ [10]. The high statistics from this reaction allow the photon asymme-
378 try Σ to be measured for each tagger energy bin. It was shown that a small systematic
379 correction should be applied to the photon polarization value obtained from the lookup
380 tables based on the difference between the photon energy and the coherent edge en-
381 ergy. A function to modify the polarization has been included in the g8b analysis. It
382 was also shown that the optimum energy window for consistency of the polarization
383 tables was the 200 MeV band below the coherent edge, and only photons in the range
384 $E_{coh} - 200\,MeV < E_\gamma < E_{coh}$ were used in the final analysis. This study is described
385 in detail in ref [10] and its application in the measurement of Σ for $\gamma p \longrightarrow p\pi^0$ and
386 $\gamma n \longrightarrow \pi^+ n$ from g8b is discussed in a CLAS Analysis note recently approved by the
387 review committee [11]. From this study the estimated systematic error on the beam po-
388 larization is 4% for the 1.3, 1.5, 1.7, 1.9 GeV coherent peak settings, and this is borne out
389 by the good agreement between the measured photon asymmetries with and previously
390 published data. At 2.1 GeV where the fits to the data were less consistent we estimate the
391 systematic error to be 6%. The lower statistics in the hyperon channels make it impossi-
392 ble to repeat this study in a rigorous, quantitative way, but we can confirm the result by
393 comparing photon asymmetries in the overlap regions between adjacent coherent peak
394 settings. Figure 17 shows the photon asymmetry as a function of W for both the Λ and
395 Σ hyperons using large bins in $\cos\theta_{cm}$ to maximize the statistics. The top two plots show
396 the results for the Λ and Σ^0 measured separately for each coherent peak (colored circles)
397 together with the results from the full data set (black circles). The bottom plot shows the

398 results from the full data set for Λ and Σ^0, together with the coherent peak positions and

399 overlap regions indicated by arrows.

400   Any issue with the systematics of the polarization would be in the overlap regions,

401 and would result in a discontinuity which would be evident at the same point in both the

402 Λ and Σ^0 . The is no indication of any trend across these regions.
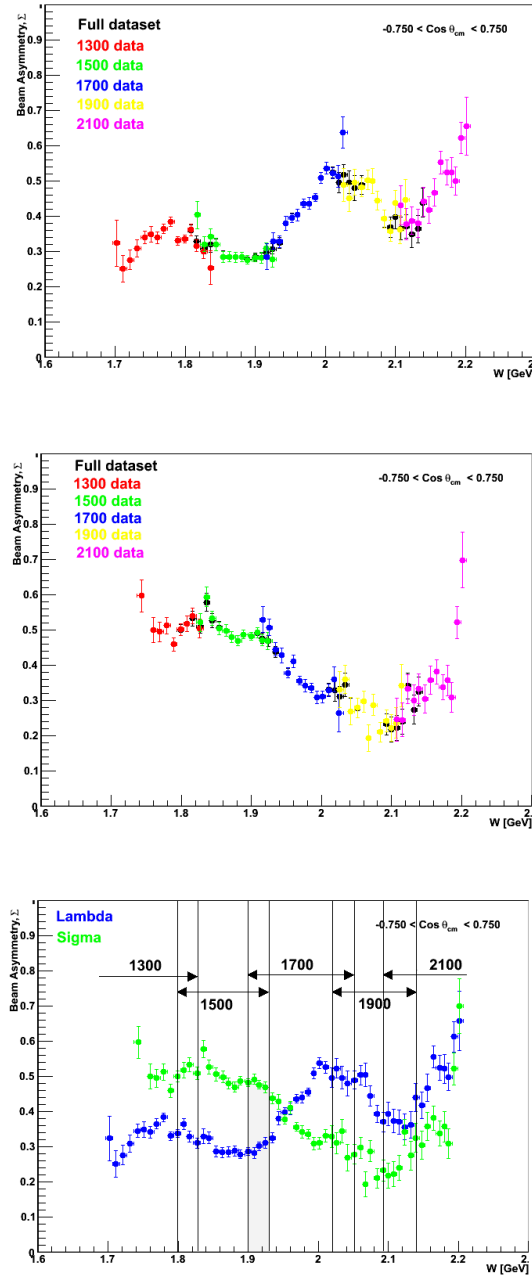
Figure 17. Photon asymmetry as a function of W for both the Λ and Σ^0 using large bins in $\cos\theta_{cm}$ to maximize the statistics. The upper pair of plots show the results for the Λ and Σ^0 measured separately for each coherent peak (colored circles) together with the results from the full data set (black circles). The bottom plot shows the results from the full data set for Λ and Σ^0, together with the coherent peak positions and overlap regions indicated by arrows.

₄₀₃ **IV.   EXTRACTING OBSERVABLES**

₄₀₄   In order to extract the observables dependent on photon polarization, two fitting tech-
₄₀₅ niques have been employed in this analysis: the *binned* fitting technique, which is a χ^2
₄₀₆ fit of a function to a 1- or 2-D histogram, and an *unbinned* or Maximum Likelihood (ML)
₄₀₇ technique, which determines probabilities on an event-by-event basis. The binned tech-
₄₀₈ nique has been used in section III for checking the consistency of photon polarization
₄₀₉ estimates. It is also used in the study of whether the background has any measurable
₄₁₀ polarization effects in section IV C. We shall use the term ML to refer to the unbinned
₄₁₁ technique to remove confusion between not binning in histograms, but binning in the
₄₁₂ variables W and $\cos\theta$.

₄₁₃   Care must be taken in the use of the binned fitting technique, especially when fitting 1-
₄₁₄ D functions where an implicit integration is carried out over a number of other kinematic
₄₁₅ variables. In that case, variation in acceptance can give rise to wrongly extracted values,
₄₁₆ and we illustrate this in section IV B with the example of comparing results from 2-track
₄₁₇ and 3-track final state events.

₄₁₈   Apart from those studies mention above, the ML technique has been used for all the
₄₁₉ other extractions of observables in this analysis. The advantages of this are that all ob-
₄₂₀ servables are extracted consistently, and that known constraints can be imposed. A com-
₄₂₁ parison between the two techniques is illustrated in section VI A. Both techniques rely
₄₂₂ on a likelihood function whose parameters are varied to fit the data. We now give a
₄₂₃ derivation of the expressions used.

₄₂₄   **A.   Data Model**

₄₂₅   The coordinate system employed in this analysis is the so-called "unprimed" frame,
₄₂₆ where for a photon momentum $\vec{k}$ and a kaon momentum $\vec{q}$, axes are defined such that

$$\hat{z}_{evt} = \frac{\vec{k}}{\left|\vec{k}\right|}; \quad \hat{y}_{evt} = \frac{\vec{k} \times \vec{q}}{\left|\vec{k} \times \vec{q}\right|}; \quad \hat{x}_{evt} = \hat{y}_{evt} \times \hat{z}_{evt}$$

₄₂₇ If the spins of all particles are quantized along $\hat{z}$, then the polarization observables are in
₄₂₈ the longitudinal basis [12]. The relationship between these directions, and those in a lab
₄₂₉ frame is shown in figure 18. It is important to note the distinction between the azimuthal

430 angle that appears in theoretical cross-section formulae and the angle that is measured in
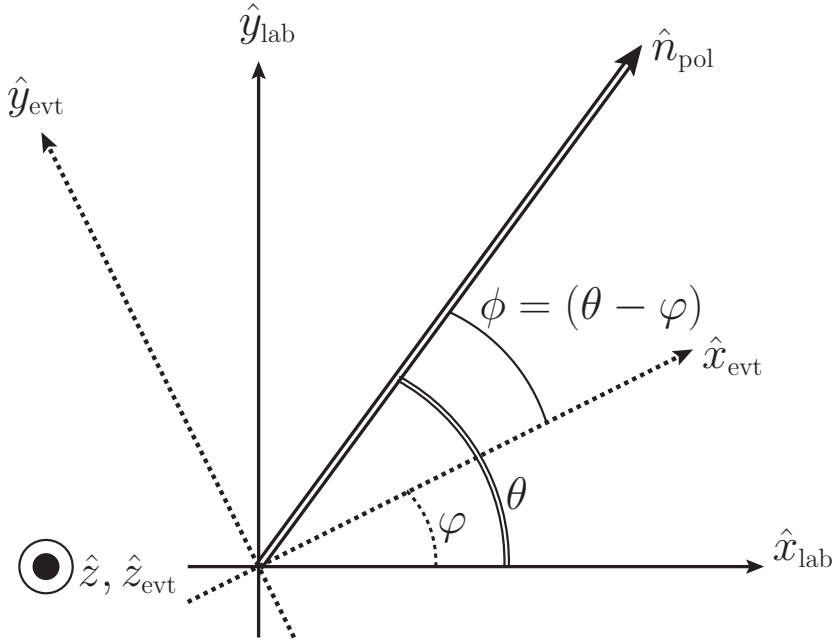431 an experiment.

Figure 18. (Taken from [12]) The definitions of azimuthal angles.

432 　　In order to construct a likelihood function, one must provide a probabilistic model for
433 what the data would be, given the model with its parameters set to specific values. The
434 differential cross section for the reaction, assuming linear photon polarization only and
435 that recoil polarization can be determined, reads

$$
\begin{aligned}
\frac{d\sigma}{d\Omega} \equiv \sigma\left(\phi, \cos\theta_x, \cos\theta_y, \cos\theta_z\right) = \sigma_0 \Big\{ & 1 - P^\gamma \Sigma \cos 2\phi \\
& + \alpha \cos\theta_x P^\gamma O_x \sin 2\phi \\
& + \alpha \cos\theta_y P - \alpha \cos\theta_y P^\gamma T \cos 2\phi \\
& + \alpha \cos\theta_z P^\gamma O_z \sin 2\phi \Big\},
\end{aligned}
\tag{6}
$$

436 where σ_0 represents the unpolarised cross-section, P^γ is the degree of linear photon po-
437 larization, ϕ is the azimuthal angle between the scattering plane and the photon polar-
438 ization direction, α is the Λ weak decay asymmetry and everything else is a polarization
439 observable. To make subsequent notation compact, we make the following alterations:

440 　　• The variables $\cos\theta_x, \cos\theta_y, \cos\theta_z$ are the direction cosines of the decay proton in the
441 　　　Λ rest frame. Let the notation for these now be x, y, z where there is no confusion
442 　　　over reference frames or coordinate systems.

443 • Let ξ represent the set $\{\phi, x, y, z\}$ where there is no need to express the individual

444 variables separately.

445 Beware the possibility of confusing P^γ, the photon beam polarization, with P, the Λ recoil

446 polarization. There is also a possibility of confusing Σ, the photon beam asymmetry

447 observable, with Σ, the hyperon. The CLAS note [13] altered notation to accommodate

448 this, but we have reverted back to what is now in common usage, and stick rigidly to the

449 notation in [12] with the exception of the use of P^γ rather than P_L^γ for photon polarization,

450 since it is understood that photons are only linearly polarized in this experiment.

451 The cross-section formula (6) can be rearranged to separate out the dependence on

452 beam polarization:

$$
\begin{aligned}
\sigma\left(\xi\right) \ = \ \sigma_0 \{ & 1 + \alpha y P \\
& - P^\gamma \left[\left(\Sigma + \alpha y T\right) \cos 2\phi \right. \\
& \left. - \alpha \left(x O_x + z O_z\right) \sin 2\phi \right] \}.
\end{aligned}
\tag{7}
$$

453 Functions independent of, and dependent on ϕ can be defined:

$$
\begin{aligned}
f\left(y\right) & \equiv f = \ 1 + \alpha y P \\
g\left(\phi, x, y, z\right) & \equiv g = \ \left(\Sigma + \alpha y T\right) \cos 2\phi - \alpha \left(x O_x + z O_z\right) \sin 2\phi,
\end{aligned}
$$

454 giving a compact expression for the differential cross-section:

$$
\sigma\left(\xi\right) = \sigma_0 \left(f - P^\gamma g\right)
\tag{8}
$$

455 Now the azimuthal angle ϕ between the scattering plane and the photon polarization

456 vector is determined in the lab by fixing the angle of the photon polarization vector θ and

457 measuring the azimuthal angle of the scattering plane (kaon) φ. In addition, there may

458 be a systematic offset of the goniometer that gives rise to a small offset $\delta\phi$ in the photon

459 polarization direction. Experience has shown that this is likely to be only a few degrees,

460 and of course common to both settings. The relationship among angles is then

$$
\phi = \theta + \delta\phi - \varphi.
$$

461 Two settings are usually employed:

462 • Parallel. If the lab axes are defined with $\hat{z}_{lab}$ in the direction of the beam, $\hat{y}_{lab}$ ver-

463 tically upwards and $\hat{x}_{lab} = \hat{y}_{lab} \times \hat{z}_{lab}$, then the polarization vector is parallel to

464 $\hat{x}_{lab}$. In this case, $\theta = 0$, so $\phi = \delta\phi - \varphi$. This is labelled "$\parallel$", and the azimuthally

465 dependent function from above becomes

$$g\left(\phi, x, y, z\right) \equiv g = \left(\Sigma + \alpha y T\right)\cos 2\left(\varphi - \delta\phi\right) + \alpha\left(xO_x + zO_z\right)\sin 2\left(\varphi - \delta\phi\right),$$

466 • Perpendicular. The polarization axis is in the lab $\hat{y}_{lab}$ direction. In this case $\theta = \frac{\pi}{2}$,

467 so $\phi = \frac{\pi}{2} + \delta\phi - \varphi$. This is labelled "$\perp$", and

$$g\left(\phi + \tfrac{\pi}{2}, x, y, z\right) = -\left(\Sigma + \alpha y T\right)\cos 2\left(\varphi - \delta\phi\right) - \alpha\left(xO_x + zO_z\right)\sin 2\left(\varphi - \delta\phi\right)$$
$$= -g\left(\phi, x, y, z\right),$$

468 We define a cross section *asymmetry* by:

$$A\left(\xi\right) = \frac{\sigma_\perp\left(\xi\right) - \sigma_\parallel\left(\xi\right)}{\sigma_\perp\left(\xi\right) + \sigma_\parallel\left(\xi\right)},$$

469 Re-writing this with the functions f and g, the asymmetry for finite bins in $\xi \equiv$

470 $\{\phi, x, y, z\}$ is [13]

$$A\left(\xi\right) = \frac{\bar{P}^\gamma g}{f + \bar{P}^\gamma \Delta P^\gamma g}. \tag{9}$$

471 The photon polarization in the two settings is not generally the same, so we introduce

472 $\bar{P}_\gamma = \frac{1}{2}\left(\bar{P}_\perp^\gamma + \bar{P}_\parallel^\gamma\right)$ as the average photon polarization for all events in the bin and $\Delta P^\gamma =$

473 $\frac{\bar{P}_\perp^\gamma - \bar{P}_\parallel^\gamma}{\bar{P}_\perp^\gamma + \bar{P}_\parallel^\gamma}$ as the asymmetry in average polarizations between settings.

474 *Estimator of Asymmetry*

475 In one $\{W, \cos\theta_{CM}\}$ bin, at one setting ($\parallel$ or $\perp$), the number of events counted will be

$$N\left(\xi\right) = \varepsilon\left(\xi\right)L\sigma\left(\xi\right),$$

476 with L the luminosity, which is not dependent on the variables ξ, and ε is the acceptance.

477 The measured asymmetry is an asymmetry of *counts*:

$$\Delta N\left(\xi\right) = \frac{N_\perp\left(\xi\right) - N_\parallel\left(\xi\right)}{N_\perp\left(\xi\right) + N_\parallel\left(\xi\right)} = \frac{\varepsilon_\perp\left(\xi\right)L_\perp\sigma_\perp\left(\xi\right) - \varepsilon_\parallel\left(\xi\right)L_\parallel\sigma_\parallel\left(\xi\right)}{\varepsilon_\perp\left(\xi\right)L_\perp\sigma_\perp\left(\xi\right) + \varepsilon_\parallel\left(\xi\right)L_\parallel\sigma_\parallel\left(\xi\right)}. \tag{10}$$

478 A key point here is that acceptance does *not* depend on the orientation of photon E-

479 vector relative to the detector. Changing the polarization direction of the photon involves

480 rotating the E-vector, but *not* the detector, so the acceptance for a phase-space volume in
481 one setting is the same in the other setting. It can therefore be divided out.

482   Dropping the explicit dependence on ξ for convenience, the averages and asymmetries
483 of luminosity and the data model cross-section:

$$\bar{L} = \frac{L_\perp + L_\parallel}{2}; \quad \Delta L = \frac{L_\perp - L_\parallel}{L_\perp + L_\parallel};$$

484

$$\bar{\sigma} = \frac{\sigma_\perp + \sigma_\parallel}{2}; \quad \Delta\sigma = A = \frac{\sigma_\perp - \sigma_\parallel}{\sigma_\perp + \sigma_\parallel}.$$

485   Rearranging Eq. 10, we have an expression that only depends on the asymmetries of
486 the contributing quantities:

$$\Delta N = \frac{\Delta L + A}{1 + + A\Delta L}. \tag{11}$$

487   Plugging 9 into 11 gives

$$\Delta N = \frac{\Delta L + \frac{\bar{P}^\gamma g}{(f + \bar{P}^\gamma \Delta P^\gamma g)}}{1 + \frac{\Delta L \bar{P}^\gamma g}{(f + \bar{P}^\gamma \Delta P^\gamma g)}} = \frac{\bar{P}^\gamma \left(1 + \Delta P^\gamma \Delta L\right) g + \Delta L f}{\bar{P}^\gamma \left(\Delta P^\gamma + \Delta L\right) g + f}. \tag{12}$$

488   Now the ΔN defined above is a function of the four kinematic variables represented by
489 ξ. Hence by binning data in 4-dimensional histograms for each setting, and forming an
490 asymmetry histogram from them, one can perform a χ^2 fit to extract observables. How-
491 ever, whilst binned fits to 4-dimensional asymmetry histograms is possible in principle,
492 the sparseness of data is one of the reasons why an unbinned method is preferrable. One
493 could effectively integrate over two of the kinematic variables to form 2-D asymmetries,
494 $\Delta N\left(\phi, x\right), \Delta N\left(\phi, y\right), \Delta N\left(\phi, z\right)$, say, whose fit by 2-D functions is more tractable, and we
495 can use more simplified expressions for the functions f and g:

$$
\begin{aligned}
f\left(\phi, x\right) &= 1 \\
g\left(\phi, x\right) &= \Sigma \cos 2\phi - \alpha x O_x \sin 2\phi \\
f\left(\phi, y\right) &= 1 + \alpha y P \\
g\left(\phi, y\right) &= \left(\Sigma + \alpha y T\right) \cos 2\phi \\
f\left(\phi, z\right) &= 1 \\
g\left(\phi, z\right) &= \Sigma \cos 2\phi - \alpha z O_z \sin 2\phi
\end{aligned}
$$

₄₉₆ Note that this will only strictly be true if the acceptance is uniform for the two vari-
₄₉₇ ables that have been integrated over. Nevertheless this provides us with an approximate
₄₉₈ method to compare with the unbinned results.

₄₉₉   As an explicit example, to extract Σ and O_x from a 2-D asymmetry in ϕ and x, we have

$$\Delta N\left(\phi, x\right) = \frac{\bar{P}^\gamma\left(1 + \Delta P^\gamma \Delta L\right)\left(\Sigma \cos 2\phi - \alpha x O_x \sin 2\phi\right) + \Delta L}{\bar{P}^\gamma\left(\Delta P^\gamma + \Delta L\right)\left(\Sigma \cos 2\phi - \alpha x O_x \sin 2\phi\right) + 1}. \tag{13}$$

₅₀₀   If only the kaon angle were measured, but placing no restriction on the proton from
₅₀₁ the Λ decay, this expression reduces to

$$\Delta N\left(\phi\right) = \frac{\bar{P}^\gamma\left(1 + \Delta P^\gamma \Delta L\right)\Sigma \cos 2\phi + \Delta L}{\bar{P}^\gamma\left(\Delta P^\gamma + \Delta L\right)\Sigma \cos 2\phi + 1}, \tag{14}$$

₅₀₂ which, in the limit of equal luminosities and photon polarizations in the $\parallel$ and $\perp$ settings,
₅₀₃ reduces further to the familiar $\cos 2\phi$ form:

$$\Delta N\left(\phi\right) = \bar{P}^\gamma \Sigma \cos 2\phi = \bar{P}^\gamma \Sigma \cos 2\left(\varphi - \delta\phi\right).$$

B.   Binned Fitting Technique

₅₀₅   In this method the event by event data is plotted into parallel ($\parallel$) and perpendicular
₅₀₆ ($\perp$) histograms binned in azimuthal angle. Separate sets of these angular distribution
₅₀₇ histograms are used for each kinematic bin (in W and $\cos\theta_{cm}$) and the polarization infor-
₅₀₈ mation for each bin is determined using the event by event photon polarization values
₅₀₉ retrieved from the lookup tables described in section III. An asymmetry of the histograms
₅₁₀ is formed and observables are extracted from a fit to this.

1-D Extraction of Σ

₅₁₂   Eq. (14) can be used as a fit function for extracting Σ. The average photon polarization
₅₁₃ $\bar{P}_\gamma$ and photon polarization asymmetry ΔP^γ are determined with the method described
₅₁₄ in section III. A significant feature of this fit is that it allows the extraction of the photon
₅₁₅ beam asymmetry without needing to explicitly know the fluxes of the data sets; in fact
₅₁₆ the asymmetry of the fluxes ΔL can be extracted from a high statistics fit and used to fix
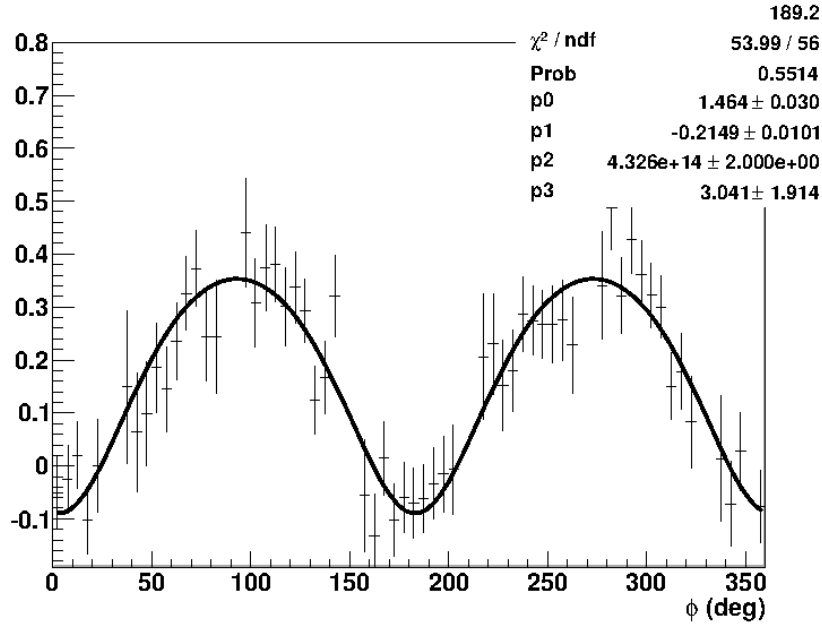₅₁₇ the parameter in lower statistics fits. A more detailed discussion of this method, together

Figure 19. Example of a binned fit using the function given in Eqn.**??**

518 with some simulated examples, is given in reference [14]. Figure 19 shows an example of
519 an asymmetry fitted using eq.14.

520   However, the expression for the asymmetry given in Eqn. 14 relies on only using the
521 azimuthal angle of the kaons. This is certainly valid when only the kaon is detected, how-
522 ever if the detection of the decay products of the hyperon is required, as is the case in this
523 analysis, then the acceptance can have a non-negligible effect. This is illustrated in figure
524 20, where a clear $\cos 2\phi$ distribution can be seen, but with an offset that is not consistent
525 with the known experimental orientation of the polarization plane. To understand why
526 this happens, one needs to examine a 2-D fit, using eq. (13).

527   *2-D Extraction of Σ and O_x*

528   A typical fit of eq. (13) is depicted in figure 21. In this case both Σ and O_x can be
529 extracted.

530   The 1D extraction of Σ is effectively a fit to the integral over all $\cos \theta_x$ of the data shown
531 in figure 21. This illustrates the reason for the phase shift of the data shown in figure 20: if
532 the acceptance varies with $\cos \theta_x$ then the contribution of the different slices to the integral
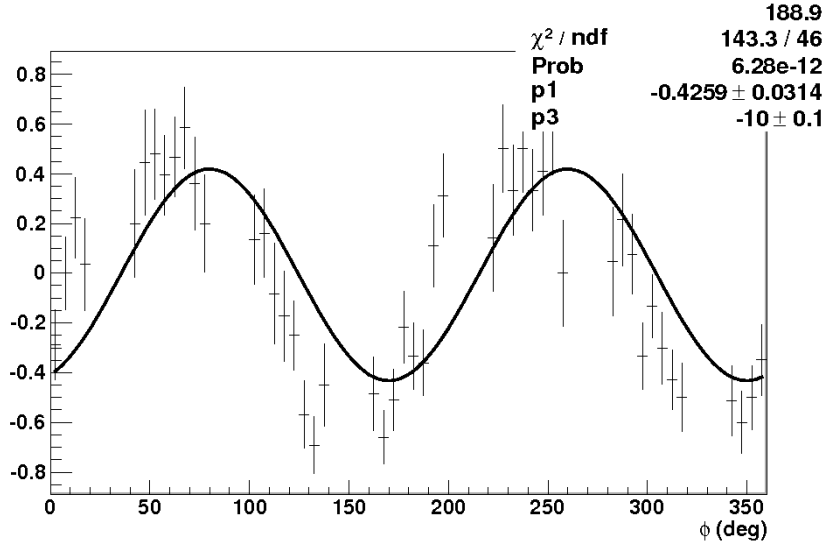533 will be unequal, resulting in a shift in the phase and amplitude of the $\cos 2\phi$ distribution,

Figure 20. Example of a binned fit using the function given in Eqn.14. The phase offset $\delta\phi$ in the fit was constrained to be less that $10°$, but it is clear that the phase shift of the data greater than that.

534 and introducing an error to the measurement of the beam asymmetry Σ, particularly if 535 the double polarization observable has a significant magnitude (which will be seen to be 536 the case).

537   Any such acceptance effect could be stronger for a more exclusive final state where 538 more particles are detected, since a more exclusive region of phase space has been carved 539 out by demanding more detected particles. Figure 22 shows examples of photon asym- 540 metry derived from the 1D fit over a range of bins in W for both the Λ and Σ^0 , firstly 541 with only the proton detected (2-track), and then with both the proton and π^- detected 542 (3-track). The data for the beam asymmetry Σ and phase offset $\delta\phi$ are shown.

543   It should be noted that in the high statistics, single pion analysis of the g8b data the 544 phase offset has already been determined to be consistent with 0, and for other analysis 545 discussed in this note was fixed at 0. In the case of the Λ there is considerable, W de- 546 pendent, disagreement on both the extracted beam asymmetry and the phase offset and, 547 furthermore, in neither topology is ϕ_0 consistent with 0. For the Σ^0, the two topologies 548 give consistent results for the beam asymmetries, and both give results consistent with 549 0 for the phase offset $\delta\phi$. The much better results for the Σ^0 can be explained by noting 550 that the undetected $\sim 70MeV$ γ-ray, which is emitted as the Σ^0 decays to a Λ, effectively

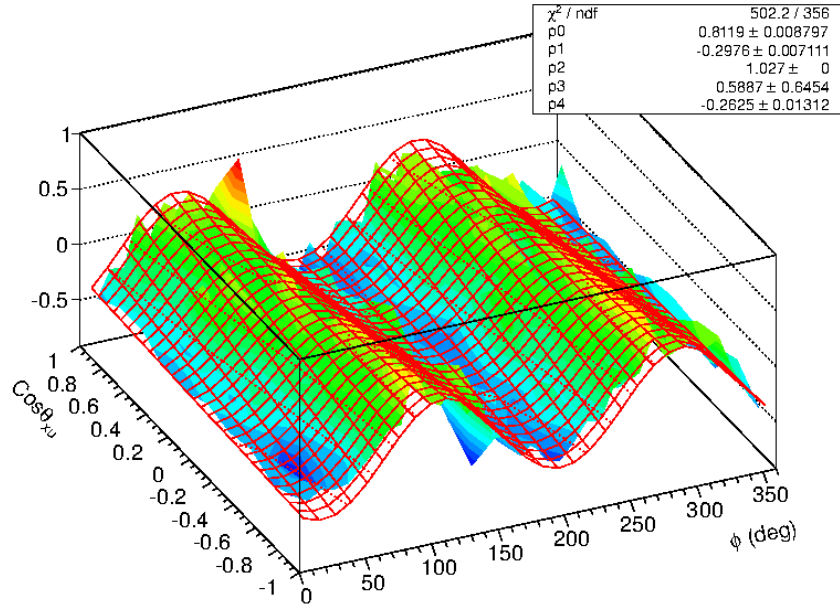| χ^2 / ndf	502.2 / 356
p0	0.8119 ± 0.008797
p1	-0.2976 ± 0.007111
p2	1.027 ± 0
p3	0.5887 ± 0.6454
p4	-0.2625 ± 0.01312

Figure 21. Example of a 2D binned fit using the function given in Eqn.13

551 smears the acceptance in ϕ and $\cos\theta_x$.

552   The conclusion here is that any extraction of the beam asymmetry based on binned

553 fitting should be performed by fitting the 2D asymmetry as opposed to the 1D asymme-

554 try. The problem of "false" offsets does not completely disappear, the the $K\Lambda$ case, so a

555 fit that takes into account the distributions of events in the four kinematic variables ξ is

556 necessary. All final results have been extracted using a likelihood analysis and the use of

557 binned fitting has been restricted to the study of systematics and background.
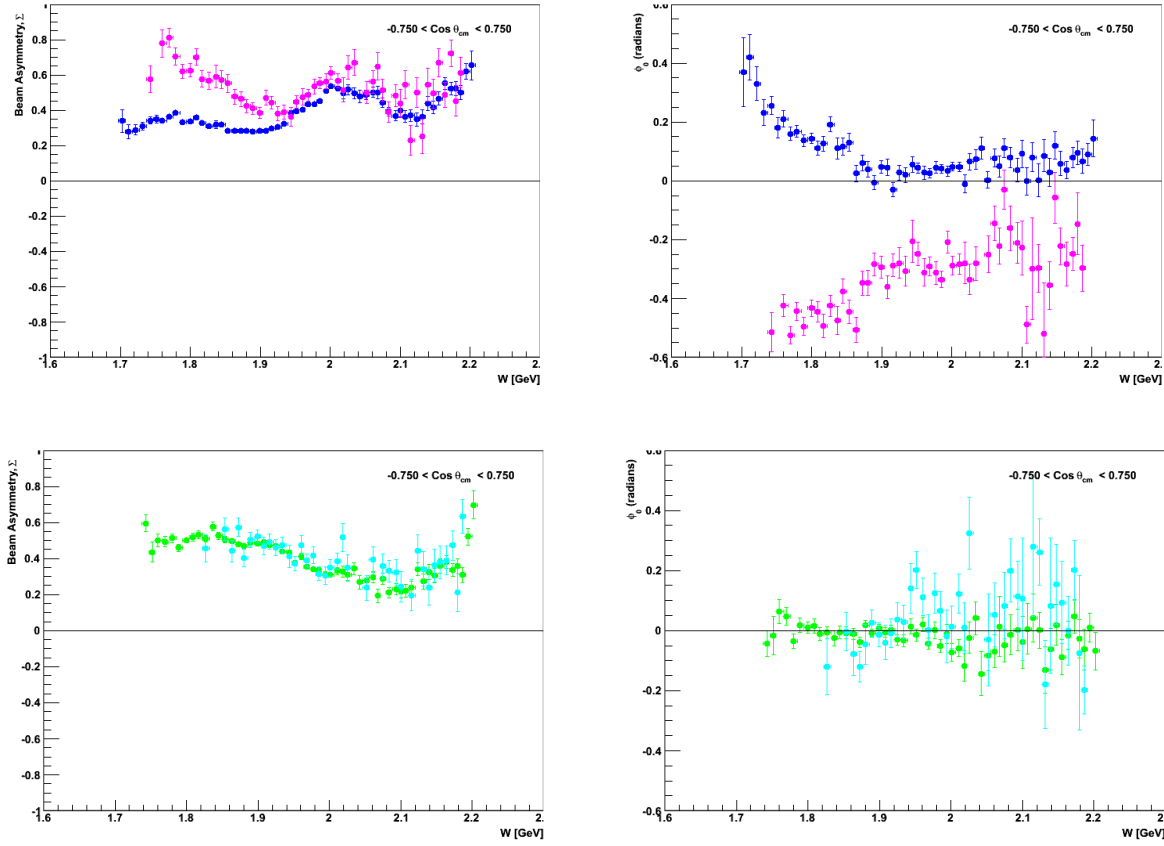
Figure 22. A comparison of the values of the photon asymmetry Σ and phase offset π^0 extracted from the 1D asymmetry plots over a range of bins in W. The data is integrated over all -0.75 < $\cos\theta_{cm}$ < +0.75 to maximize the statistics. The top plots show the results for the Λ hyperon and the bottom plots for the Σ hyperon. For the Λ data, results from detection of a K and p are shown in blue, and those requiring a K and p, π^- in magenta. For the Σ hyperon data, results from detection of a K and p are shown in green, and those requiring a K and p, π^- in cyan.

558   **C.   Background correction**

559   As described in section II, the final selection for Λ and Σ^0 events is based on 3σ cuts

560 on the respective peaks in the missing mass spectrum. Figure 23 shows a typical missing

561 mass distribution for events which have satisfied the event selection criteria. The Λ and

562 Σ^0 (and Σ^*) are clearly visible but sitting on top of a non-negligible background. To

mMiss W: 1.981-2.023, CosThetaCM: -0.75 - 0.75
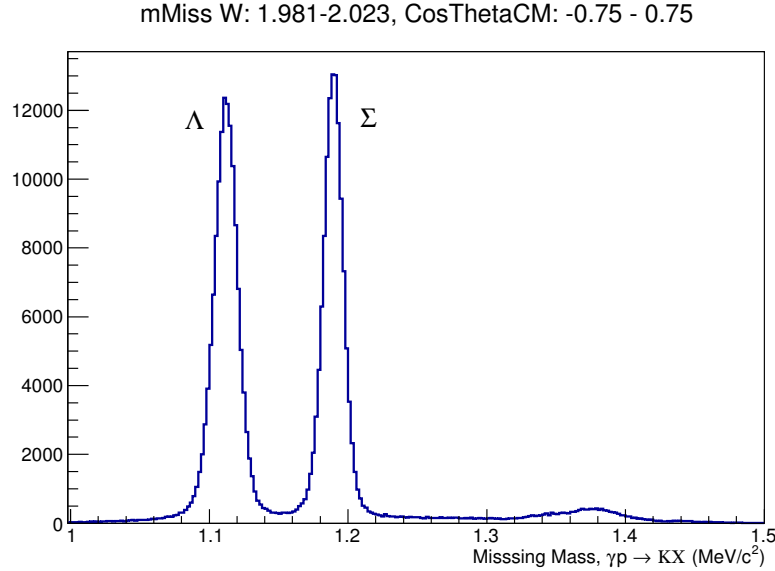
563   Figure 23. Missing mass for identified hyperon events

564

565 quantify this the data was fitted using ROOT's TSpectrum::Background() function and

566 the ratio of background / total for each peak was made using the integrals of the data

567 and the fit between the respective limits. This is shown in Figure 24.

568   As can be seen from the figure, the background contamination for this bin was $\sim$3%

569 under the Λ and $\sim$2.5% under the Σ. To assess the variation with W and $\cos\theta_{cm}$ the data

570 was split into 13 bins in W (each bin corresponding to 10 tagger channels) and 4 bins

571 in $\cos\theta_{cm}$. The results are shown in Figure 25. There is a small dependence on W and

572 $cos\theta_{cm}$where the contamination ranges from $\gtrsim$5% at low W, backward angles to $< 1.5\%$

573 at higher W, forward angles. The results of these fits were stored in tables for Λ and Σ^0

574 and the background was measured for each kinematic bin used in the final analysis by

575 interpolating from this table using the values of W and $\cos\theta_{cm}$ for the bin center.

576   This background is mainly due to uncorrelated pions from different time buckets

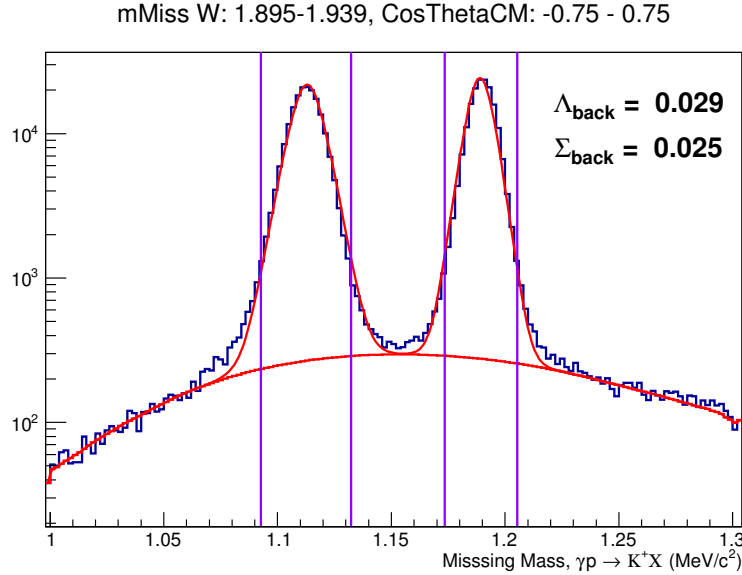577 misidentified as kaons, and should have no intrinsic photon asymmetry. To confirm this

Figure 24. An example of the measurement of the background under the Λ and Σ^0. The lower red line show the background fit. For each of the peaks the ratio of background / total is made using the integrals of the data and the fit between the respective limits. The fits to the peaks are breit-wigner functions convoluted with gaussians.

we made two different tests. For the first we divided the missing mass distribution in into the 5 regions shown in the top plot of figure 27. For each region we split the data into 12 bins in W and fitted the ϕ asymmetry with the both standard $\cos 2\phi$ expression used to extract photon asymmetry (14) and a polynomial of degree 0 (a horizontal line) and plotted the ratio of the $\chi^2/$ ndf value from each of the fits as a function of W. If the data in the bin has no photon asymmetry then the χ^2 / ndf for should be of the same order for both the $\cos 2\phi$ and straight line fits, and the ratio should be close to 1. A large photon asymmetry should result in a value much greater than 1. The results are shown in the bottom plot of figure 27. As would be expected, in the regions relating to the Λ and Σ^0 the ratio is high, indicating that there is a clear signal of a photon asymmetry. In the regions to the left of the Λ and to the right of the Σ^0 the ratio is low, indicating that there is no significant improvement in a $\cos 2\phi$ fit over a straight line fit. For the region between the two hyperon peaks the $\cos 2\phi$ fit is slightly better than a straight line due to the fact that the region is mostly background, but has some contribution from the tails of the hyperon peaks. Overall, the plot supports the hypothesis that the background has no
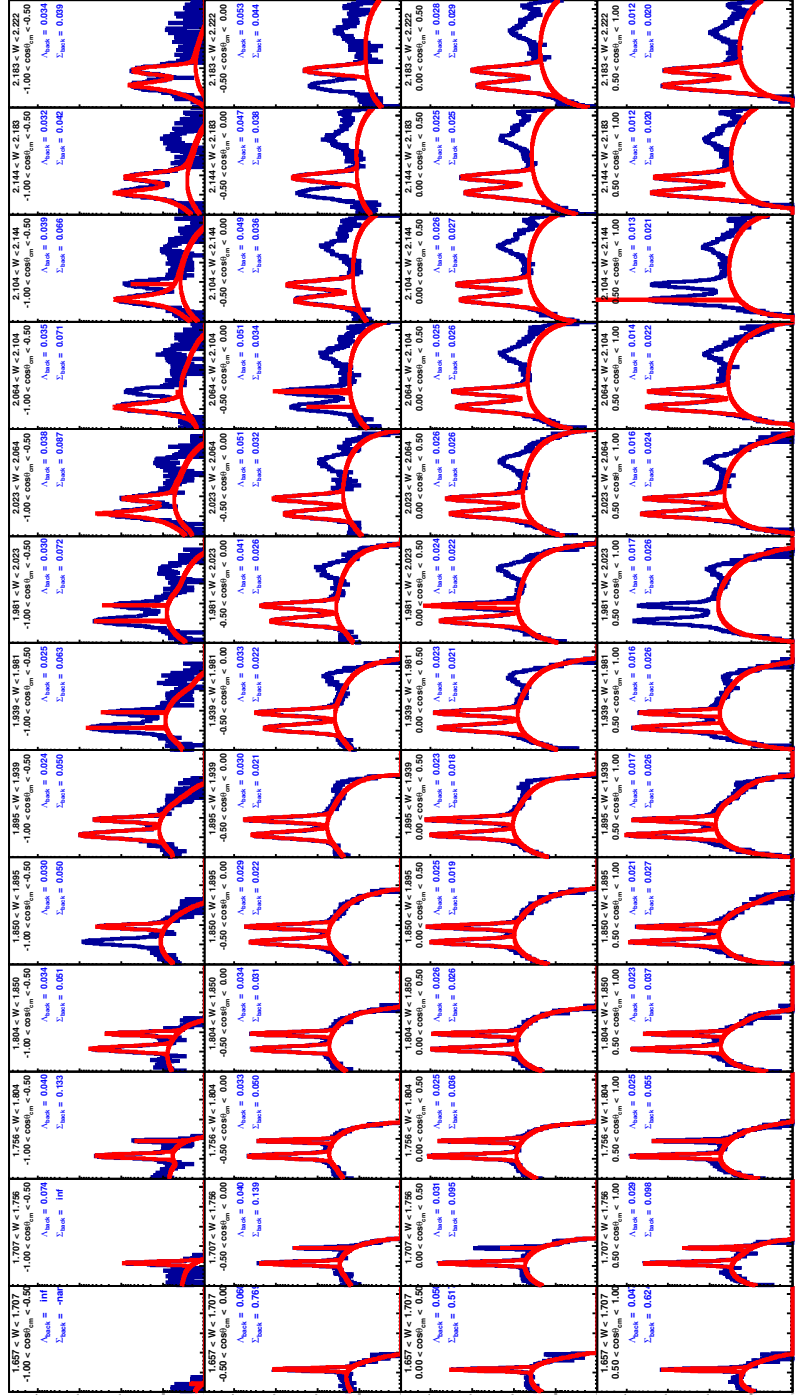
Figure 25. Measurement of the background under the Λ and Σ as a function of *W* and cos θ*cm*. The *W* and cos θ*cm* values for each bin, and the extracted background are shown in each plot. The higher rows of plots are at backward angles and the columns are increasing in *W* in the +ve *x* direction.
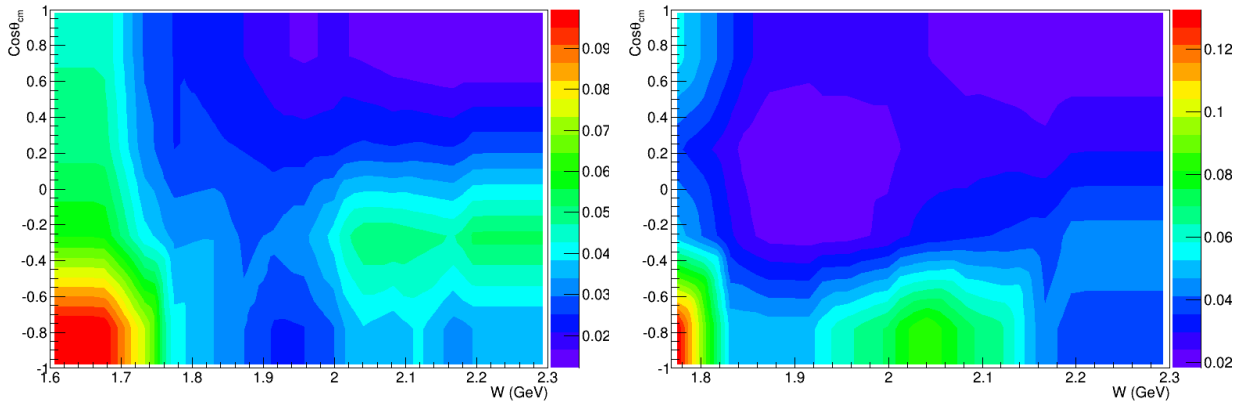
Figure 26. Background contribution under the Λ (Left) and Σ (Right) as a function of W ans $\cos\theta_{cm}$ calculated using the fitting method described in the text.

intrinsic photon asymmetry.

For the second test we compared the photon asymmetry for both hyperons using the standard 3σ cut shown in Figure 24 and with a much tighter cut ($1/5 \times 3\sigma$) to include a smaller background contribution. In both cases the *true* photon asymmetry was calculated on the assumption that the background had no photon asymmetry using the following expression:

$$\Sigma_{tot} = \frac{N_Y\Sigma_Y + N_{bg}\Sigma_{bg}}{N_{tot}}$$

where Σ_{tot} is the photon asymmetry measured from the $\cos 2\phi$ fit, Σ_Y, Σ_{bg} the photon asymmetry for the hyperon and background respectively and $N_{tot} = N_Y + N_{bg}$ where N_{tot} is the total number of counts in the peak, made up of the sum of the counts from the hyperon and background. In the case where the background is unpolarized, $\Sigma_{bg} = 0$ and this can be rewritten as:

$$\Sigma_Y = \frac{\Sigma_{tot}}{1 - B}$$

where B is the background under the hyperon, calculated as described above.

Overall, for both the Λ and Σ^0 the two sets of points are consistent given the size of the error bars. From the two studies shown in figures 28 and 29 we proceed to correct all data points on the assumption that there was no underlying photon asymmetry in the background events.
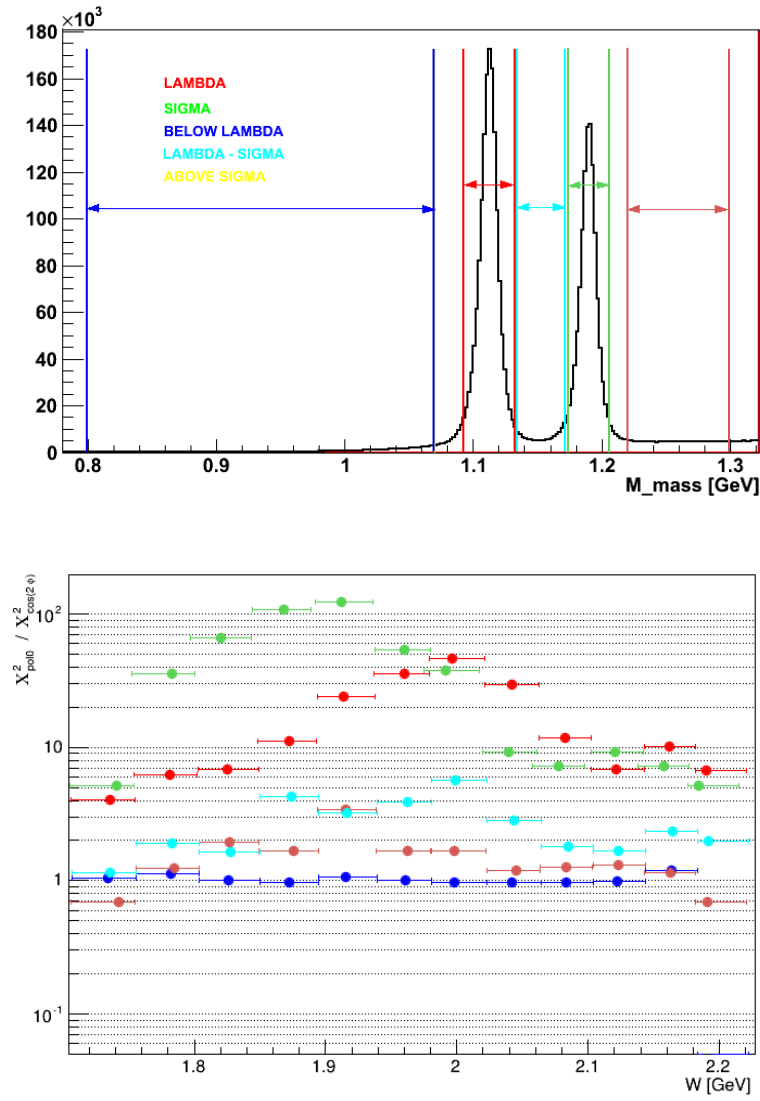
Figure 27. Top: the definition of 5 regions used to investigate the validity of the assumption that the background has no photon asymmetry. Bottom: ratio of χ^2/ndf for $\cos 2\phi$ and straight line fits for each of the regions defined in the top figure.
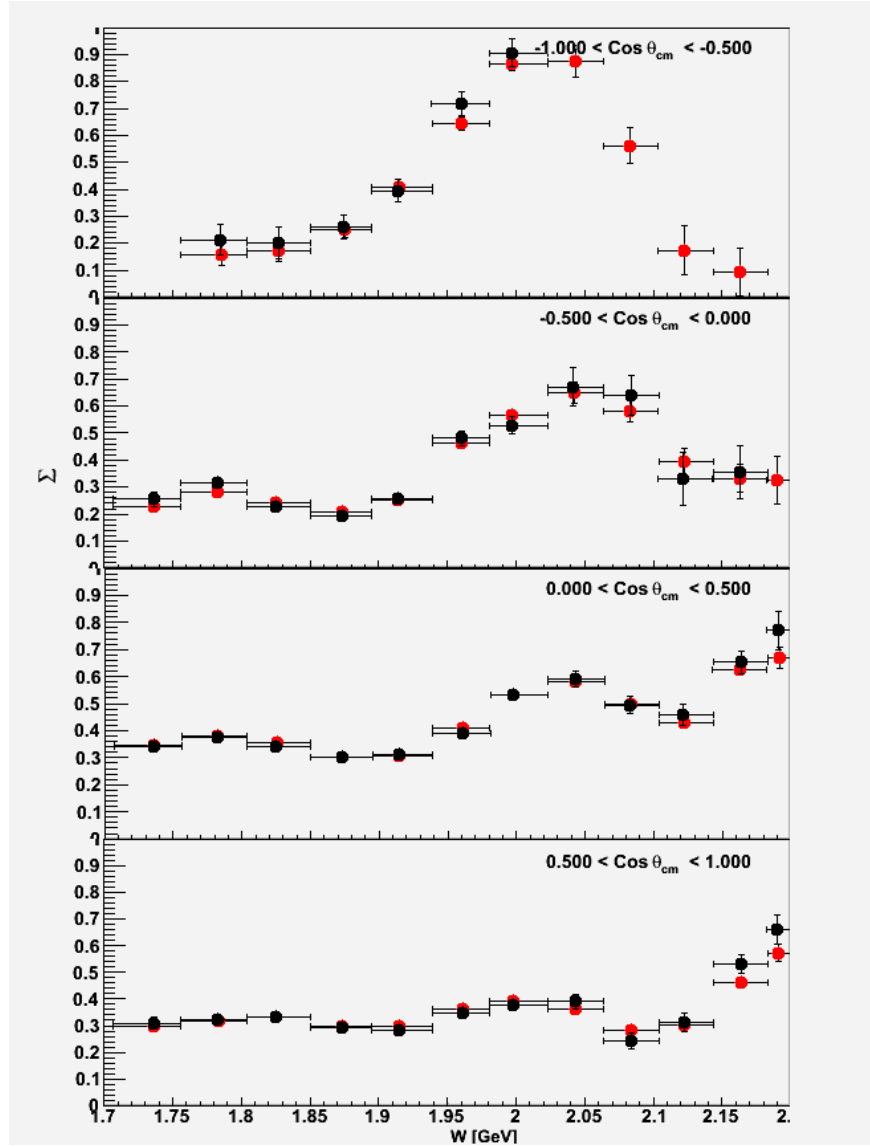
Figure 28. Photon asymmetry for the Λ corrected for background. The red points are based on the standard 3σ cut on the Λ peak and the black points are cut only on the central $1/5$ th of this.
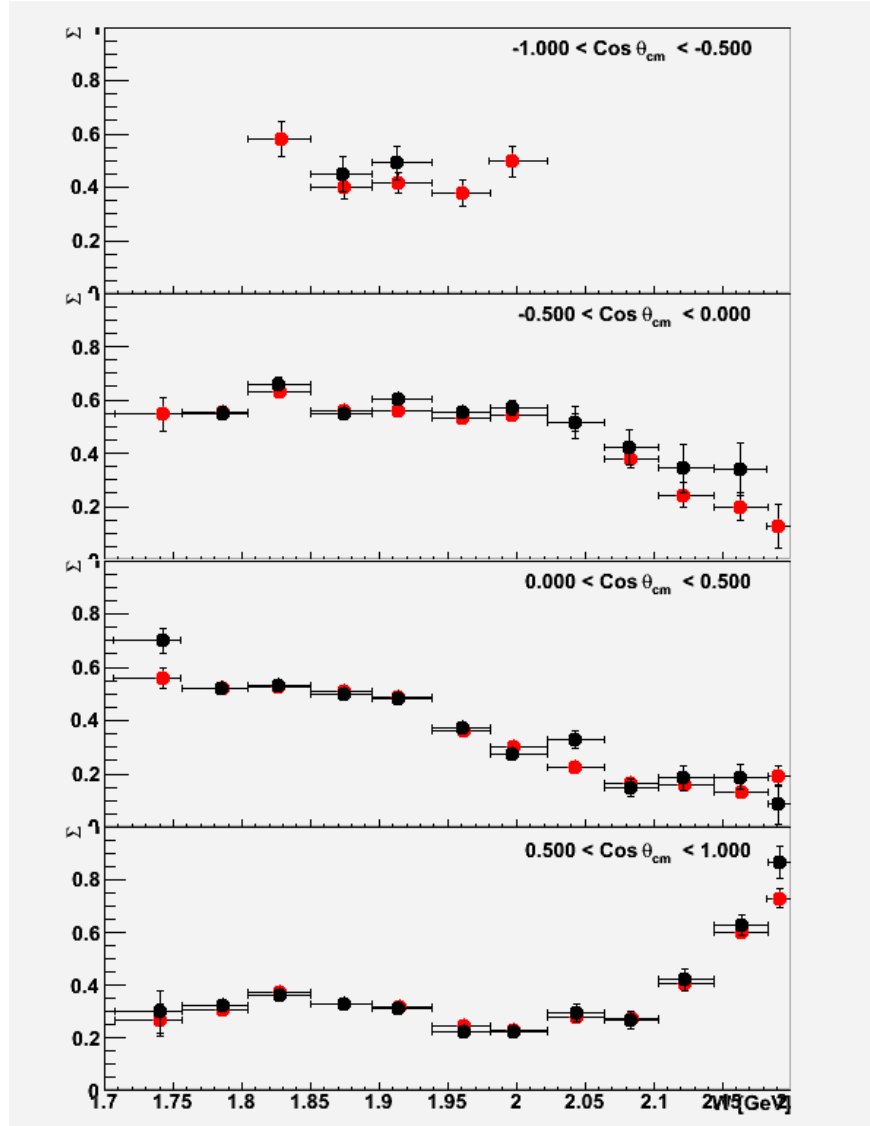
Figure 29. Photon asymmetry for the Σ^0 corrected for background. The red points are based on the standard 3σ cut on the Σ^0 peak and the black points are cut only on the central $1/5$ th of this.

D.   Unbinned fitting technique (Event-based Maximum Likelihood Estimates)

The event-by-event maximum likelihood (ML) method of extracting observables was documented in a previous CLAS Note [13]. In that note the program used here, EPO (Extraction of Polarization Observables), was described. Since this is the first time that the technique has been used in a CLAS analysis for determining polarization observables, we describe here the main points, taking some material from that analysis note. The main reason for using this technique is to enable a consistent set of observables to be extracted from the data.

For unbinned likelihood calculations, each event can in principle be assigned its own photon polarization (the best estimate for the photon polarization for that point in an experimental run - see section III). The expression for cross-section asymmetry (eq. (9)) then becomes

$$A\left(\xi\right) = \frac{P^{\gamma}g}{f}. \tag{15}$$

In other words there is no need to worry about different degrees of photon polarization for different polarization states; each event can treated as if there were a trial of both states with the same degree of polarization, but that one count was measured in only one of the states.

Including background

The events included in the fits may include background events. The number of events measured in each setting will be proportional to a combined cross-section

$$\sigma_{\perp}^{c} = \sigma_{\perp}^{s} + \sigma_{\perp}^{b}$$

and

$$\sigma_{\parallel}^{c} = \sigma_{\parallel}^{s} + \sigma_{\parallel}^{b},$$

where the subscripts c, s and b stand for combined, signal and background, respectively. As demonstrated in section IV C, we may assume that any asymmetries attributed to background events are zero, so that $\sigma_{\perp}^{b} = \sigma_{\parallel}^{b} \equiv \sigma^{b}$, say. This results at most in a small

632 dilution of the values of observables for the genuine signal events:

$$A = \frac{\sigma_\perp^c - \sigma_\parallel^c}{\sigma_\perp^c + \sigma_\parallel^c} = \frac{\sigma_\perp^s - \sigma_\parallel^s}{(1 + \beta)\left(\sigma_\perp^s + \sigma_\parallel^s\right)}, \tag{16}$$

633 where β is the background fraction (determined independently using the method de-
634 scribed in section IV C)

$$\beta = \frac{2\sigma^b}{\sigma_\perp + \sigma_\parallel}.$$

635 The expression for asymmetry then becomes slightly modified from eq (15) to be

$$A = \frac{P^\gamma g}{(1 + \beta) f}, \tag{17}$$

636 where f and g are the functions independent of, and dependent on ϕ, as defined above.

637 It is understood that the cross-sections used in the previously derived eq. (12) refer to
638 the combination of both signal and background, so the expression for A in eq. (11) should
639 be calculated from eq. (17).

640 Within one $\{W, \cos\theta_{CM}\}$ bin, there is a distribution in the variables $\xi \equiv \{\phi, x, y, z\}$,
641 the form of which allows us to estmate the polarization observables. Throughout such a
642 bin, we assume that there is an asymmetry $a(\xi) \in [-1, 1]$ for which ΔN is an estimator
643 in a range of the variables ξ. In a specified range of ξ, the probability of obtaining exactly
644 $N_\perp$ and $N_\parallel$ counts in the perpendicular and parallel settings respectively, given a specific
645 value of a would be

$$\mathcal{P}\left(N_\perp, N_\parallel \mid a\right) = \frac{1}{Z}(1 + a)^{N_\perp}(1 - a)^{N_\parallel}, \tag{18}$$

646 where Z is a normalizing constant. This probability density has mean $\frac{N_\perp - N_\parallel}{N_\perp + N_\parallel + 2}$ and mode
647 $\frac{N_\perp - N_\parallel}{N_\perp + N_\parallel}$.

648 Imagine now shrinking the range of ξ such that it contains one event. Equation 18
649 would then become

$$\mathcal{P}\left(N_\perp = 1, N_\parallel = 0 \mid a\right) = \frac{1}{2}(1 + a) \tag{19}$$

650 for a range with an event in the $\perp$ setting, and

$$\mathcal{P}\left(N_\perp = 0, N_\parallel = 1 \mid a\right) = \frac{1}{2}(1 - a) \tag{20}$$

651 for ranges with a $\parallel$ event.

⁶⁵²   *Likelihood Function*

⁶⁵³   The likelihood function is the probability that a data set would be obtained, given a
⁶⁵⁴ specific set of parameters. In this case the parameters are the observables, which we now
⁶⁵⁵ denote $\mathcal{O} \equiv \{\Sigma, P, T, O_{x'}, O_{z'}\}$, and other quantities referred to as "nuisance parameters"
⁶⁵⁶ $\lambda \equiv \{P_L^\gamma, \Delta L, \delta\phi\}$. The nuisance parameters represent quantities that must be determined
⁶⁵⁷ independently and that can affect systematic uncertainties. We label each event E_i and
⁶⁵⁸ $\{E_i\}$ represents a set of data. The total likelihood is a product of likelihoods for individual
⁶⁵⁹ data E_i:

$$\mathcal{P}\left(\{E_i\} \mid \mathcal{O}, \lambda\right) = \prod_i \mathcal{P}_i\left(E_i \mid \mathcal{O}, \lambda\right) \tag{21}$$

⁶⁶⁰   So for each event equation (19) or (20) is used, depending on the setting ($\perp$ or $\parallel$).
⁶⁶¹ The a in the equations is equal to the estimator ΔN in equation (11), and the quantity
⁶⁶² A appearing in equation (11) is determined from equation (17). The functions f and g
⁶⁶³ in equation (15) are dependent on variables ξ, parameters $\mathcal{O}$ and λ. By maximizing the
⁶⁶⁴ likelihood, we therefore obtain the most likely values of the observables. This is done
⁶⁶⁵ by using Minuit, from which we obtain values, parabolic errors, asymmetric errors (from
⁶⁶⁶ MINOS) and a covariance matrix if desired.

⁶⁶⁷   In practice, whereas recoil polarization P appears in the denominator of equation (15),
⁶⁶⁸ it was found that a reliable value of P could not be extracted by considering asymmetries
⁶⁶⁹ alone. Instead, the distribution of intensity as a function of the direction cosine $\cos\theta_y \equiv y$
⁶⁷⁰ in the Λ rest frame can be used to extract P. The probability for an event at y is

$$\mathcal{P}\left(y \mid P\right) = \varepsilon\left(y\right)\left(1 - \alpha y P\right)$$

⁶⁷¹ where $\epsilon\left(y\right)$ is the acceptance, and is calculated with simulations as described in appendix
⁶⁷² B.

⁶⁷³   For an extraction from g8 data, an estimate of P is required first, either by an event-
⁶⁷⁴ by-event maximum likelihood fit or using an externally measured value as input. This
⁶⁷⁵ yields an estimate $P = p_0$ with error $\pm\delta p_0$. A likelihood for the recoil polarization $\mathcal{P}\left(P\right)$
⁶⁷⁶ is then a Gaussian, or Normal probability density

$$\mathcal{P}\left(P\right) = \mathcal{N}\left(P \mid \mu = p_0, \sigma = \delta p_0\right).$$

⁶⁷⁷ This is multiplied into the probability for asymmetry

$$\mathcal{P}_i\left(E_i \mid \mathcal{O}, \lambda\right) \rightarrow \mathcal{P}_i\left(E_i \mid \mathcal{O}, \lambda\right)\mathcal{N}\left(P \mid \mu = p_0, \sigma = \delta p_0\right), \tag{22}$$

678 so that some variation in the value of P is allowed in the likelihood fitting of the asymmetry, but in a more constrained fashion. As will be seen later, an external value (with uncertainty) of P can be used alternatively to define the mean and width of the normal distribution.

682 *Including Prior Information*

683 Equation (22) is sufficient to determine estimates of observables. However, just as kinematic fitting allows the known physics constraints of energy and momentum conservation to be taken into account, we can make use of the physics of pseudoscalar meson photoproduction to extract values that we know to be physical and consistent with each other. In the first place, we know that all the parameters to be determined are themselves asymmetries of cross-sections (in different combinations of spin projections), and are thus bounded in $[-1, +1]$. We also know (e.g. from [15]) that there are additional constraints. In our case, we have:

$$R^2 + O_x^2 + O_z^2 \leq 1, \tag{23}$$

$$B^2 + O_x^2 + O_z^2 \leq 1, \tag{24}$$

$$|T - R| \leq 1 - B; \quad |T + R| \leq 1 + B, \tag{25}$$

$$O_x^2 + O_z^2 + C_x^2 + C_z^2 + B^2 - T^2 + R^2 = 1. \tag{26}$$

694 These constraints severely limit the space of possible observable values. For example, eqn. (25) results in a physical region of $\{\Sigma, P, T\}$ parameter space that is a tetrehedron, with a volume that is only $\frac{1}{3}$ of $[-1, +1]^3$. While we do not measure C_x and C_z with linearly polarized photons, we can use (26) to give an inequality

$$O_x^2 + O_z^2 + B^2 - T^2 \leq 1 - R^2, \tag{27}$$

699 since $C_x^2 + C_z^2 + R^2 \leq 1$.

700 The likelihood function is actually the probability of the data given the parameters, whereas what we really want is the probability of the parameters, given the data. This is given by the posterior probability

$$\mathcal{P}\left(\mathcal{O} \mid \{E_i\}\right) \propto \mathcal{P}\left(\{E_i\} \mid \mathcal{O}\right) \mathcal{P}\left(\mathcal{O}\right), \tag{28}$$

703 where we do not care about the normalizing constant, since the function is to be maxi-
704 mized. So at the time of evaluating the likelihood, the conditions defined by equations
705 (23-27), as well as the bounds $[-1, +1]$ can be encoded into a prior probability function
706 $\mathcal{P}(\mathcal{O})$. This means our fit will yield a maximum posterior probability estimate of the
707 observables. What is actually done is to perform an unconstrained fit without the prior
708 (maximum likelihood) to check whether there may be systematic uncertainties associated
709 with the evaluation of the nuisance parameters, then a constrained fit (maximum poste-
710 rior probability) is carried our to yield the final numbers. As will be seen later, there is
711 almost no difference in the two results across the entire kinematic region, which is a good
712 indication that the information about observables in mostly contained in the measured
713 data, as opposed to any prior assumptions.

714   A full Bayesian analysis would require marginalising over the nuisance parameters λ.
715 What we do is to look at the effect of changing these parameters from best-estimate val-
716 ues by given amounts to understand the sensitivity of the results to what are systematic
717 uncertainties.

718   **E.   Data Range in W and $\cos \theta$**

719   The range of data passing all PID cuts is depicted in figures 30 and 31, where data
720 from all coherent beam settings have been amalgamated. Note that the distribution of
721 the number of events reflects a combination of CLAS acceptance, photon energy distri-
722 butions and physics. Unless stated explicitly the events used are 2-track final state events
723 (measured Kaon and proton), but 3-track events (measured Kaon, proton and pion) were
724 also analysed to investigate consistency.

725   In order to display the extracted results, the kinematic region in $\{W, \cos \theta\}$ needs to
726 be divided up into discrete bins. The bins must be chosen such that there are sufficient
727 events in each to effect a reasonable fit, whilst keeping them small enough to be able to
728 discern the variation in observables over the region.

729   It can be seen from figures 30 and 31 that a regularly spaced rectangular grid would
730 lead to very different numbers of events in each bin. To display angular distributions we
731 require bins with a common range of W, whilst for W distributions we need to be able
732 to define common ranges in $\cos \theta$. In addition to this, it was noted during several trial
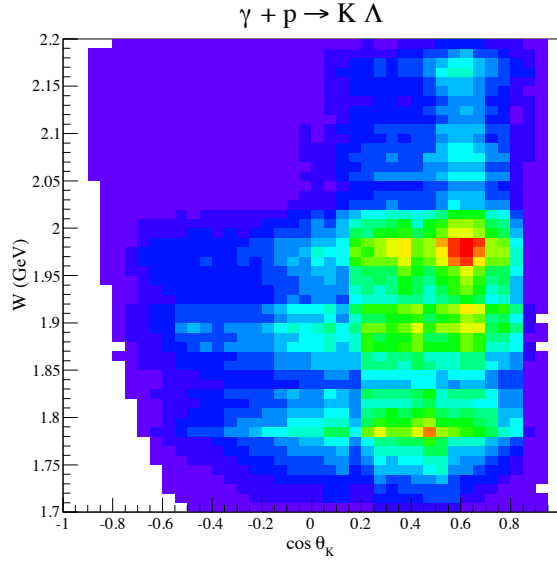
Figure 30. Data used in the extraction of observables for the $K\Lambda$ channel.
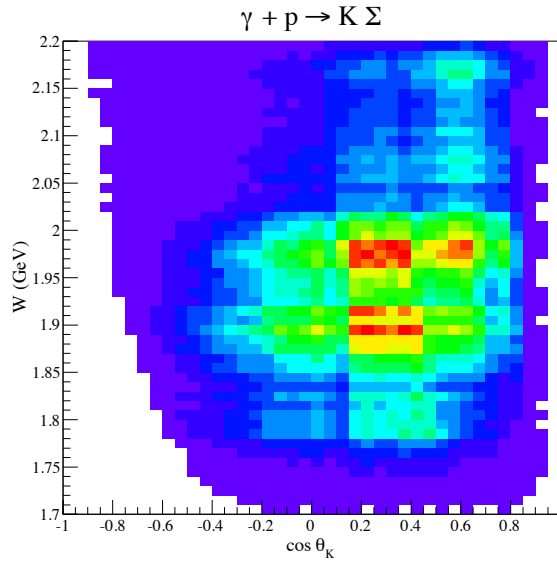

Figure 31. Data used in the extraction of observables for the $K\Sigma^0$ channel.

733 extractions that for the $K\Lambda$ channel, a minimum of 1000 events were required to enable
734 a sensible fit, whilst for the $K\Sigma^0$ channel that number was more like 3000. This can be
735 understood by the fact that for the $K\Sigma^0$ channel, since the polarization carried by the Σ is
736 only accessible through the decaying Λ, the effective weak decay constant is diluted by
737 factor of -0.256 compared to the $K\Lambda$ channel [1], requiring roughly four times more events
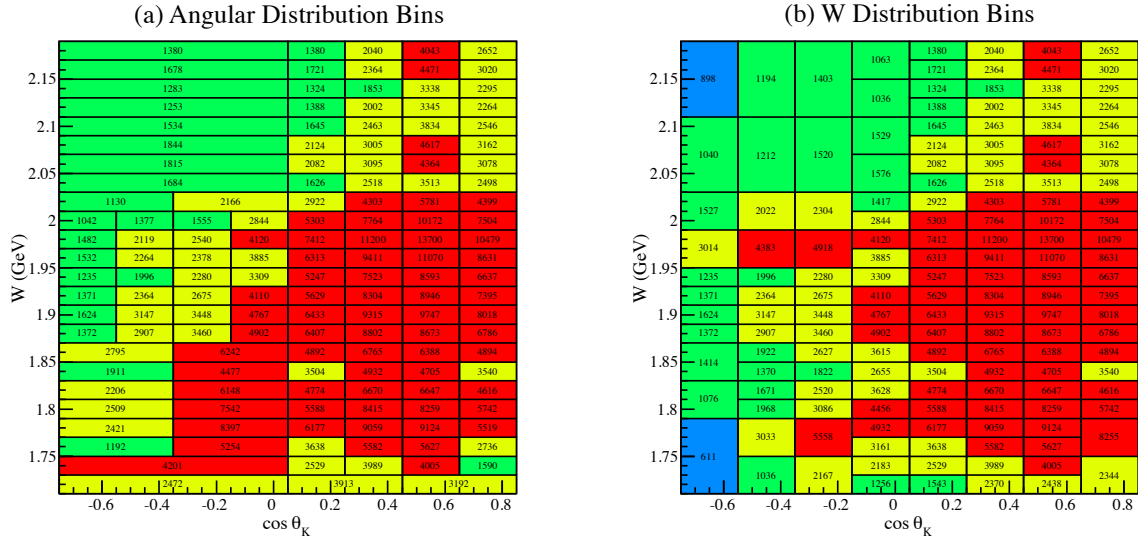
Figure 32. Bins defined for $\gamma p \rightarrow K\Lambda$ events

738 to achieve the same level of accuracy. Note that in both cases the events form a distribu-

739 tion of points in a 4-dimensional space ($\{\xi\} = \{\phi_K, x, y, z\} = \{\phi_K, \cos\theta_x, \cos\theta_y, \cos\theta_z\}$).

740 The partitioning of $\{W, \cos\theta\}$ was carried out by defining a grid of small bins, and

741 successively adding them together to obtain bins that contain enough counts for the fit-

742 ting process. The results of this process can be seen in figures 32 and 33. The bins defined

743 in the (a) panels are used for angular distributions (i.e. the bins are all the same width in

744 W), and the bins defined in the (b) panels are used for energy (W) distributions (i.e. the

745 bins are all the same width in $\cos\theta$). Bins colored blue contain too few events, and are

746 therefore discarded in the extraction of observables.

747 **F. Basic fitting procedure**

748 Before estimates of observable values can be extracted, the "nuisance" parameters P^γ

749 (degree of photon beam polarization), ΔL (asymmetry in luminosity between the two

750 photon polarization settings) and $\delta\phi$ (goniometer offset) need to be evaluated. A descrip-

751 tion of how to evaluate P^γ as a function of photon energy and goniometer setting ($\parallel$ or

752 $\perp$) was given in section III. For this analysis we assume that $\delta\phi = 0$. It has been de-

753 termined in other g8 analyses [11][cite Mike Dugger's note] that this quantity is indeed

754 consistent with zero. We subsequently investigate the effect of a non-zero $\delta\phi$ as part of
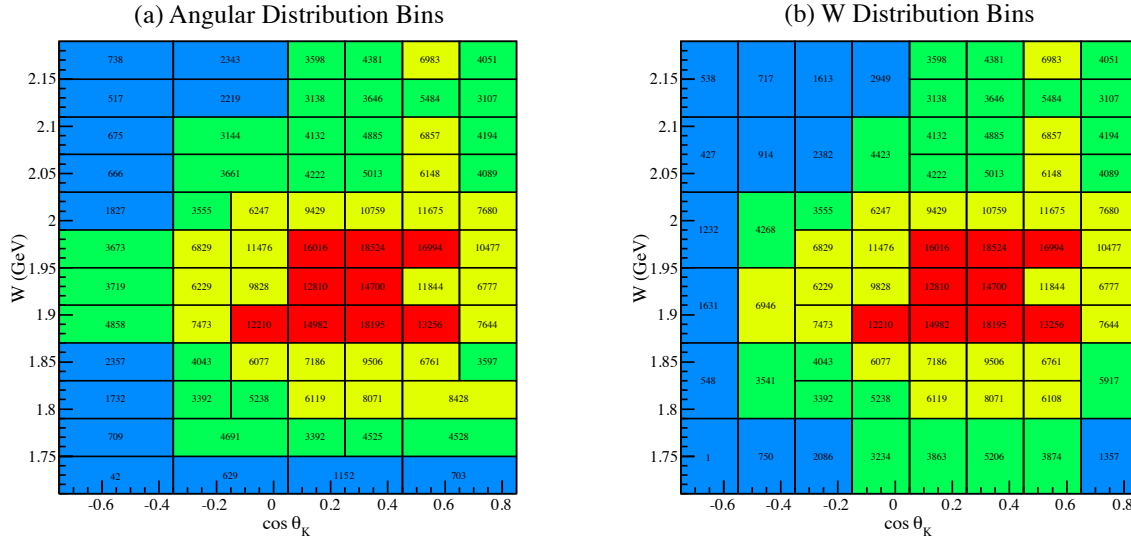
Figure 33. Bins defined for $\gamma p \rightarrow K\Sigma^0$ events

the systematic studies.

This just leaves the luminosity asymmetry ΔL. It is going to be different for each bin in W. We can see from equation (11) that it could be a free parameter in a fit to the asymmetry in counts ΔN. However, since it will only vary in W and not $\cos\theta$, we first perform a fit for all events in a W-range (horizontal lines in figures 32 and 33), then fix ΔL ($W \in [W_0, W_1]$), where W_0 and W_1 delimit a range, for all bins in $\cos\theta$ in that W range.

It can be seen from figures 32 and 33 that a variety of W bin widths are required. Maximum likelihood fits were carried out for events over the entire range of $\cos\theta$, where the ΔL parameter was left as a free parameter. Values extracted for $K\Lambda$ events are shown in figure 34. They range from roughly -0.2 to +0.2, and can be quite different from one bin to the next. Subsequent fits at specific values of $\cos\theta$ use these values as fixed parameters. Similar fits were done for $K\Sigma^0$ events, as well as 3-track events in both $K\Lambda$ and $K\Sigma^0$ channels, all of which are consistent with each other.

With the bins for the two reactions defined as shown in figures 32 and 33, a maximum likelihood fit was carried out for each bin, both in the unconstrained and constrained versions. Where MINOS errors are calculated, the error bars for each observable are asymmetric. In some cases a MINOS calculation will fail. This happens only for constrained fits, and is likely to be because the optimum values are close to a physical limit,
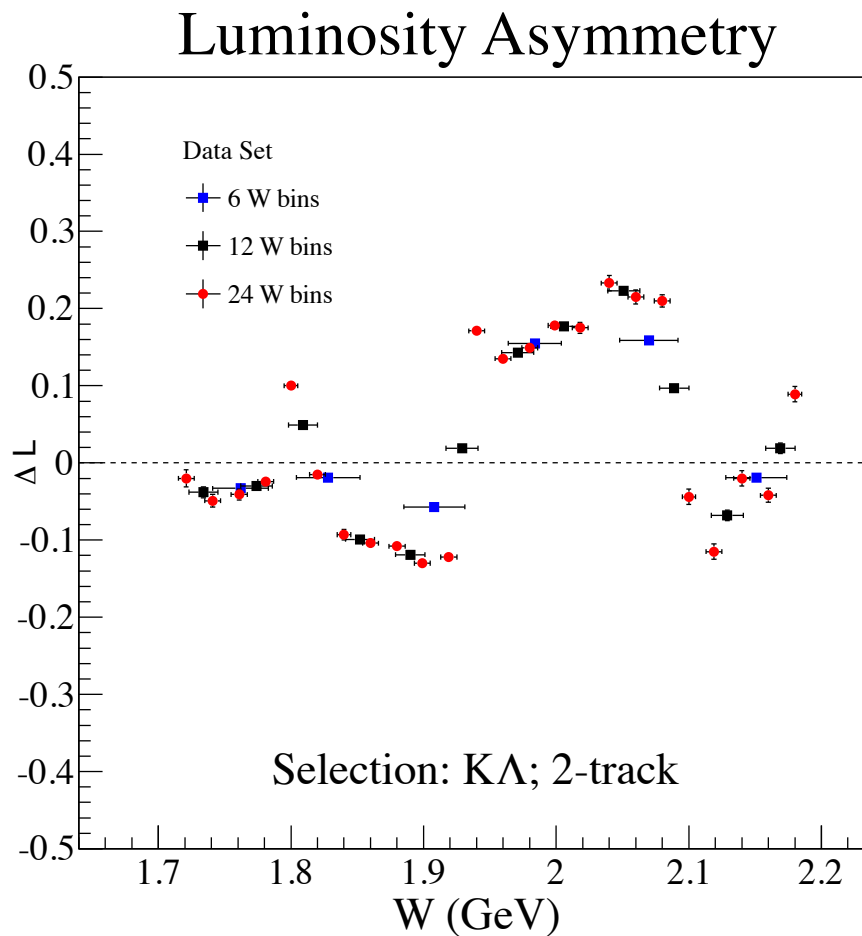
Figure 34. Calculated values of ΔL from fits to bins of varying widths.

773 so that the constraint functions give rise to a shape in the likelihood surface that is far
774 from parabolic. In the case of constrained fits where MINOS has failed, the parabolic
775 error returned by MINUIT is used.

776 V.   COMPARISON WITH PUBLISHED DATA

777   To establish the correctness of the g8 data, several comparisons are possible with pre-
778 viously published data. These data come from six different sources:

779   1. CLAS g11 [16, 17]

780   2. CLAS g1c [1]

781   3. LEPS [18]

782   4. GRAAL [19, 20]

783 All the data sets have a different kinematic coverage, and were sensitive to different ob-
784 servables. Table III gives an indication of the measurements performed and reported by
785 the different experiments.

Experiment	Final State	W range (GeV)	Σ	P	C_x	C_z	T	O_x	O_z
CLAS g11	$K\Lambda$	1.62 - 2.84	-	$\star$	-	-	-	-	-
	$K\Sigma^0$	1.69 - 2.84	-	$\star$	-	-	-	-	-
CLAS g1c	$K\Lambda$	1.68 - 2.74	-	$*$	$*$	$*$	-	-	-
	$K\Sigma^0$	1.79 - 2.74	-	$*$	$*$	$*$	-	-	-
LEPS	$K\Lambda$	1.94 - 2.30	$\star$	-	-	-	-	-	-
	$K\Sigma^0$	1.94 - 2.30	$\star$	-	-	-	-	-	-
GRAAL	$K\Lambda$	1.64 - 1.92	$\star$	$\star$	-	-	$\star$	$\star$	$\star$
	$K\Sigma^0$	1.74 - 1.92	$\star$	$\star$	-	-	-	-	-
CLAS g8	$K\Lambda$	1.71 - 2.19	$\star$	$\star$	-	-	$\star$	$\star$	$\star$
	$K\Sigma^0$	1.75 - 2.19	$\star$	$\star$	-	-	$\star$	$\star$	$\star$

Table III. Measurements performed by the different experiments.

786   The CLAS g11 data set covers the whole range of the g8 data set in $\{W, \cos\theta\}$. A
787 comparison of the kinematic coverage of the g8 dataset with the LEPS and GRAAL ex-
788 periments is represented in figures 35 and 36. Taken together with the information in
789 table III, it is readily seen that the g8 dataset significantly extends the amount of world
790 data for polarization observables for these two channels in the resonance region.
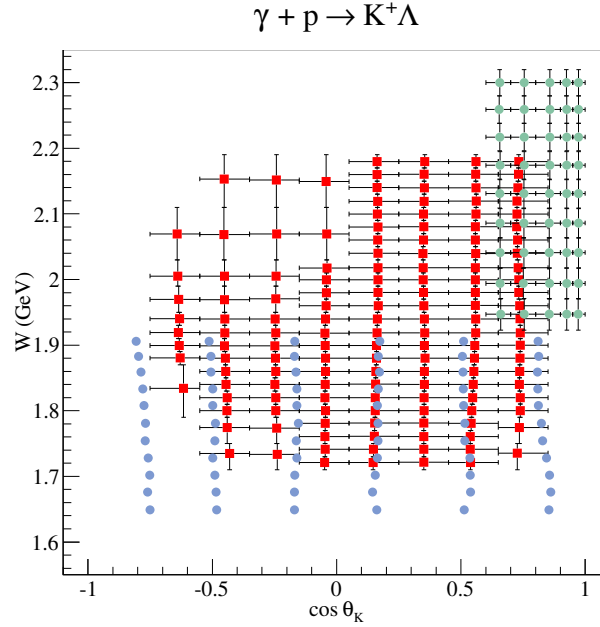
Figure 35. Comparison of kinematic coverage for $\gamma p \rightarrow K\Lambda$. Red squares - g8; green circles - LEPS; blue circles - GRAAL. The g8 and LEPS dataset error bars represent the limits of the bins in $\{W, \cos\theta\}$.
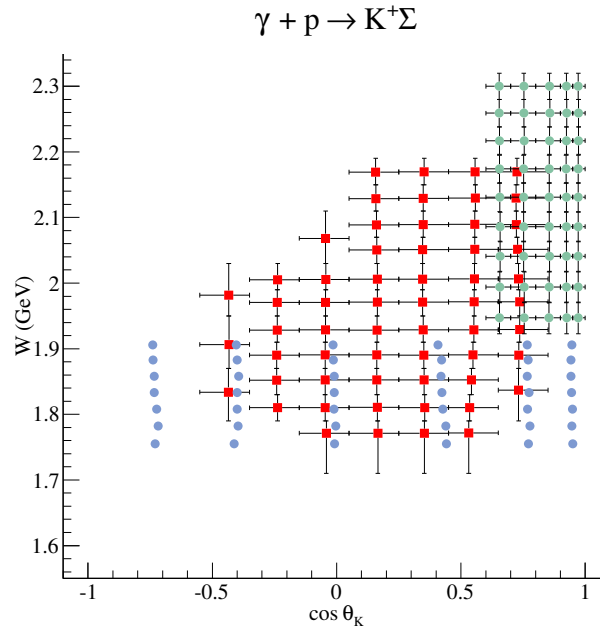
Figure 36. Comparison of kinematic coverage for $\gamma p \rightarrow K\Lambda$. Symbols are defined in figure 35.

A.   Previous CLAS measurements - Recoil Polarization

Comprehensive data sets that include recoil polarizations for both $K\Lambda$ and $K\Sigma^0$ reactions have already been published by CLAS [16, 17]. These data have higher granularity and larger coverage than g8, so the best we can do is look at comparisons in the overlapping range of W and $\cos\theta$. In particular, what we do for a comparison here is to use the bins defined in figures 32 (a) and 33 (a) for angular distributions. Each of the bins spans two W bins in the g11 data set, so data from two g11 bins are used in the plotted comparisons. The comparisons of g11 recoil polarizations with g8 data extracted from constrained maximum likelihood fits are shown in figures 37 and 38.

The overall agreement with g11 $K\Lambda$ data is excellent. The two methods of extracting recoil polarization are very different, and the data come from two different run periods, so this level of agreement is very reassuring.

A comparison of recoil polarizations for the $K\Sigma^0$ channel is shown in figure 38. The agreement for this channel is fair, but shows significant discrepancies for forward kaon angles at the higher energies. Similar discrepancies between recoil polarization results from g1c and g11 were seen in [17]. The discrepancies between g1c and g11 have been attributed to the sophistication of the simulations for acceptance calculations. Whilst a study of acceptance corrections for g8 was carried out, as reported in appendix B, the event generator was simply phase space for the final state particles. The recoil polarization is the only observable for which an acceptance calculation is required in our data.

In order to remove this potential source of inconsistency (which only occurs in $K\Sigma^0$ at forward angles at the highest measured energies), we have decided not to report recoil polarizations from this data set, and to rely on the g11 results for that observable, as input for the fits to extract the other observables via asymmetries. Indeed, it was never intended that g8 recoil polarization data would be used in future phenomenological fits, since the g11 data has finer resolution in W and $\cos\theta$. However, we can make use of the very accurate determinations of recoil polarization for both $K\Lambda$ and $K\Sigma^0$ from g11, so we adopt the following procedure. We take a value of recoil polarization from the g11 results by extrapolating the values to the bin centers of our g8 bins. We also interpolate the statistical error. We then use these as the mean and standard deviation of the gaussian PDF that multiplies the likelihood function, as described in IV D. We refer to this from

now on as using *external* recoil polarizations, as opposed to *internal* recoil polarizations that would be derived from fits to g8 data.

We do want to check that the use of external polarizations does not affect the extracted values of the other observables. Extractions of observables were therefore carried out using both internal and external recoil polarizations, and the results compared. There is no discernable difference for the $K\Lambda$ channel, as one would expect from the almost identical values of recoil polarizations shown in figure 37. The main worry is the $K\Sigma^0$ channel, which we illustrate in figures 39 and 40. Rather than showing every result, figure 39 shows the most favourable comparison (beam asymmetry, Σ), whilst figure 40 shows the least favourable example (target polarization, T).

The average difference is less than 1% for all observables in the $K\Lambda$ channel. For the $K\Sigma^0$ channel, the average differences are less than 1% for Σ and O_z, whilst only the T and O_x observables show differences of up to $\pm9\%$ and $\pm4\%$ respectively, but these are not large when compared with statistical uncertainties. We therefore proceed by using the external recoil values for all other results.
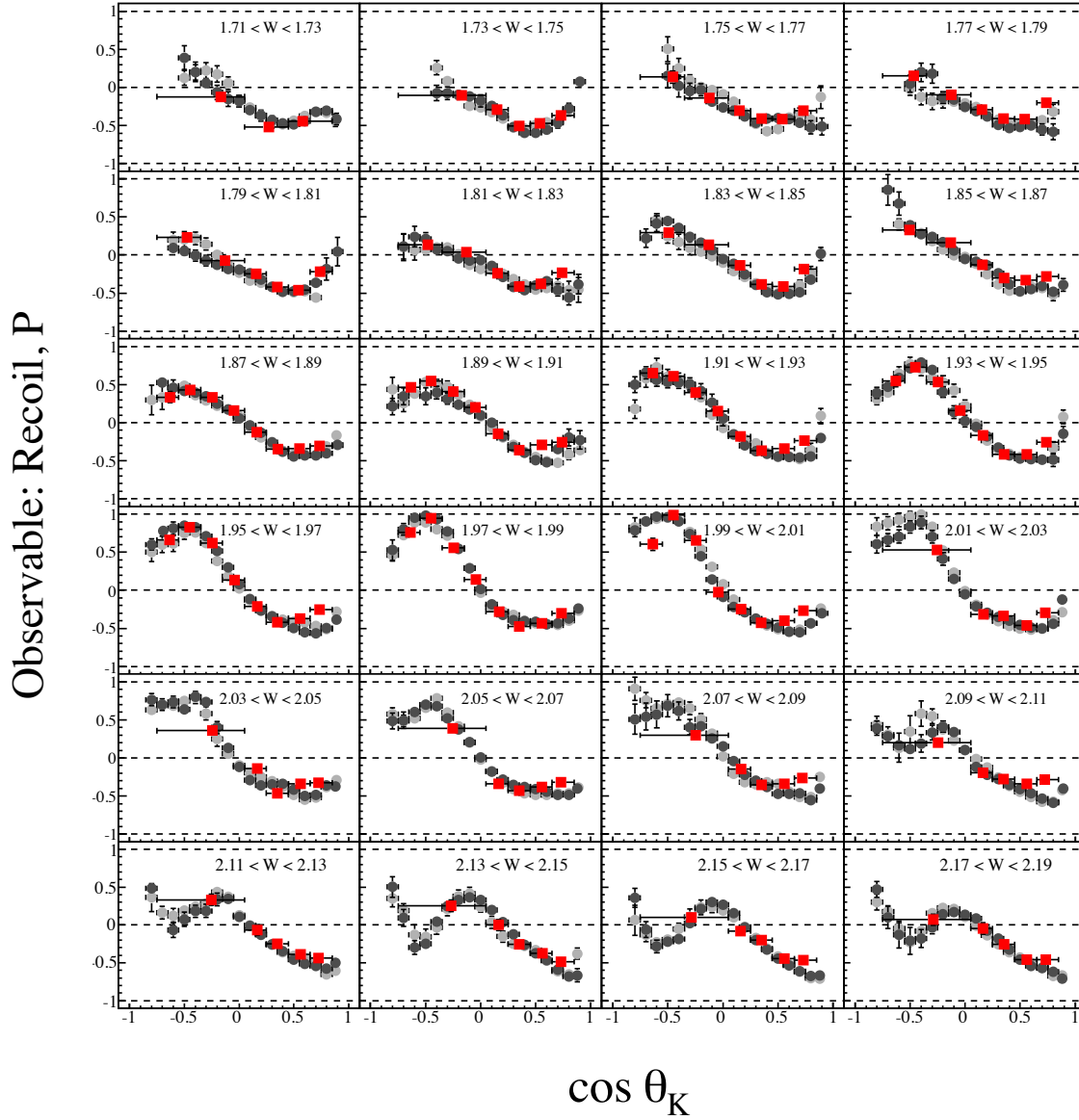
Figure 37. Comparison of recoil polarization *P* between g8 (red squares) and g11 (light grey - data for *W* values in bottom half of region quoted; dark grey - data for *W* values in top half of region quoted).
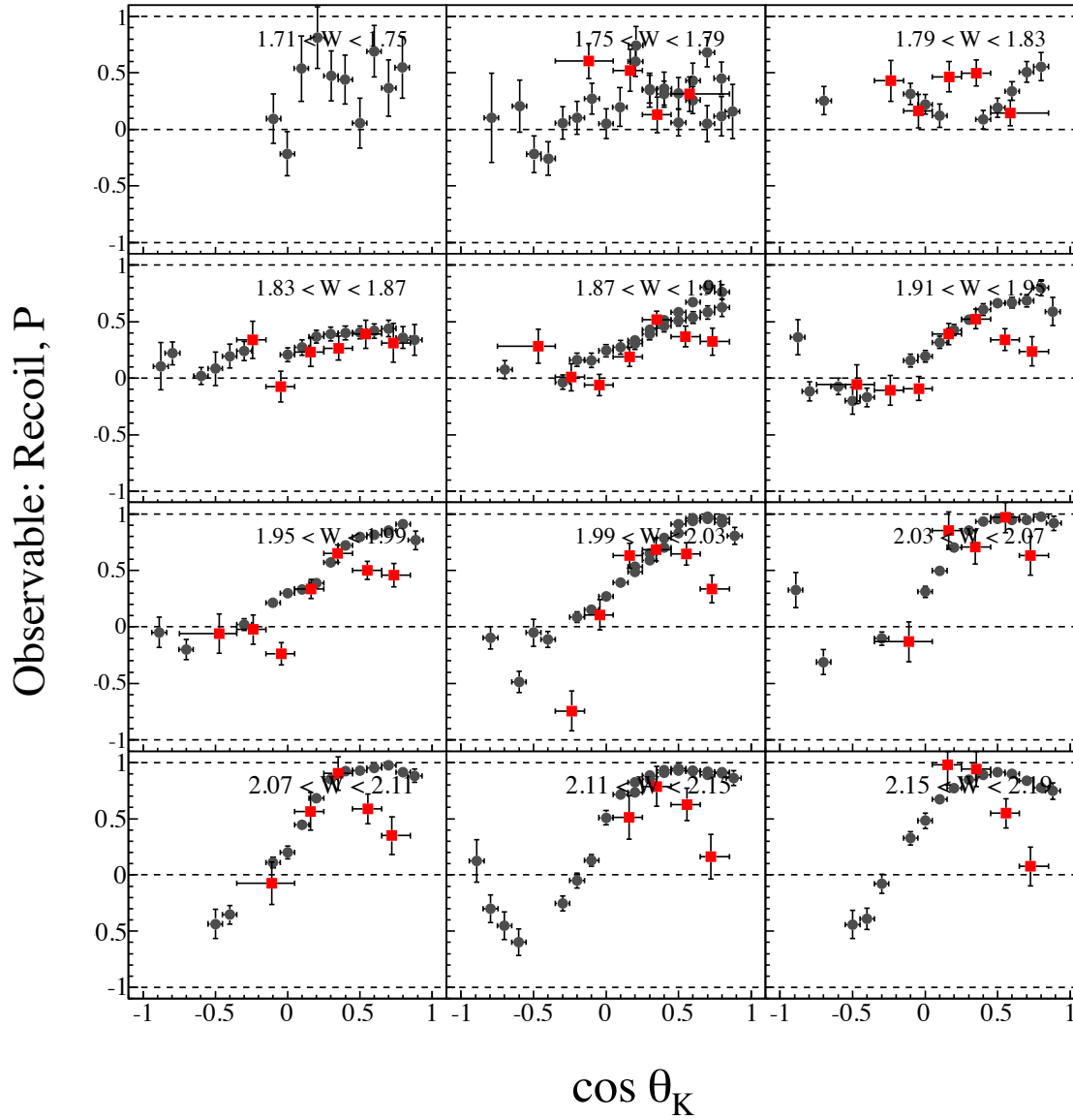
Figure 38. Comparison of recoil polarization P between g8 (red squares) and g11 (dark grey circles) Each plot in this comparison shows all the g11 data that are contained within a 40 MeV bin in W.

$$\gamma + p \rightarrow K^+ \Sigma$$
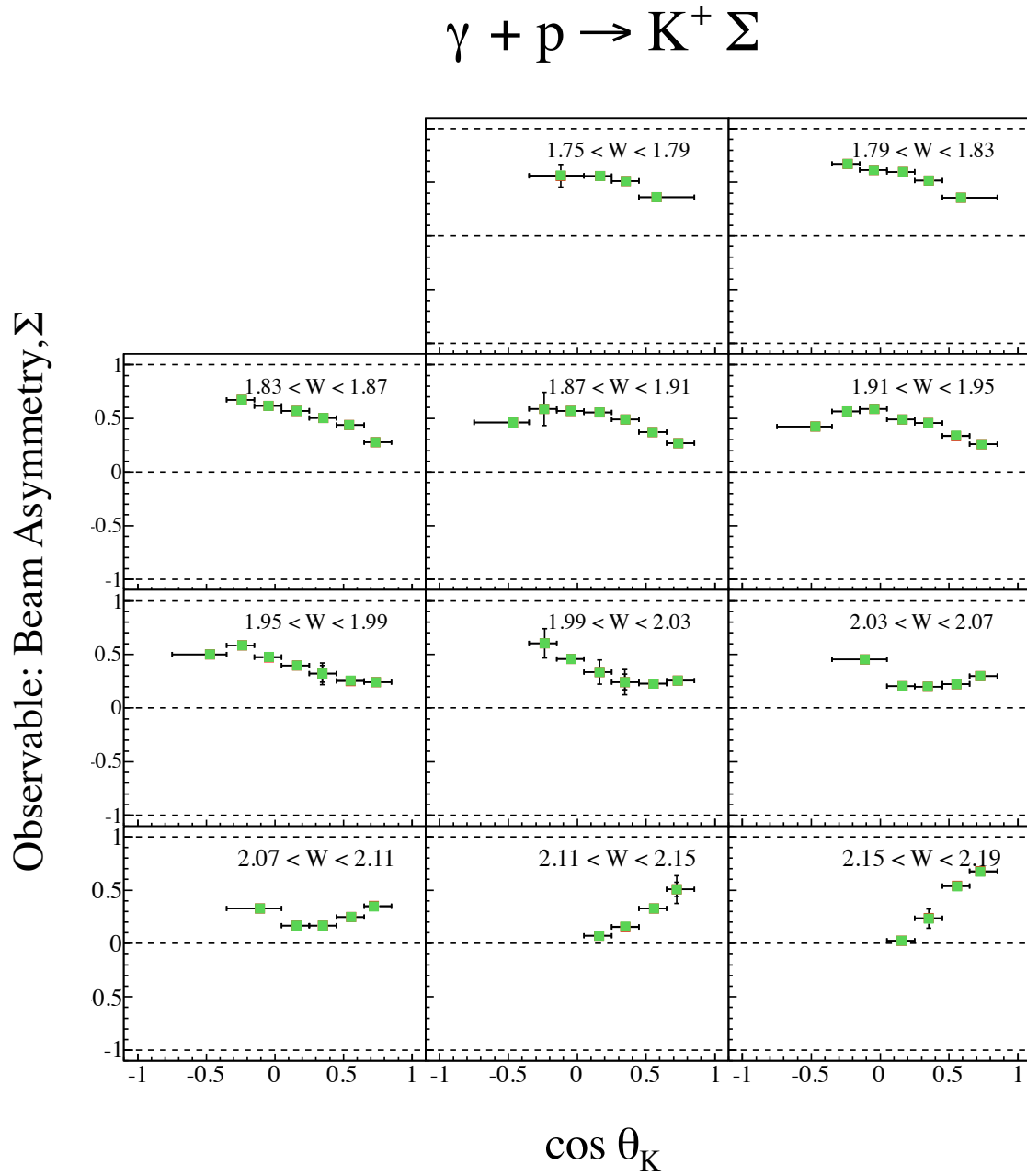
Figure 39. Effect of using g11 recoil polarizations as input to g8 extraction of beam asymmetry for the $K\Sigma^0$ channel. Green data points - using recoil polarizations calculated from g8 data; Red data points (barely seen in these plots) - using g11 recoil polarizations.
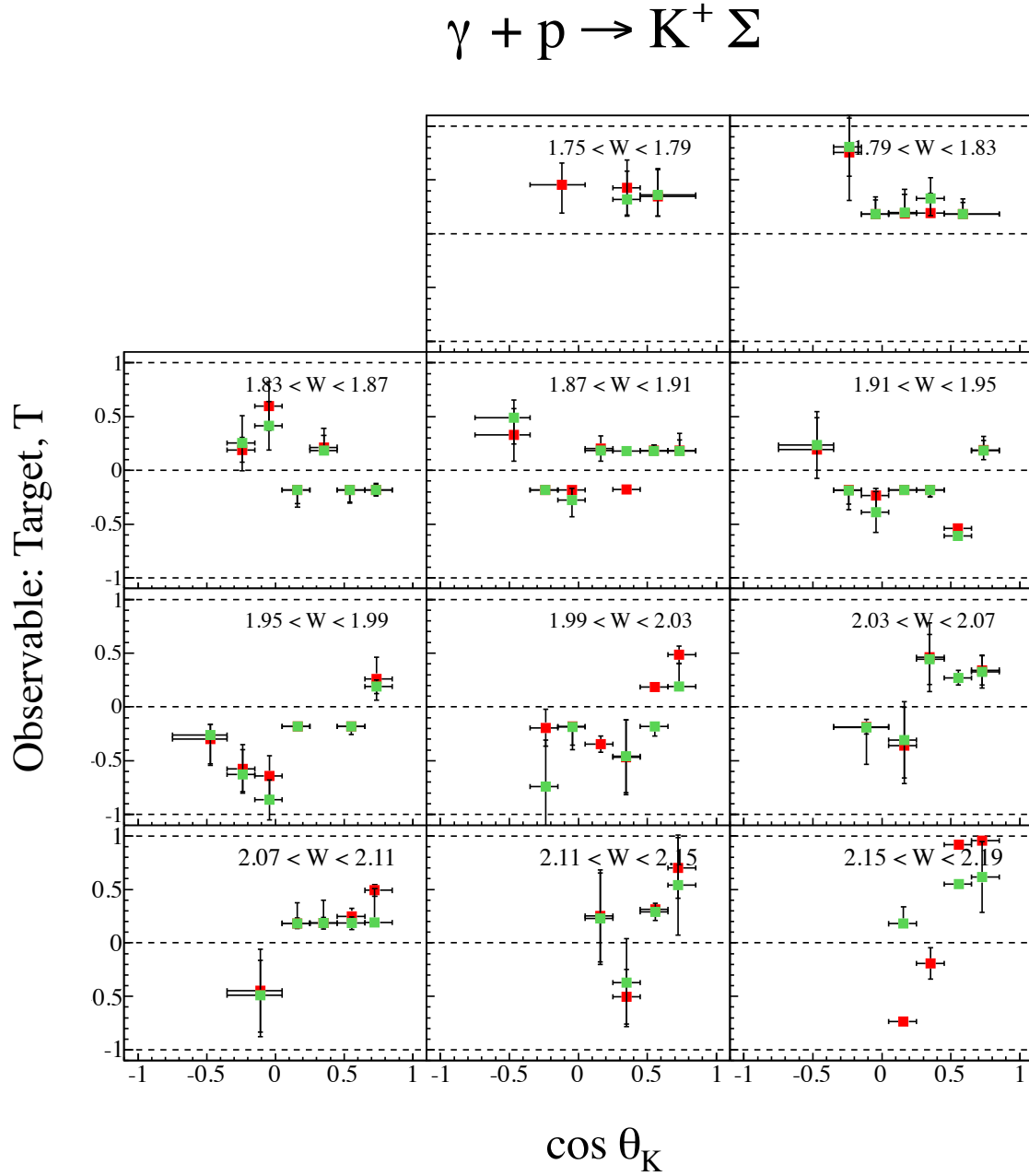
Figure 40. Effect of using g11 recoil polarizations as input to g8 extraction of target asymmetry *T* for the $K\Sigma^0$ channel. Green data points - using recoil polarizations calculated from g8 data; Red data points - using g11 recoil polarizations.

B.   LEPs measurements - Beam Asymmetry

The LEPS data only cover forward angles [18], and a range of W that extends a little beyond the g8 W reach. For these comparisons, bins were defined for the g8 data that closely matched the W bins of the LEPs data, and the results are displayed in figures 41 and 42. A comparison of the coverage can be seen in the bottom right panel in these figures.

For both channels the results are consistent, but the g8 results cover a much larger range of scattering angle and have greater statistical accuracy.

g8-LEPS comparison: $\gamma + p \rightarrow K^{+}\Lambda$
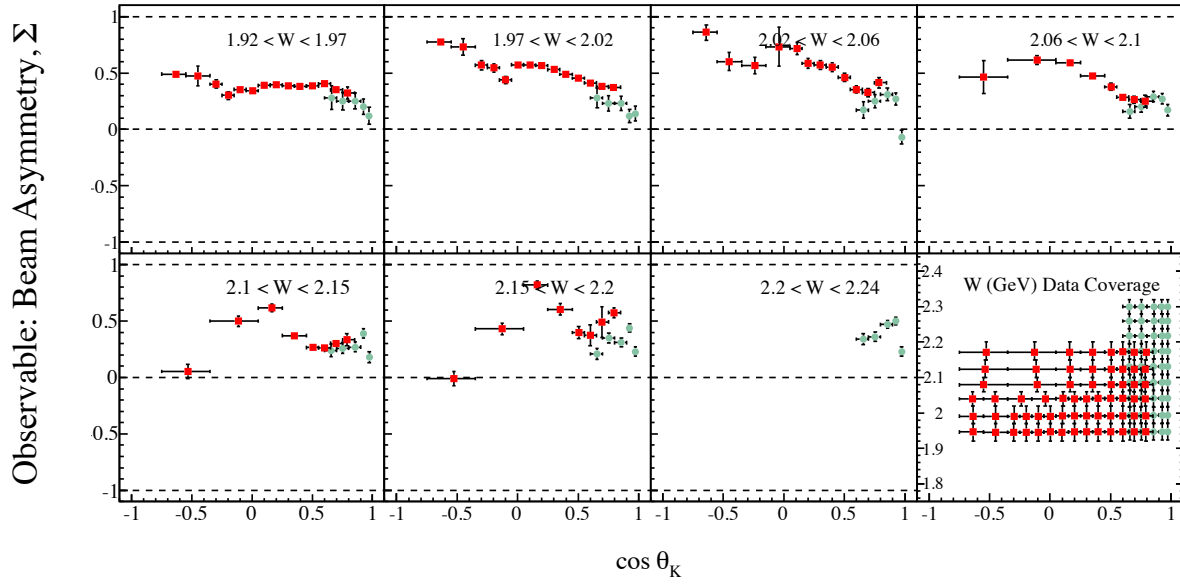
Figure 41. Comparison of beam asymmetry Σ between g8 (red squares) and LEPS (green circles).

g8-LEPS comparison: $\gamma + p \rightarrow K^{+}\Sigma^{0}$
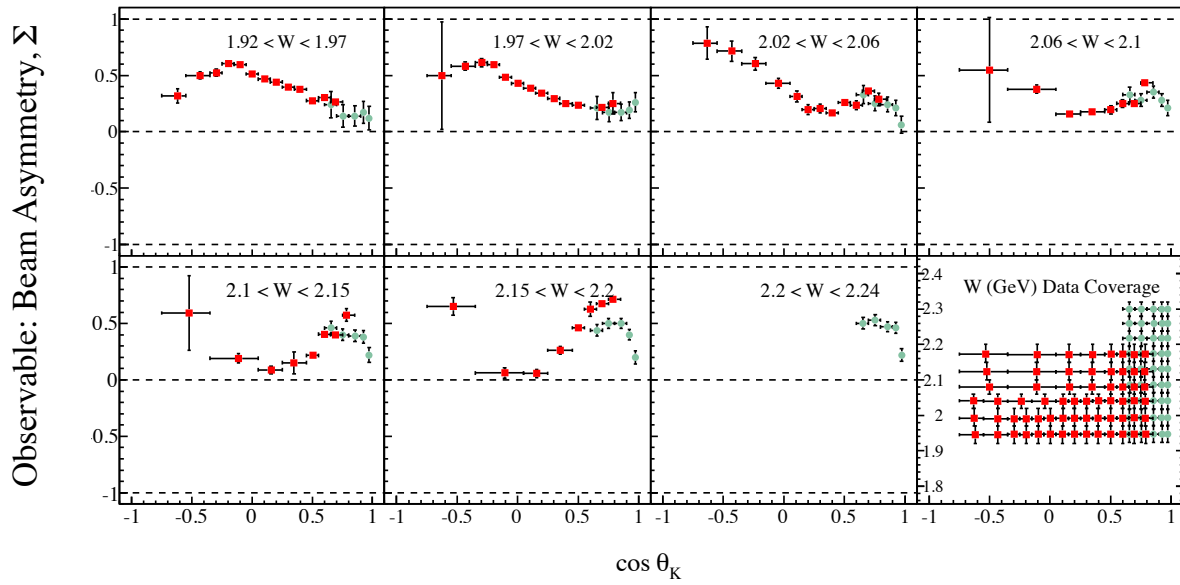
Figure 42. Comparison of beam asymmetry Σ between g8 (red squares) and LEPS (green circles).

845 ## C.   GRAAL measurements

846   GRAAL published measurements of beam asymmetry and recoil polarization for both
847 the $K\Lambda$ and $K\Sigma^0$ channels [19], and separately measurements of O_x, O_z and T for $K\Lambda$
848 [20]. These covered eleven photon beam energy bins, and six angles. To compare the
849 g8 results with these, bins were defined to be matched to GRAAL bins in W, but with a
850 larger number of angular bins where possible. The results of this comparison are shown
851 in figures 43-47. The plots show an excellent agreement between the two experiments for
852 all the observables in both channels. They also show the very much improved accuracy
853 of the g8 data.

g8-GRAAL comparison: $\gamma + p \rightarrow K^+ \Lambda$
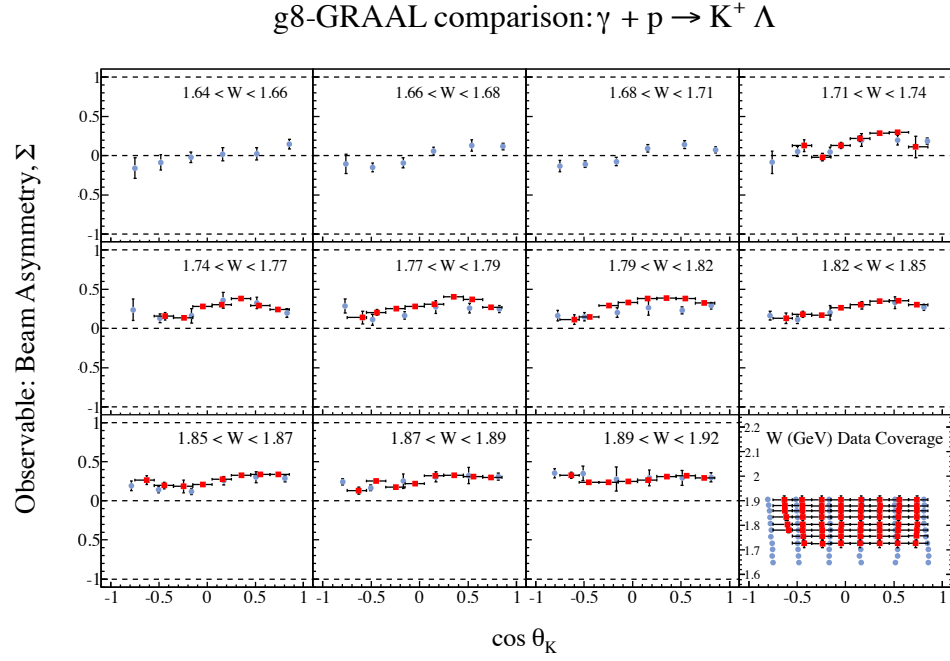
Figure 43. Comparison of beam asymmetry Σ between g8 (red squares) and GRAAL (blue circles).

g8-GRAAL comparison: $\gamma + p \rightarrow K^+ \Lambda$
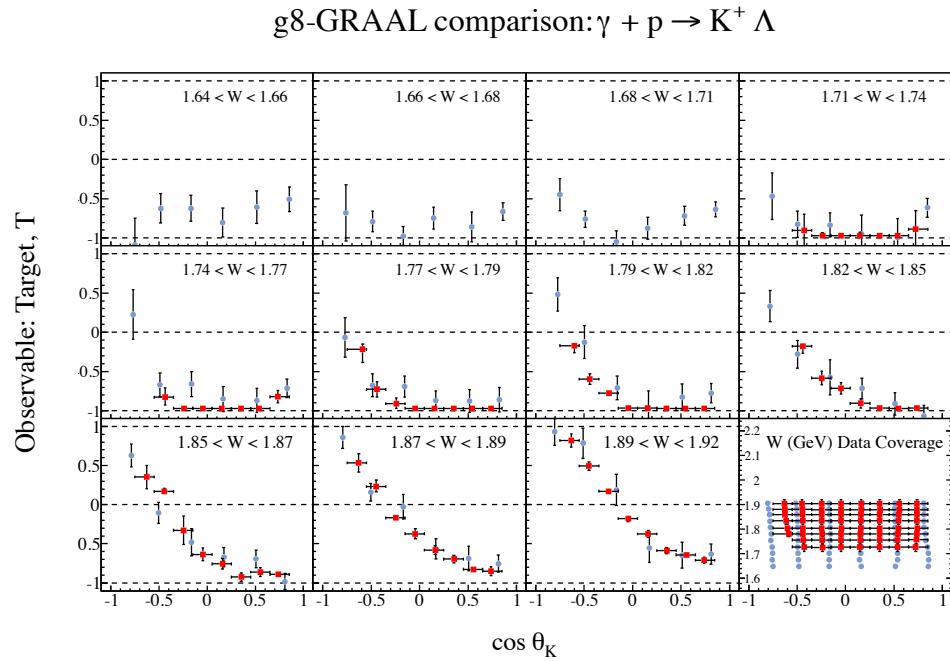
Figure 44. Comparison of target polarization T between g8 (red squares) and GRAAL (blue circles).

g8-GRAAL comparison: $\gamma + p \rightarrow K^+ \Lambda$
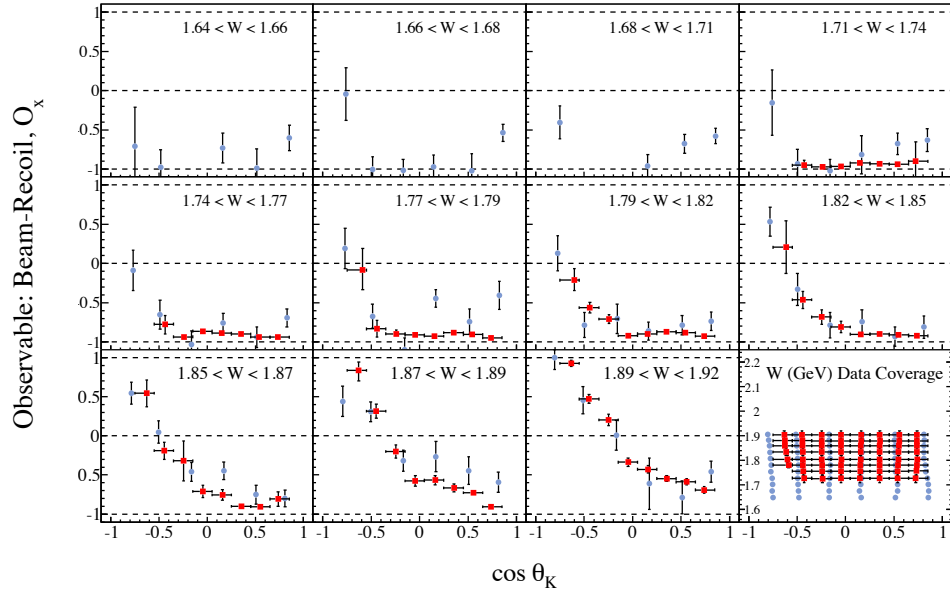
Figure 45.   Comparison of beam-recoil double polarization O_x between g8 (red squares) and GRAAL (blue circles).

g8-GRAAL comparison: $\gamma + p \rightarrow K^+ \Lambda$
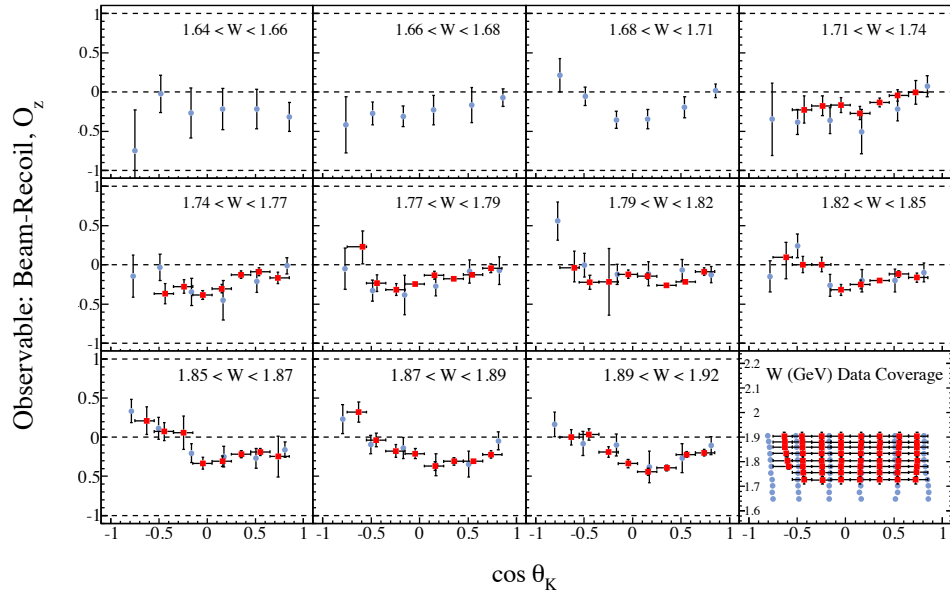
Figure 46.   Comparison of beam-recoil double polarization O_z between g8 (red squares) and GRAAL (blue circles).

g8-GRAAL comparison: $\gamma + p \rightarrow K^+ \Sigma^0$
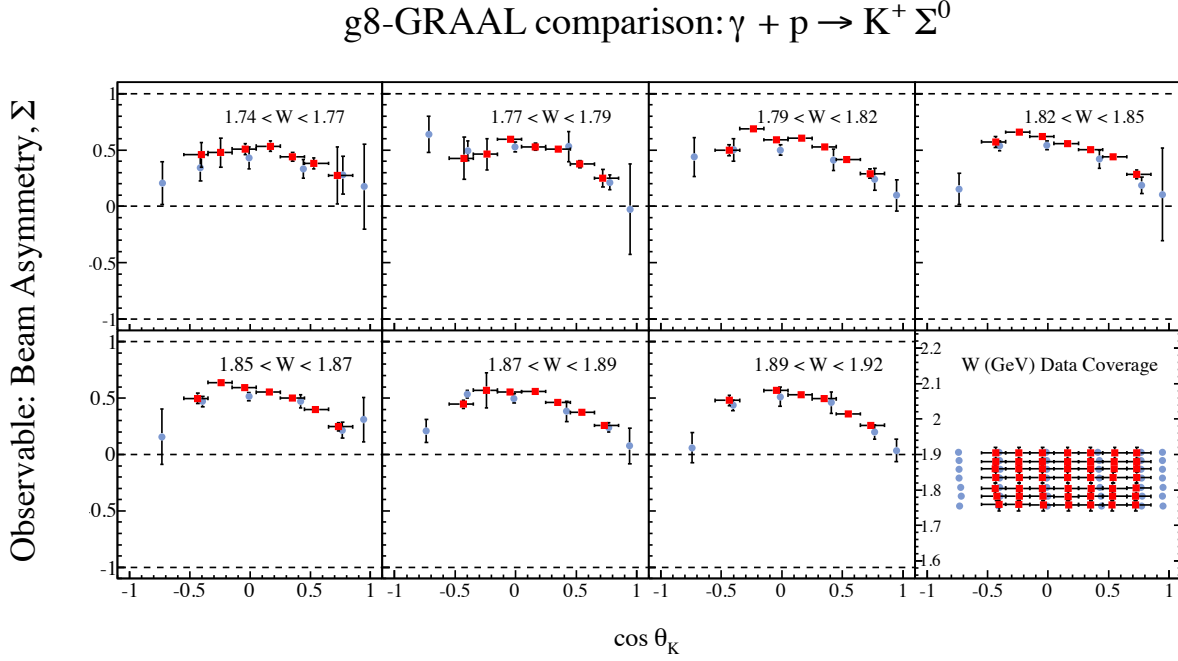
Figure 47. Comparison of beam asymmetry Σ between g8 (red squares) and GRAAL (blue circles).

D.   Check of a Fierz Identity

As a final comparison with previous measurements, we can make use of one of the many identities that connect the polarization observables for pseudoscalar meson photo-production. The g1c measurement of $K\Lambda$ and $K\Sigma^0$ channels extracted the observables C_x and C_z in a similar range of W and $\cos\theta$ to the g11 measurement [1]. There is the relation

$$O_x^2 + O_z^2 + C_x^2 + C_z^2 + \Sigma^2 - T^2 + P^2 = 1$$

which connects all the observables measured in g8 and g1c. A comprehensive list of all such relations can be found in the appendix of [21] (the relation above is S.br in that paper). The relations in [21] have the beam-recoil observables in the "primed" frame, but since this is a squared relation, it should also hold true in the unprimed frame. Regarding g1c and g8 as independent experiments, we can plot $C_x^2 + C_z^2$ from g1c together with the combination $1 - O_x^2 - O_z^2 - \Sigma^2 + T^2 - P^2$ from g8 (bearing in mind that the value of P used is essentially from the g11 measurements). The physical range in both cases is $[0, 1]$.

The results of the comparison are shown in figures 48 and 49. Whilst the error bars from the combinations are large, it can be seen that there is a good degree of agreement

868 between the two combinations. The g8 data are, by construction, within the physical
869 range, and indicate a significant feature at $W = 2\,\mathrm{GeV}$, which is also seen in the g1c data.

870 **E.   Conclusion from Comparisons**

871 Checks for consistency have been carried out for several different experiments across
872 different ranges in W and $\cos\theta$. The overall level of agreement is very good, with all the
873 comparisons showing that the results extracted from g8 are consistent with the results
874 previously published, within experimental uncertainties. This will be crucial when the
875 data is used for comparison with theoretical models.

$$g1c: C_x^2 + C_z^2; \ g8: 1-\Sigma^2+T^2-P^2-O_x^2-O_z^2$$
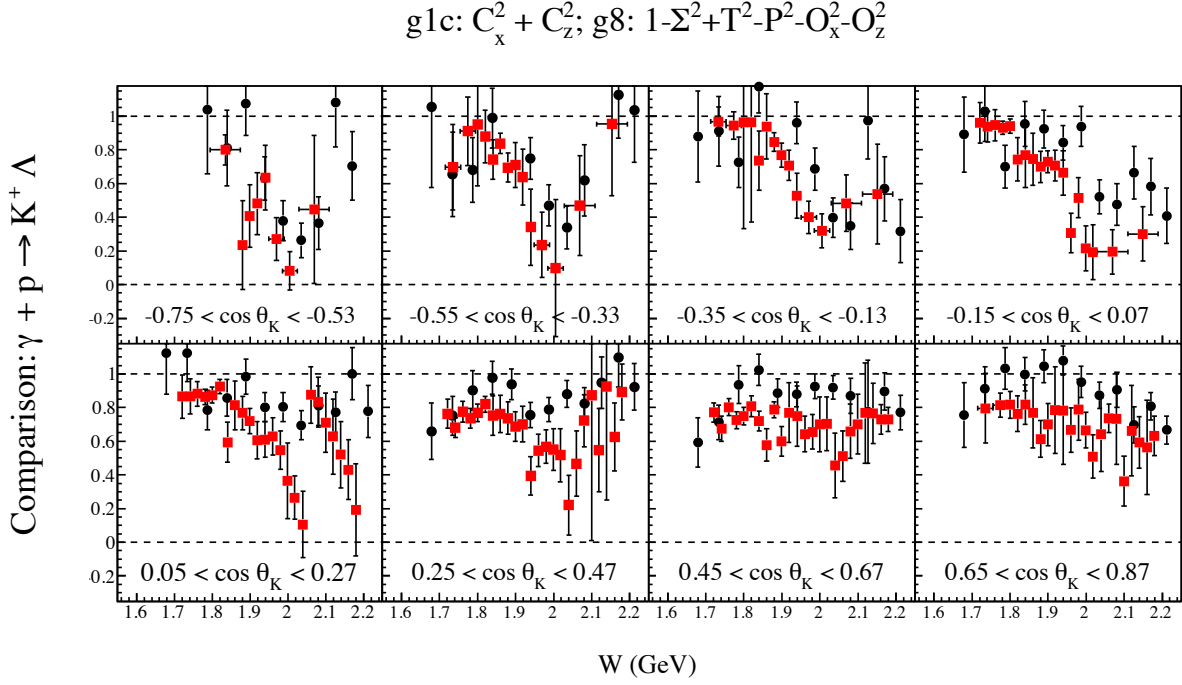
Figure 48. Fierz identity check for $K\Lambda$. Dark circles: g1c, $C_x^2 + C_z^2$; Red Squares: g8,$1 - O_x^2 - O_z^2 - \Sigma^2 + T^2 - P^2$

$$g1c: C_x^2 + C_z^2; \ g8: 1-\Sigma^2+T^2-P^2-O_x^2-O_z^2$$
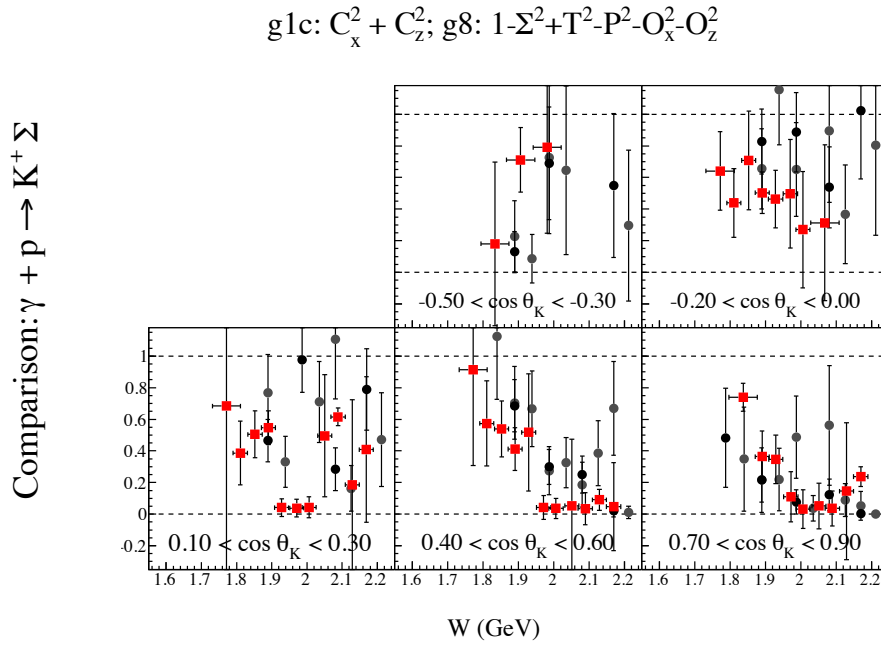
Figure 49. Fierz identity check for $K\Sigma^0$. Dark circles: g1c, $C_x^2 + C_z^2$; Red Squares: g8,$1 - O_x^2 - O_z^2 - \Sigma^2 + T^2 - P^2$

876 VI.   SYSTEMATICS AND OTHER CHECKS

877 Checks on the accuracy of the results boil down to two types: consistency checks, such
878 as those described in the previous section, and systematic checks based on studies of
879 quantities previously referred to as "nuisance paramters". Examination of the expres-
880 sions used to extract the observables show that the results are systematically dependent
881 on a few parameters, namely: photon polarization, goniometer offset, background esti-
882 mation. Each of these will be described later, but first some additional consistency checks
883 are highlighted.

884 A.   Comparing Results with χ^2 Extractions - Binned Fit check

885 The two techniques for extracting polarization observables were described previously
886 in sections IV B and IV D. At some level, the results obtained from them should be con-
887 sistent (bearing in mind the limitations of the binned technique). To do this correctly, we
888 need to extend the expression in eq. (9) to include an unpolarized background fraction
889 for larger bins in ξ for the binned fitting method

$$A\left(\xi\right) = \frac{\bar{P}_\gamma g}{\left(1+\beta\right)\left(f + \bar{P}_\gamma \Delta P_\gamma g\right)}. \tag{29}$$

890 The full expression for the asymmetry in counts now becomes

$$\Delta N = \frac{\Delta L + \frac{\bar{P}_\gamma g}{\left(1+\beta\right)\left(f + \bar{P}_\gamma \Delta P_\gamma g\right)}}{1 + \frac{\Delta L \bar{P}_\gamma g}{\left(1+\beta\right)\left(f + \bar{P}_\gamma \Delta P_\gamma g\right)}} = \frac{\bar{P}_\gamma \left(1 + \left(1+\beta\right)\Delta P_\gamma \Delta L\right) g + \left(1+\beta\right)\Delta L f}{\bar{P}_\gamma \left(\left(1+\beta\right)\Delta P_\gamma + \Delta L\right) g + \left(1+\beta\right) f}.$$

891 The data were analysed with the two different methods and two example compar-
892 isons, which display the greatest differences between the two methods are given in fig-
893 ures 50 and 51 for $K\Lambda$ and $K\Sigma^0$ respectively. These show

894 • generally good agreement between the methods;

895 • that the χ^2 method does not limit extracted values to the physical region;

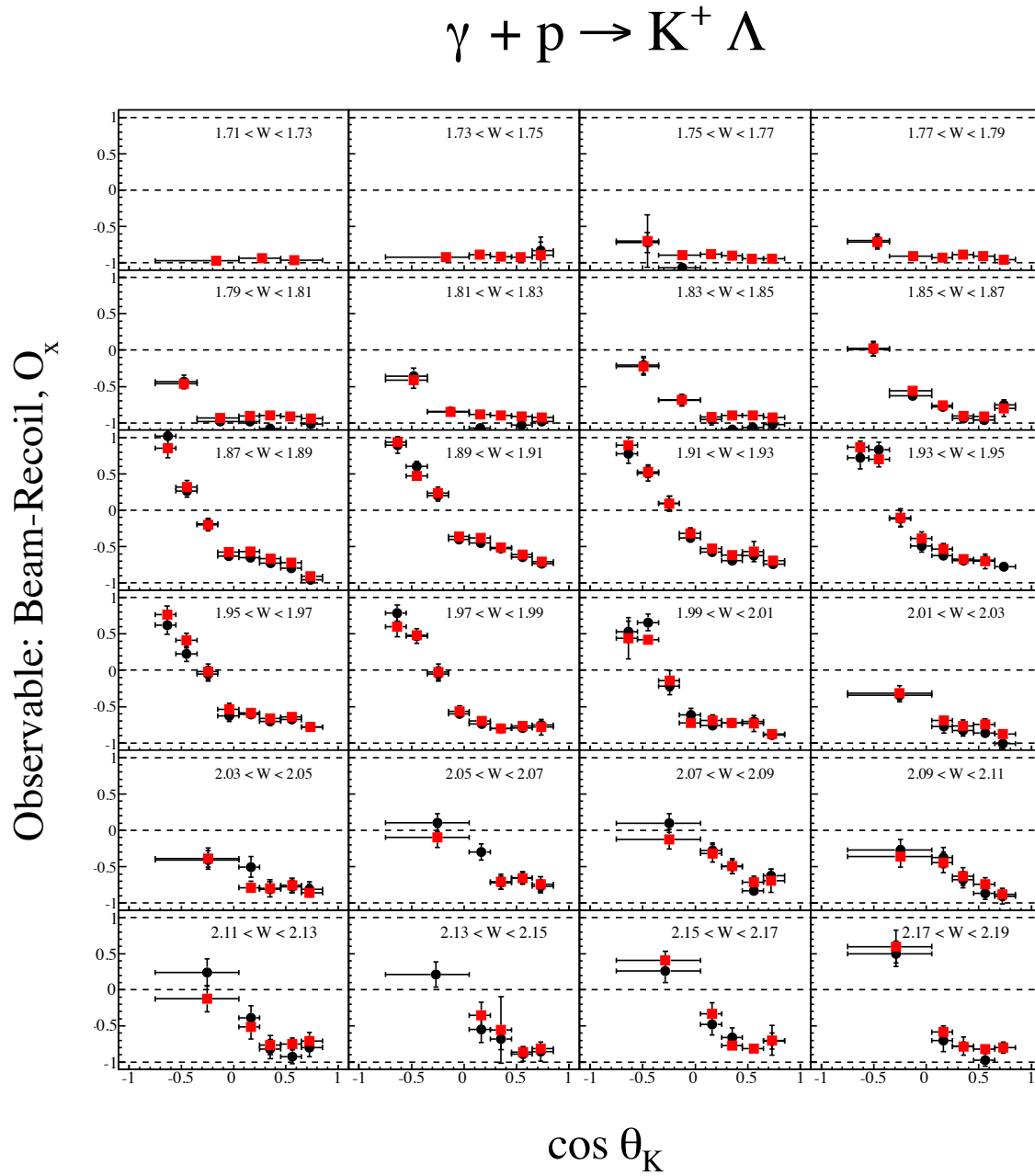896 • the unbinned method results in smoother angular distributions.

$$\gamma + p \rightarrow K^+ \Lambda$$

Figure 50. Example of comparison between χ^2 (black) and constrained ML (red) extracted values of O_x from $K\Lambda$.
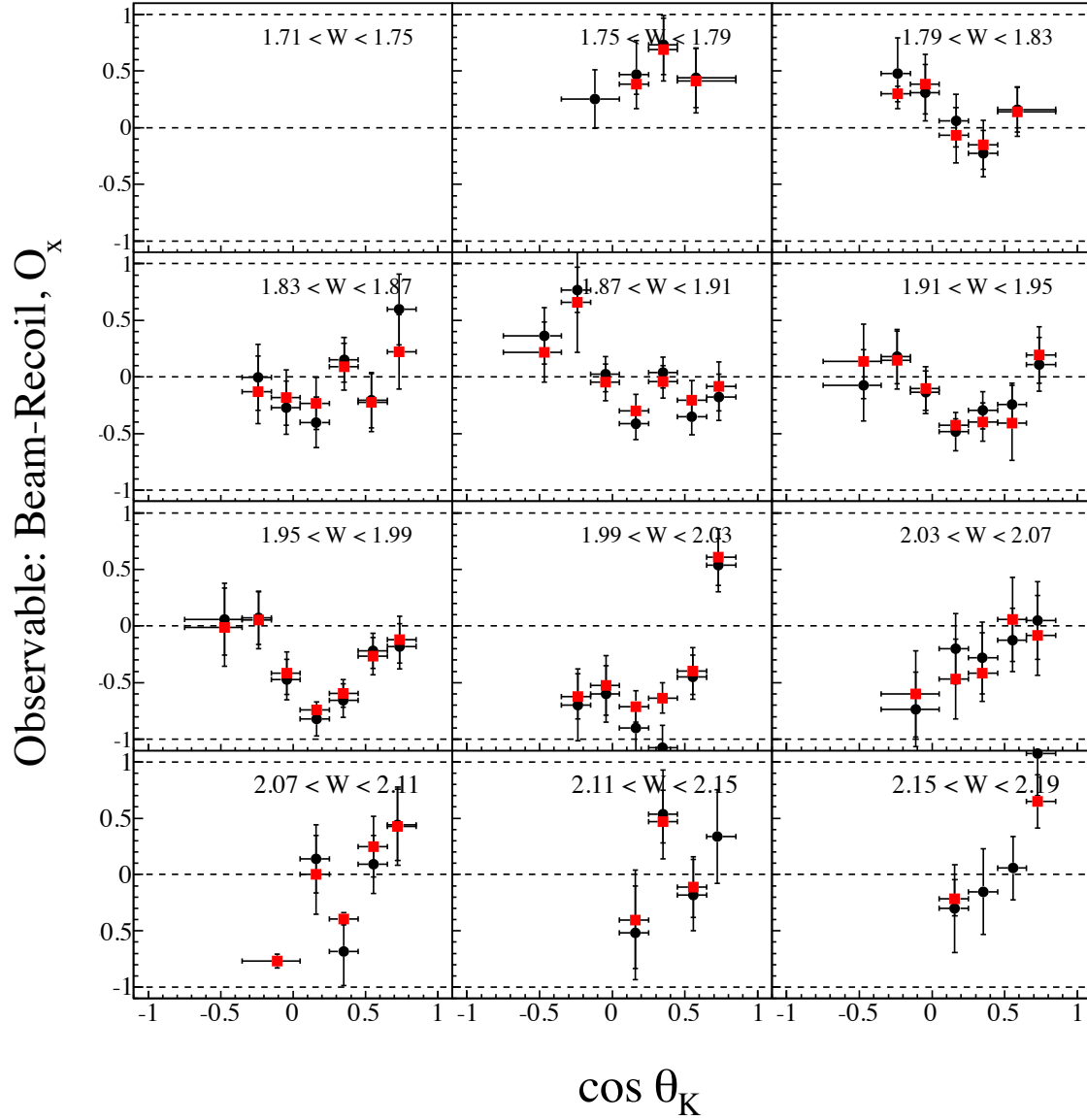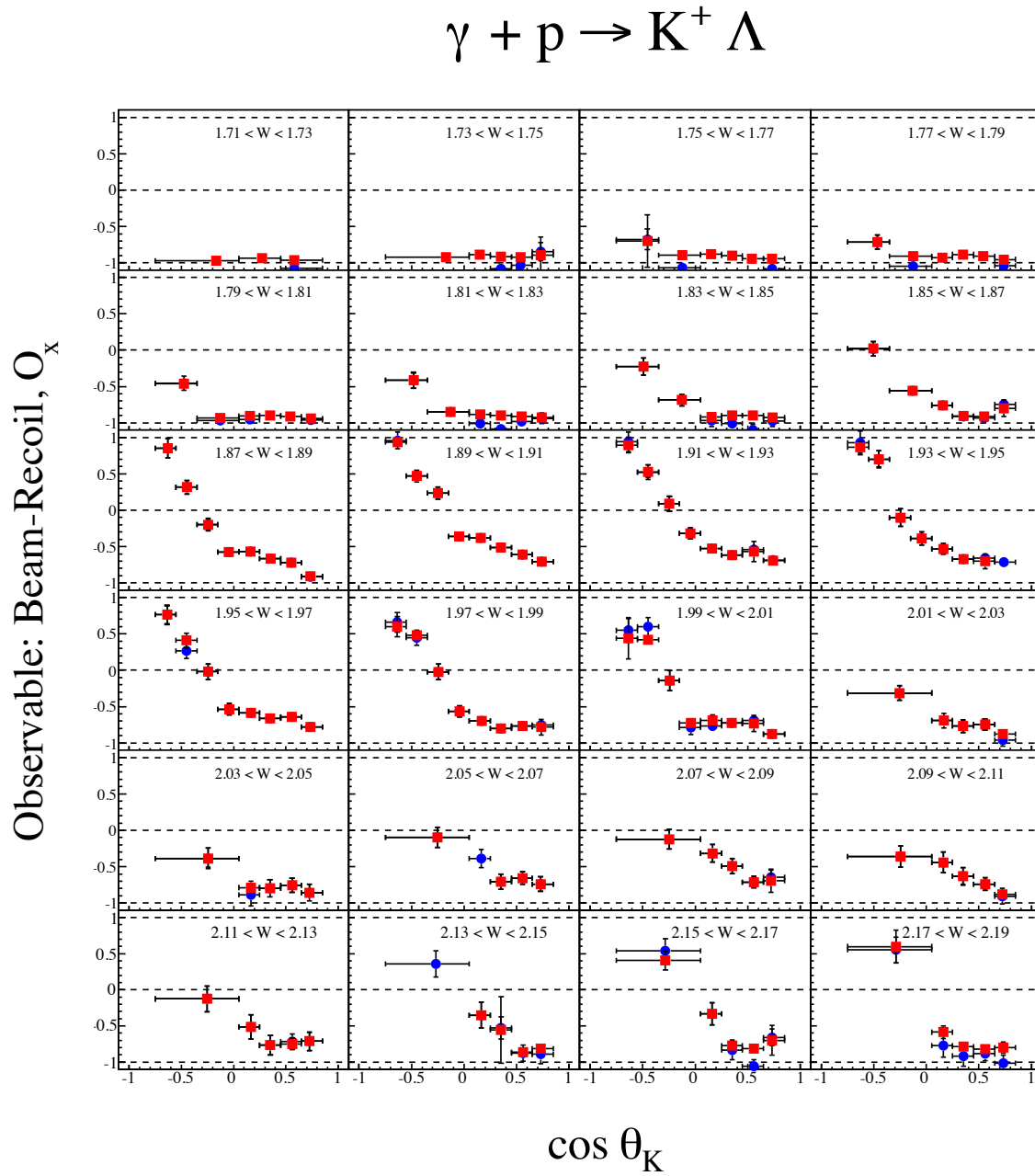
Figure 51. Example of comparison between χ^2 (black) and constrained ML (red) extracted values of O_x from $K\Lambda$.

B. Constrained vs. Unconstrained

To study the effect of constraining the observables to the physical region, the EPO program allows the option of an unconstrained maximum likelihood. A comparison of unconstrained versus constrained values indicates no significant difference in beam asymmetry values for both channels, and very little difference for the other observables. Figures 52 and 53 show the comparison of O_x for the $K\Lambda$ and $K\Sigma^0$ channels respectively. These examples respresent the greatest difference between the two methods. In both cases it is evident that the constraint has made a small difference when values approach the physical limit, and otherwise the results are consistent, since the overlap of points is enough to obscure the unconstrained results in most places.

Figure 52. Example of comparison between unconstrained ML (blue) and constrained ML (red) extracted values of O_x from $K\Lambda$.
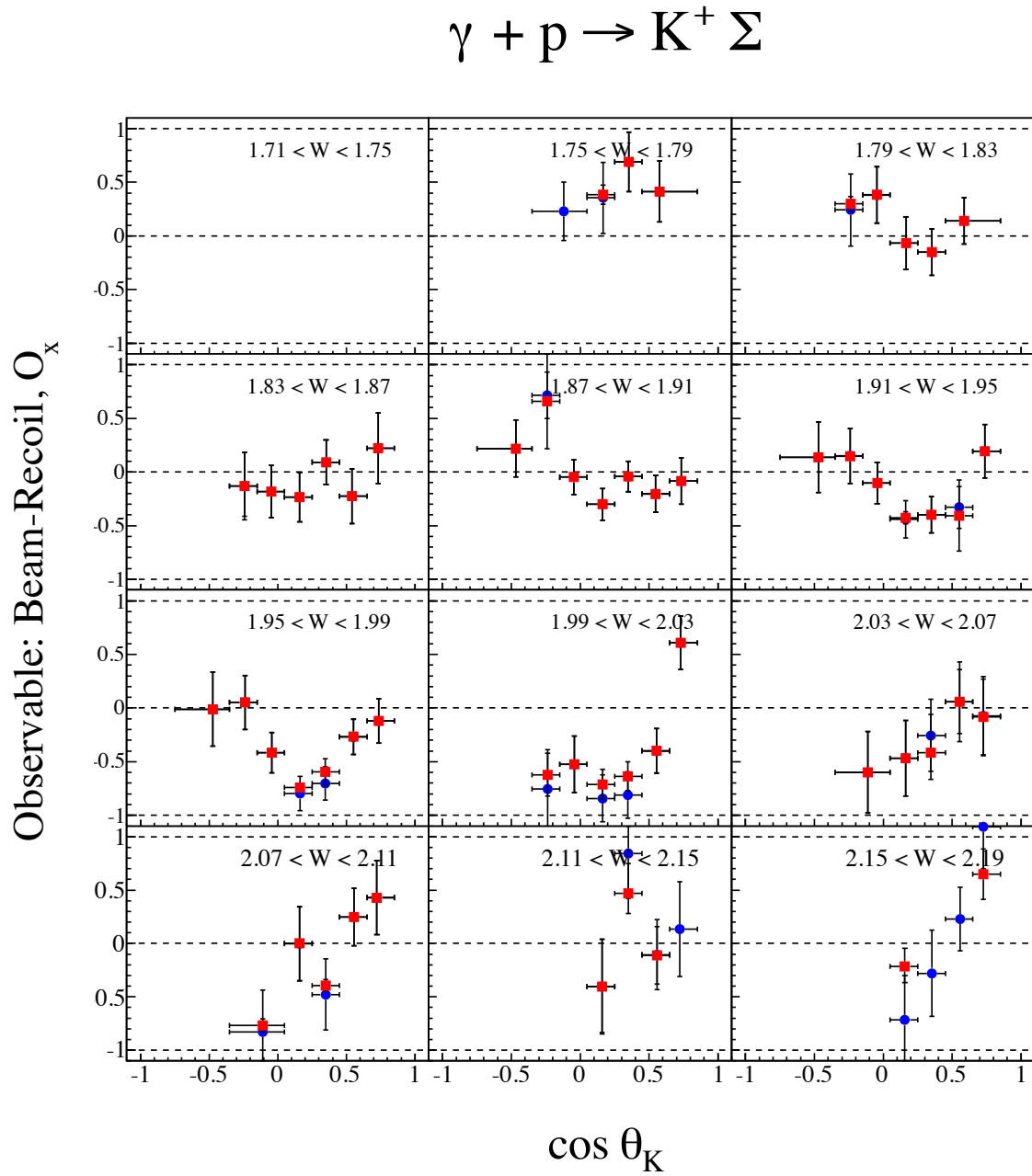
Figure 53. Example of comparison between unconstrained ML (blue) and constrained ML (red) extracted values of O_x from $K\Sigma^0$.

C.   Comparison between Different Topologies

A fraction of the g8 events contain three-particle measured final states, which we will refer to as 3-track events. Based on the number of 3-track events, bins were defined to enable a comparison between observables extracted from 2-track events and from 3-track events. These bins necessarily had to be rather larger than those possible for 2-track events. Comparisons have been made between the values of observables extracted from both 3-track and 2-track topologies in these bins, and this section displays the results.

This test accomplishes two things: internal consistency, and a check of the calculation of the effective weak decay constant in the case of the $K\Sigma^0$ channel. Both reactions studied here are identified from the detection of kaons and protons. In the case of the $K\Lambda$ reaction, this is enough to over-determine the kinematics, whereas with the additional photon from the decay of the Σ means that there are not suffcient measured kinematic variables to determine the rest frame of the Λ in the decay chain $\Sigma \to \Lambda\gamma; \Lambda \to \pi^- p$. The polarization of the Σ^0 is retained in part by the Λ, and one can show that the relationship between polarizations is

$$P_\Lambda = -\frac{1}{3}P_{\Sigma^0}. \tag{30}$$

So by determining the polarization components of the Λ, those of the Σ^0 can be obtained. However the equation (30) only applies if one can determine the Λ rest frame, and this is only possible for 3-track events. A detailed calculation of how to obtain the Σ^0 polarization components for 2-track events is given in the appendix of [1], and we use the results of that calculation here. The key results are that for 2-track events, the effective weak decay constant is

$$\alpha_{eff} = -0.256\alpha$$

and the equivalent for 3-track events is

$$\alpha_{eff} = -\frac{1}{3}\alpha.$$

So using these values, if the extraction from 2-track and 3-track events is correct, the beam-recoil observables should be consistent.

The results are shown in figures 54-61. It appears that results from 2-track and 3-track events are consistent. Any points that are not within error bars can be seen to have different bin centroids.
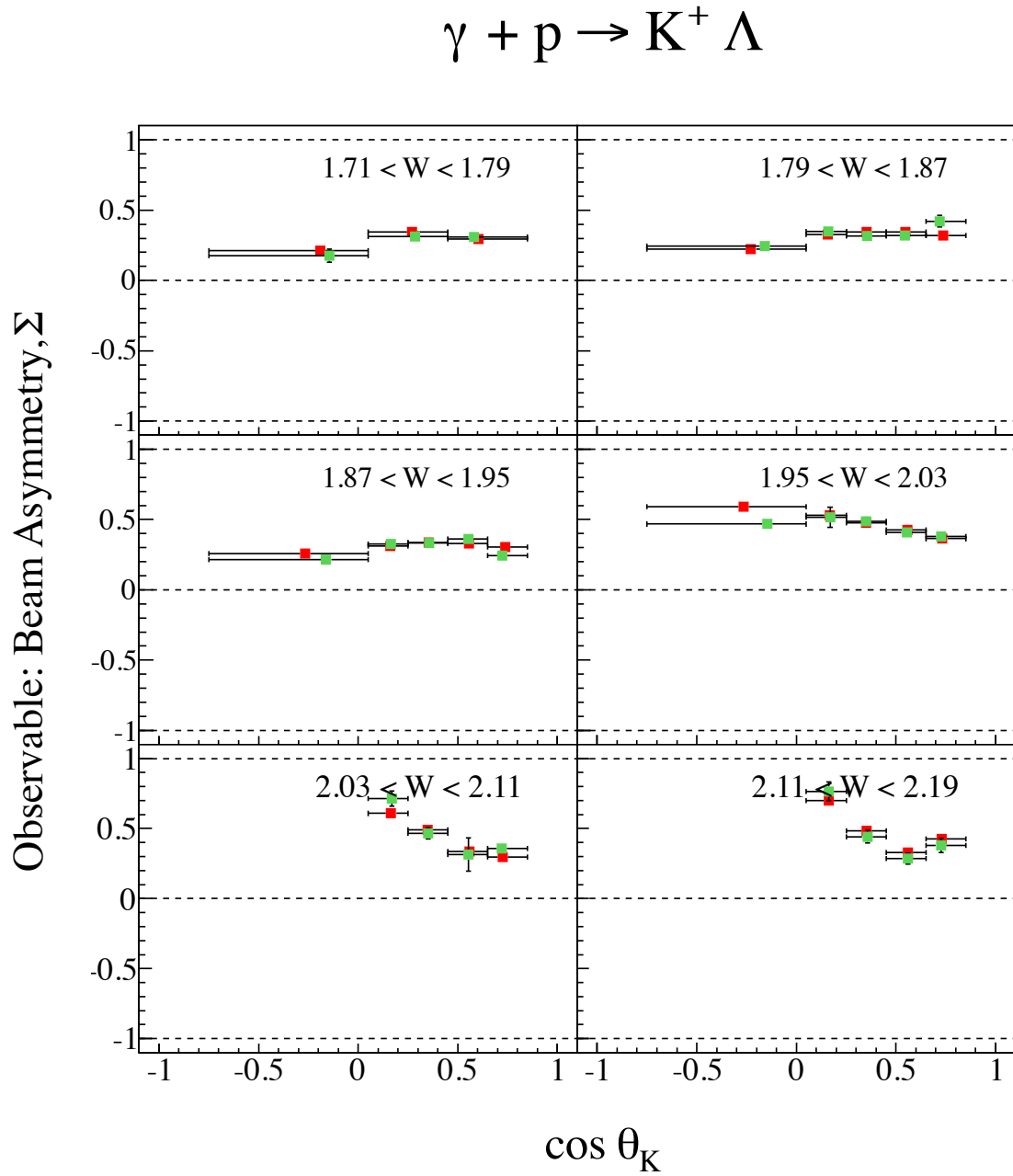
Figure 54. Comparison of $\gamma p \to K\Lambda$ beam asymmetries, extracted from 2-track (red) and 3-track (green) events.
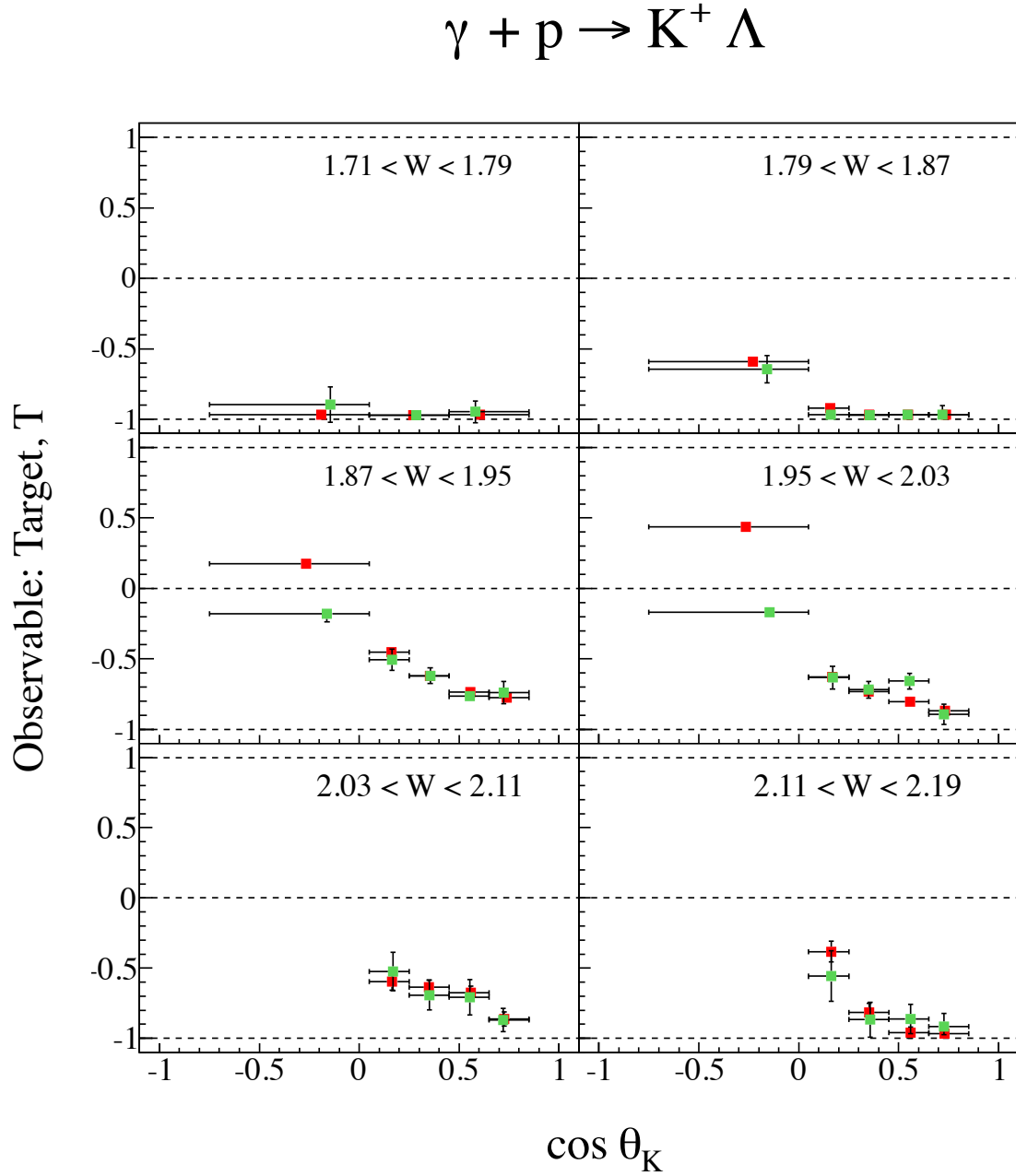
Figure 55. Comparison of $\gamma p \rightarrow K\Lambda$ target asymmetries, extracted from 2-track (red) and 3-track (green) events.
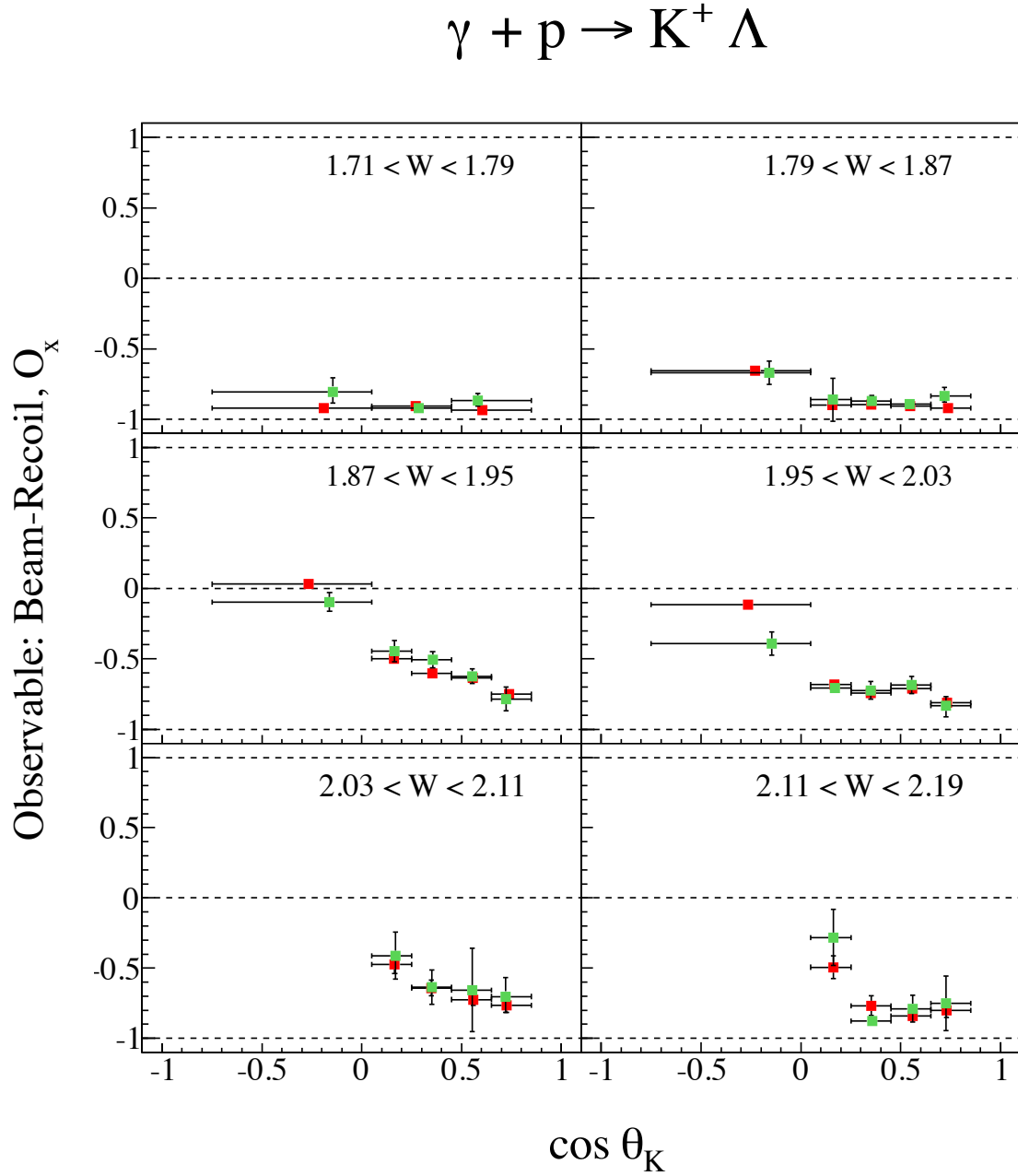
Figure 56. Comparison of $\gamma p \rightarrow K\Lambda$ beam-recoil O_x asymmetries, extracted from 2-track (red) and 3-track (green) events.
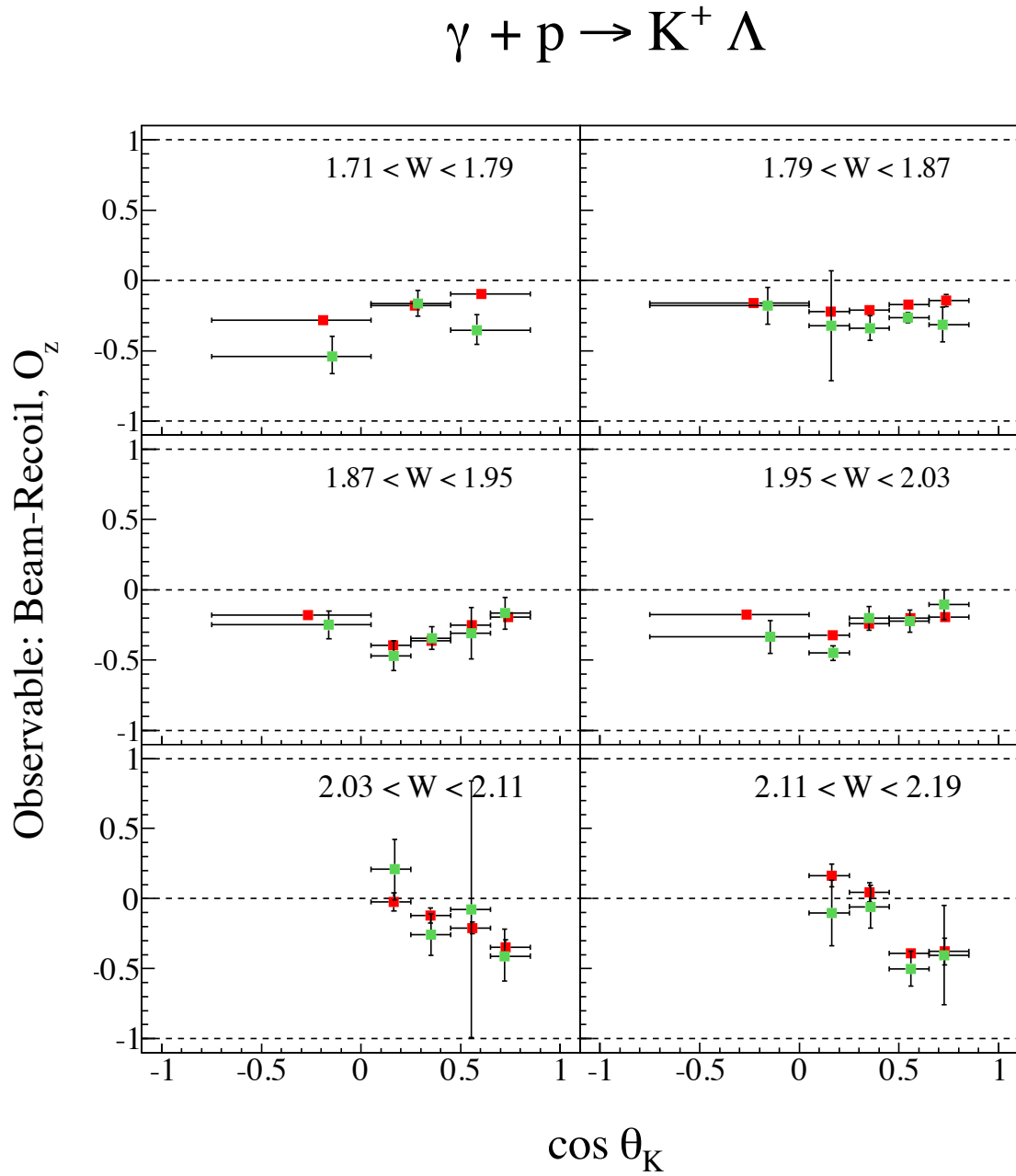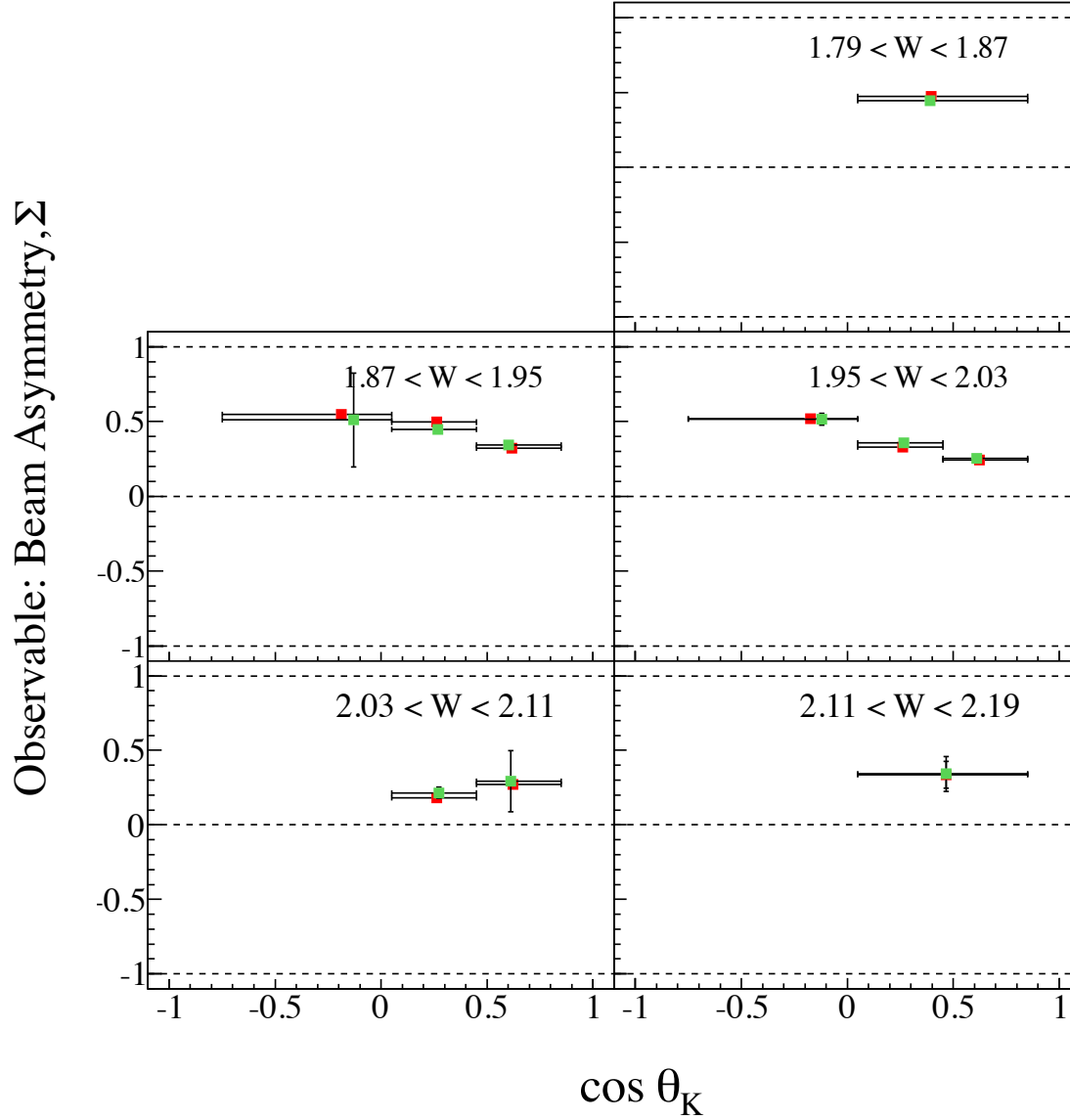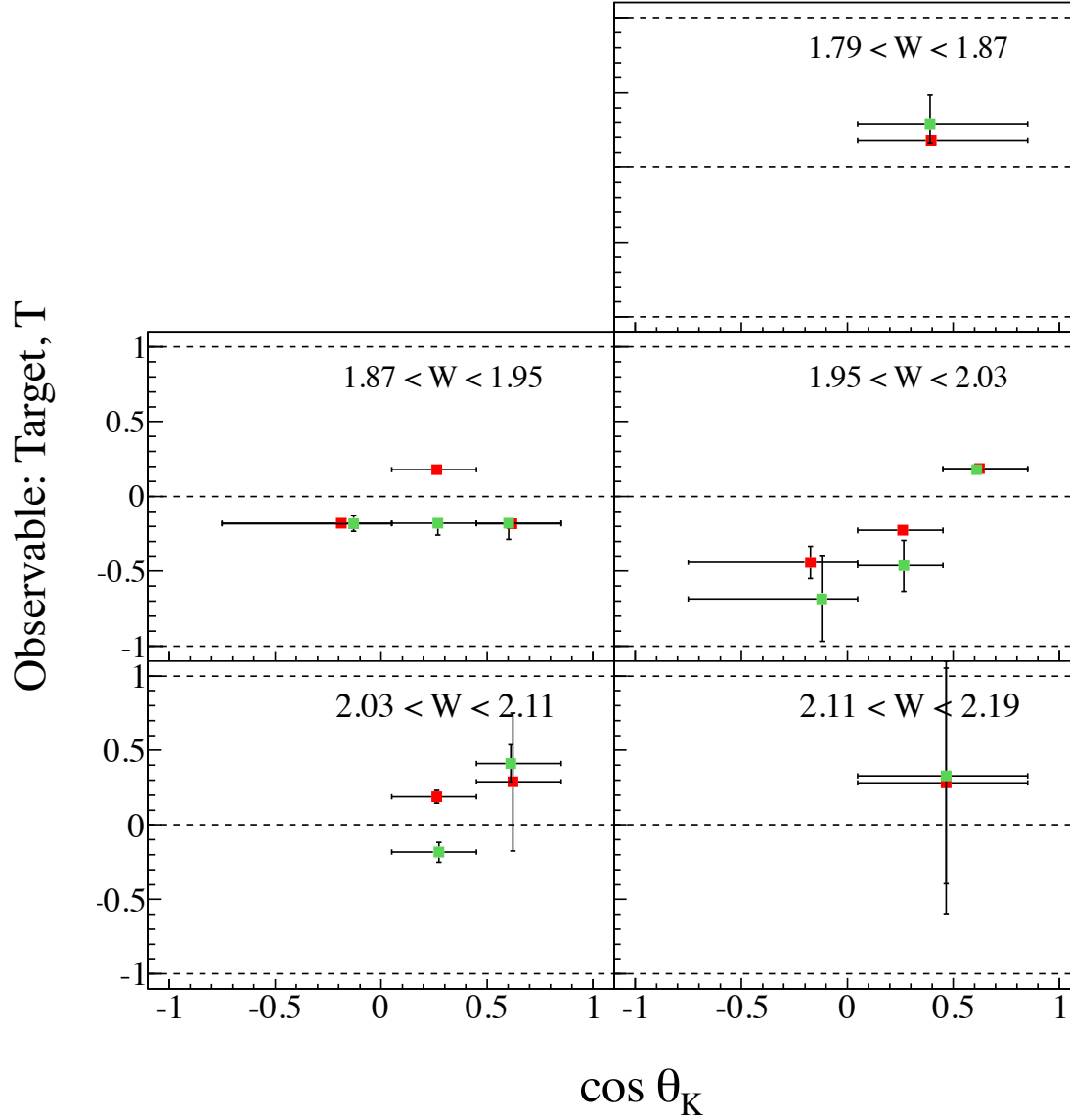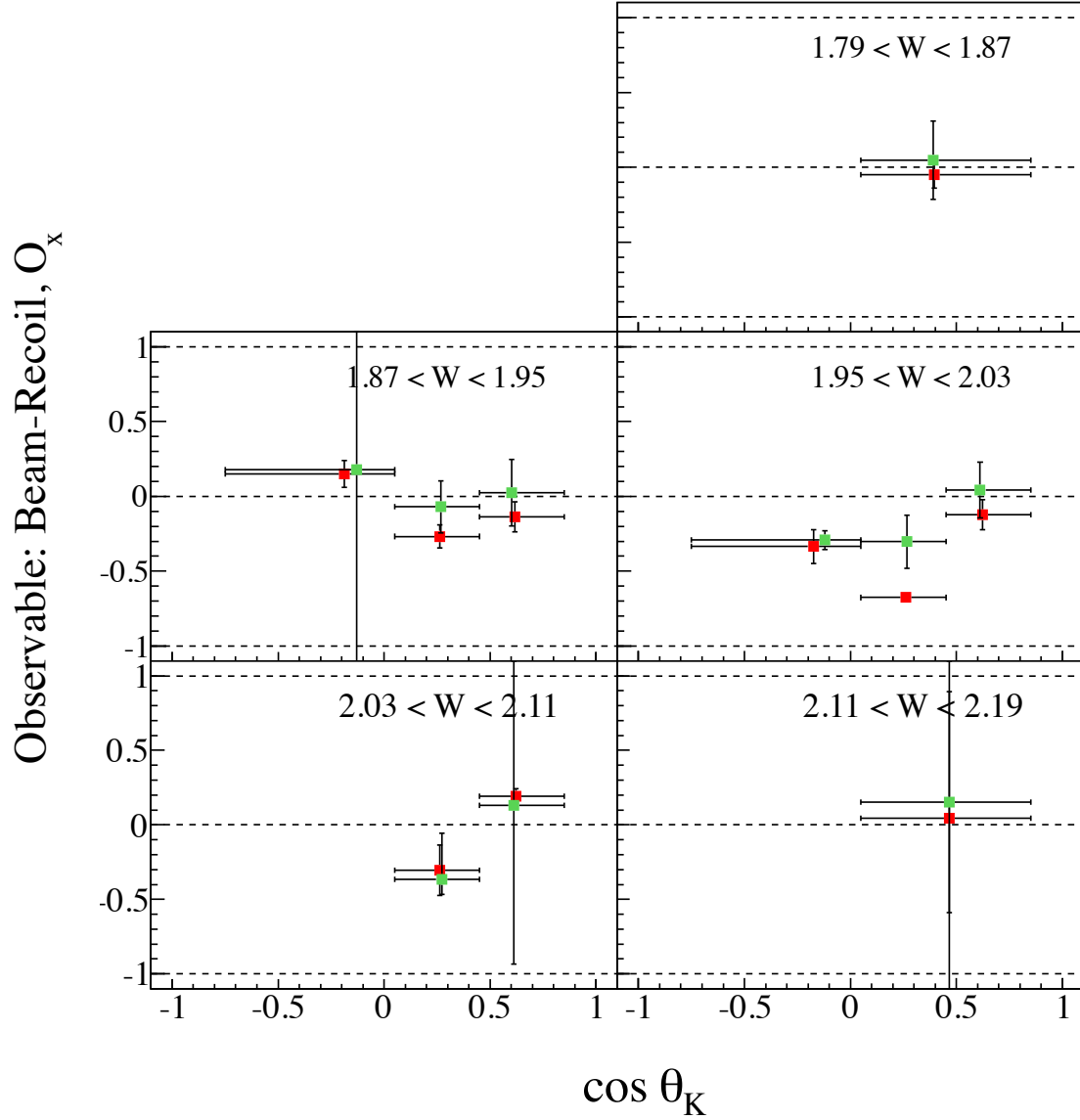
Figure 57. Comparison of $\gamma p \rightarrow K\Lambda$ beam-recoil O_z asymmetries, extracted from 2-track (red) and 3-track (green) events.

Figure 58. Comparison of $\gamma p \to K\Sigma^0$ beam asymmetries, extracted from 2-track (red) and 3-track (green) events.

Figure 59. Comparison of $\gamma p \rightarrow K\Sigma^0$ target asymmetries, extracted from 2-track (red) and 3-track (green) events.

Figure 60. Comparison of $\gamma p \rightarrow K\Sigma^0$ beam-recoil O_x asymmetries, extracted from 2-track (red) and 3-track (green) events.
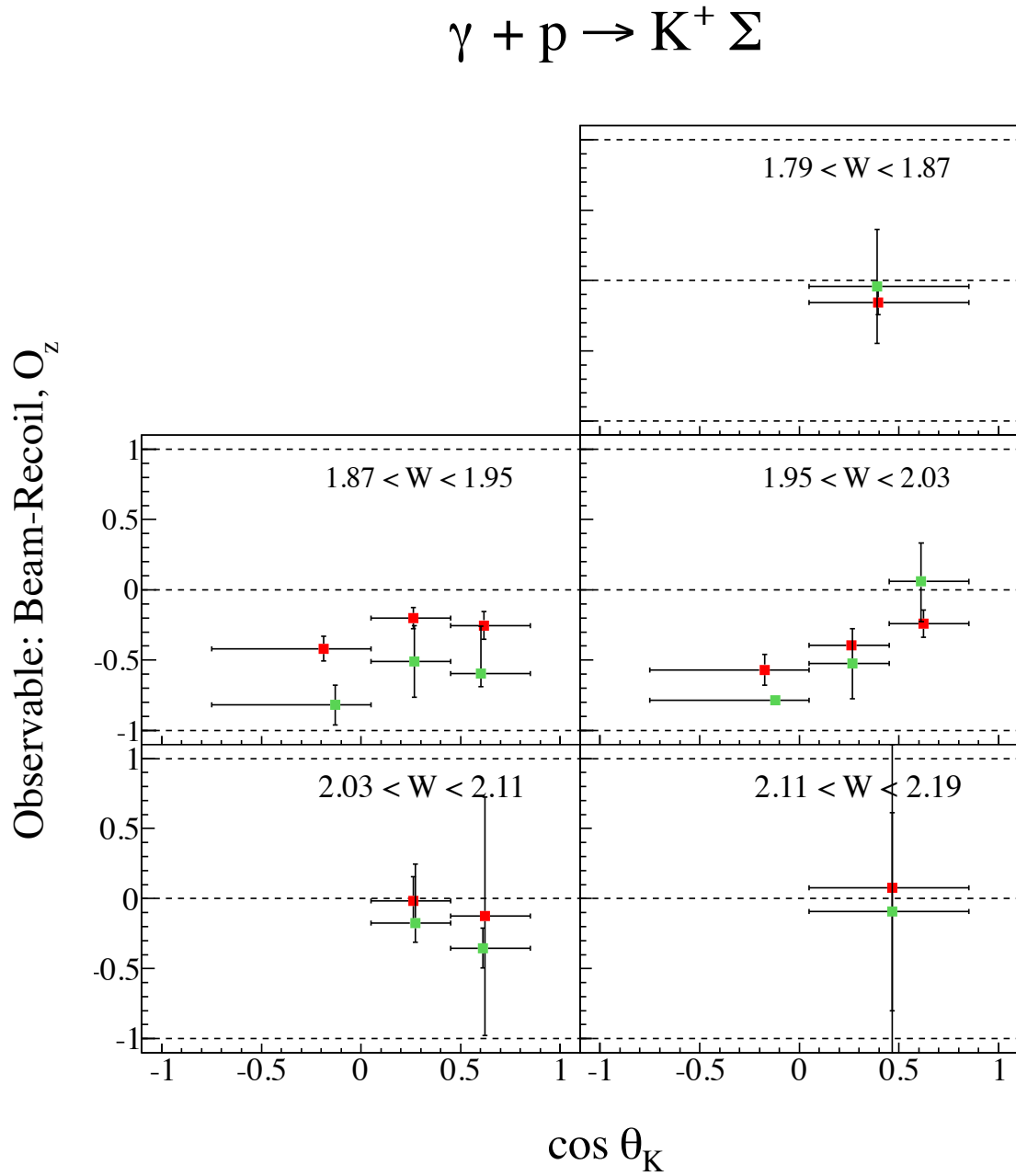
Figure 61. Comparison of $\gamma p \rightarrow K\Sigma^0$ beam-recoil O_z asymmetries, extracted from 2-track (red) and 3-track (green) events.

934   **D.   Photon polarization**

935   As mentioned previously, the determination of the degree of photon linear polariza-
936 tion is central to the g8 experiments. Previous studies of how accurately this can be
937 determined [10] showed that for g8, the data up to $E_\gamma = 2.1$ GeV ($W \approx 2.1$ GeV) had an
938 associated systematic uncertainty of 3% on the value of photon polarization, whilst data
939 above that energy had a 6% uncertainty. To estimate the effect of this on the extracted val-
940 ues of observables in $K\Lambda$ and $K\Sigma^0$, EPO was run with all values of photon polarization
941 adjusted by ± 0.03.

942   For each $\{W_i, \cos\theta_i\}$ bin a relative difference for each observable was calculated. For
943 an observable $\mathcal{O}_i$ in bin i, the relative difference between the best estimate $\mathcal{O}_i^{best}$ and the
944 estimate with the photon polarization systematically adjusted $\mathcal{O}_i^{sys}$ is defined as

$$\delta\mathcal{O}_i = 2\frac{\mathcal{O}_i^{sys} - \mathcal{O}_i^{best}}{\mathcal{O}_i^{sys} + \mathcal{O}_i^{best}}, \tag{31}$$

945 i.e. the difference divided by the average. This was used since the observables are all
946 asymmetries. There is some variation in relative differences for all observables across
947 the range in $\{W, \cos\theta\}$, so to summarize the effect of the systematic change in photon
948 polarization the median value of relative difference is obtained and quoted. We use the
949 median rather than the mean, since the occasional point may have a very large relative
950 difference caused by having small absolute values, which will have unrealistic pulls on
951 the mean. What we want is an estimate of the average effect over the range of $\{W, \cos\theta\}$
952 bins. The results for this study are given in table IV.

Observable	$K\Lambda$		$K\Sigma^0$	
	$P_\gamma + 0.03$	$P_\gamma - 0.03$	$P_\gamma + 0.03$	$P_\gamma - 0.03$
Σ	-0.036	0.037	-0.037	0.039
T	-0.037	0.037	-0.034	0.033
O_x	-0.035	0.035	-0.035	0.037
O_z	-0.035	0.035	-0.035	0.036

Table IV. Effect of uncertainty in P_γ. Average differences (and their standard deviations) between observables extracted with adjusted values of P_γ and the baseline values.

953 For values of Σ, the observed differences are what would be expected, i.e. a value of
954 P_γ that is 0.03 too low leads to a value of Σ that is too high, and vice versa. A further
955 check with $P_\gamma \pm 0.06$ was carried out for points above W=2.1 GeV, and it was established
956 that the size of the differences all scaled by a factor of 2.

957 **E. Goniometer Offset**

958 The angular positioning of the goniometer is known to be accurate. However, to study
959 what effect an error in the angle would have, we took large differences of $\pm 1°$ as offsets
960 and re-calculated the values of observables. As in the previous section, averages and
961 standard deviations over all $\{W, \cos\theta\}$ bins were evaluated, and the results are shown in
962 table V.

Observable	$K\Lambda$		$K\Sigma^0$	
	$\phi + 1°$	$\phi - 1°$	$\phi + 1°$	$\phi - 1°$
Σ	0.003	-0.004	-0.002	0.001
T	-0.001	0.000	-0.001	0.000
O_x	-0.006	0.005	0.024	-0.018
O_z	0.010	-0.012	-0.016	0.019

Table V. Effect of uncertainty in goniometer angular offset. Average differences (and their standard deviations) between observables extracted with adjusted values of Φ_0 and the baseline values.

963 We know that the goniometer offset in this study is exaggerated, and that it is likely to
964 be only at the level of $0.1°$. Given the small numbers in table V, we take the systematic
965 uncertainty associated with goniometer offset as being negligible.

966 **F. Background**

967 The amount of background has been estimated by fitting a function to the kaon miss-
968 ing mass spectrum at different points in the $\{W, \cos\theta\}$ range of this experiment (see sec-
969 tion IV C). This is seen to vary between 2-11%. To establish what effect an incorrect eval-
970 uation of this fraction would have, observables were extracted assuming no background,

Observable	$K\Lambda$	$K\Sigma^0$
Σ	-0.023	-0.025
T	-0.022	-0.015
O_x	-0.019	-0.024
O_z	-0.019	-0.024

Table VI. Effect of background uncertainty. Average differences (and their standard deviations) between observables extracted with no background and the baseline values.

and compared to the baseline values extracted by including the fitted background fraction. The results are shown in table VI.

The differences seen are relatively small, and represent a large overestimate, since the error in the fitted background fraction is about 1%. We therefore take the systematic error associated with uncertainty in background estimate as negligible.

G.   Summary

Having identified the possible major sources of systematic uncertainty, we conclude that the only source of systematic error that is significant for our results is the photon polarization estimate. The magnitude of this effect for different ranges of W is given in table VII. The final results presented in section VII show error bars that are statistical only.

Observable	$K\Lambda$		$K\Sigma^0$	
	$W < 2.1$ GeV	$W > 2.1$ GeV	$W < 2.1$ GeV	$W > 2.1$ GeV
Σ	0.037	0.073	0.038	0.076
T	0.037	0.074	0.034	0.067
O_x	0.035	0.070	0.036	0.072
O_z	0.035	0.070	0.036	0.071

Table VII. Estimates of total systematic errors on each observable for both channels.

VII.   PRESENTATION OF G8 DATA

In this section the extracted observables are presented in a manner that provides a reasonable visual impact. In order to present both angular disributions and energy distributions, a slightly different binning was required for each, as indicated in figures 32 and 33. For future comparisons with theoretical calculations, the definition of $\{W, \cos\theta\}$ bins can be altered very easily with the likelihood extraction (EPO) method, depending on the expected size of features either in angle or energy.
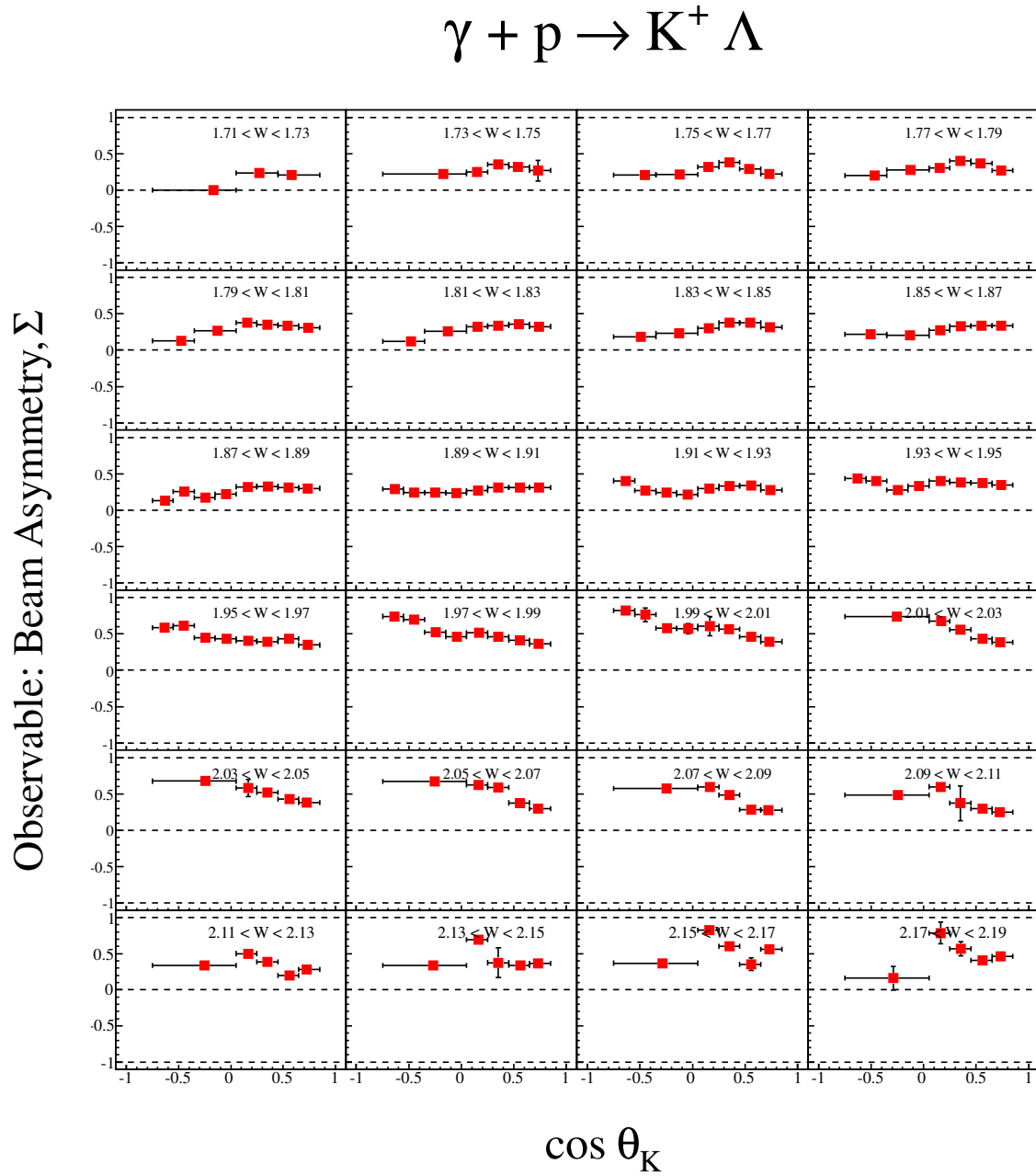
Figure 62. $\gamma p \to K^+\Lambda$ angular distributions of beam asymmetry Σ, for bins in W as labelled in each sub-plot.
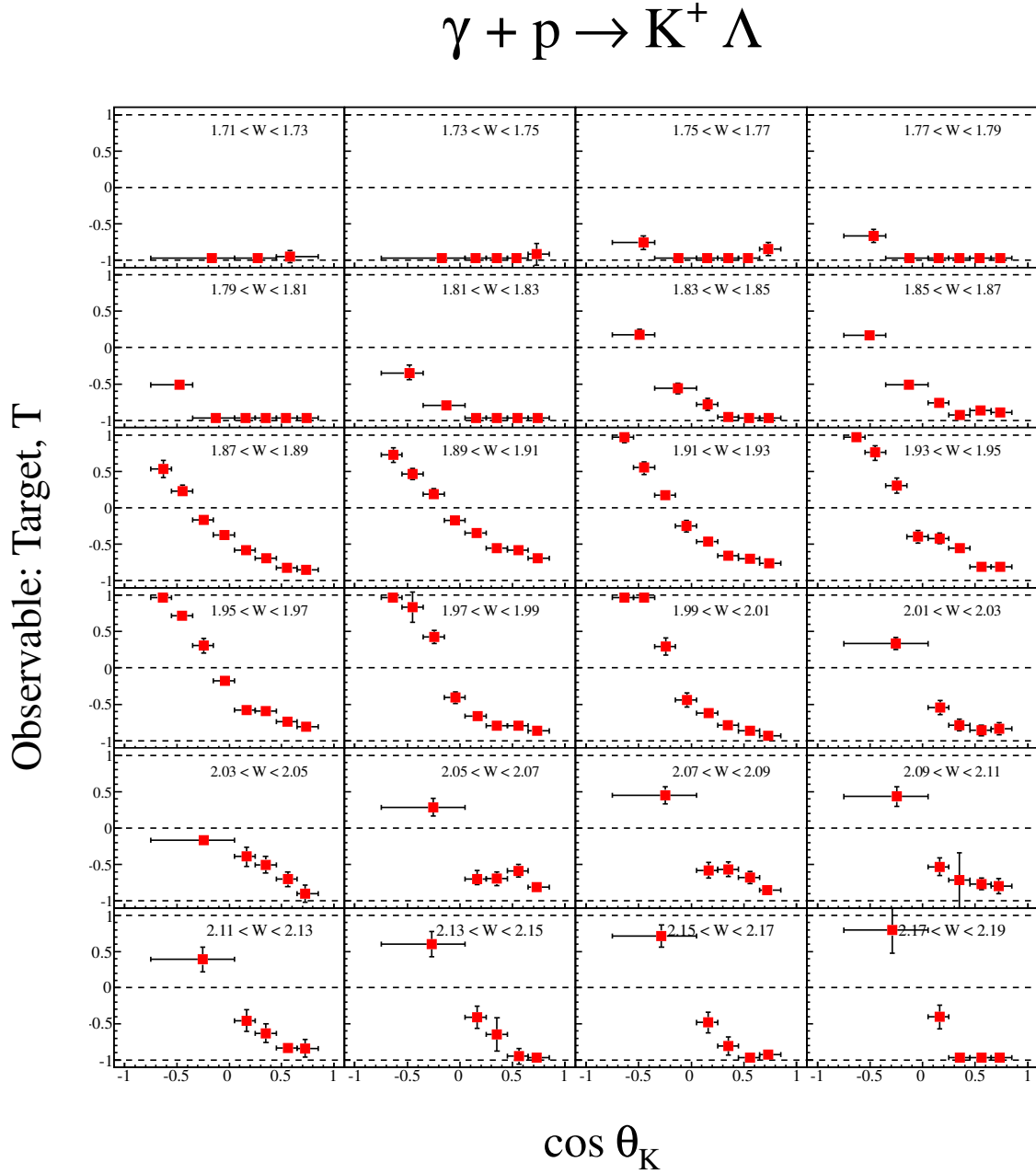
Figure 63. $\gamma p \to K^+ \Lambda$ angular distributions of target asymmetry T, for bins in W as labelled in each sub-plot.
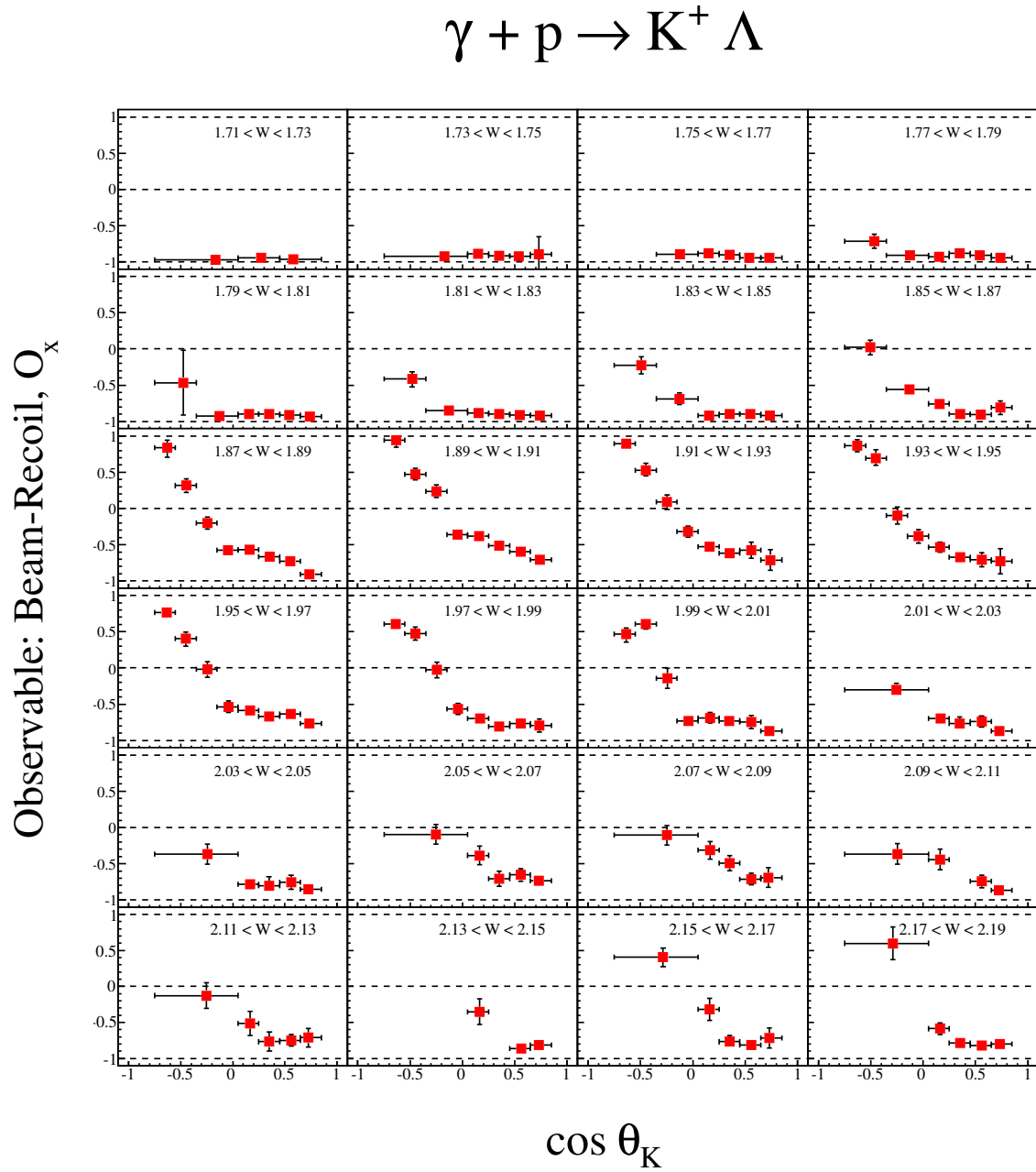
Figure 64. $\gamma p \rightarrow K^+\Lambda$ angular distributions of beam-recoil asymmetry O_x, for bins in W as labelled in each sub-plot.
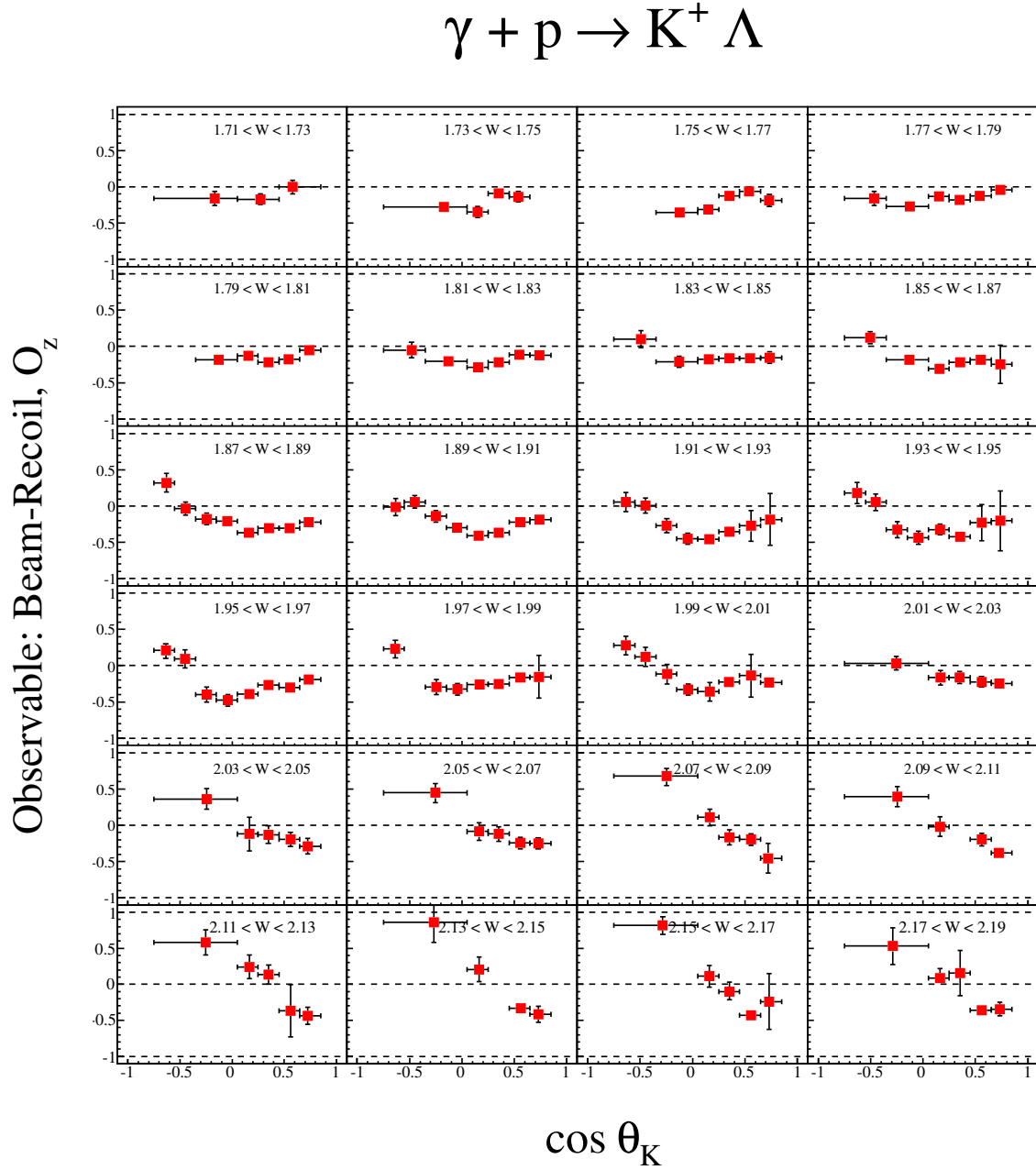
Figure 65. $\gamma p \rightarrow K^+\Lambda$ angular distributions of beam-recoil asymmetry O_z, for bins in W as labelled in each sub-plot.
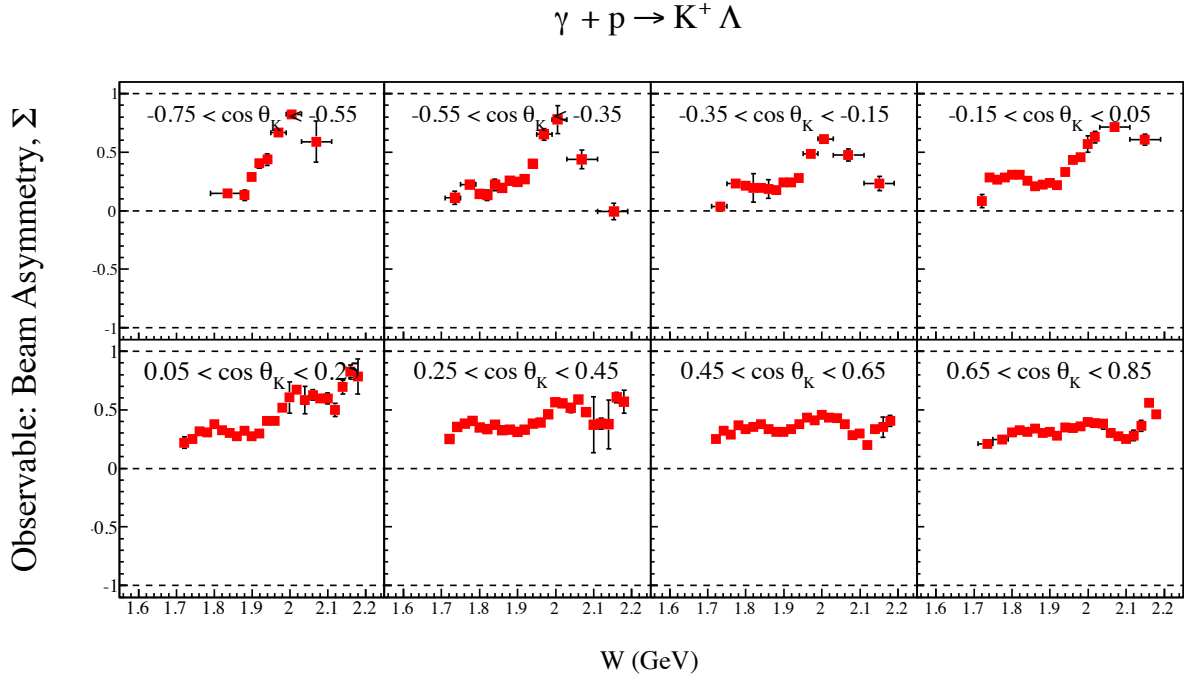
Figure 66. $\gamma p \to K^+ \Lambda$ hadronic mass W distributions of beam asymmetry Σ, for bins in $\cos \theta_K$ as labelled in each sub-plot.
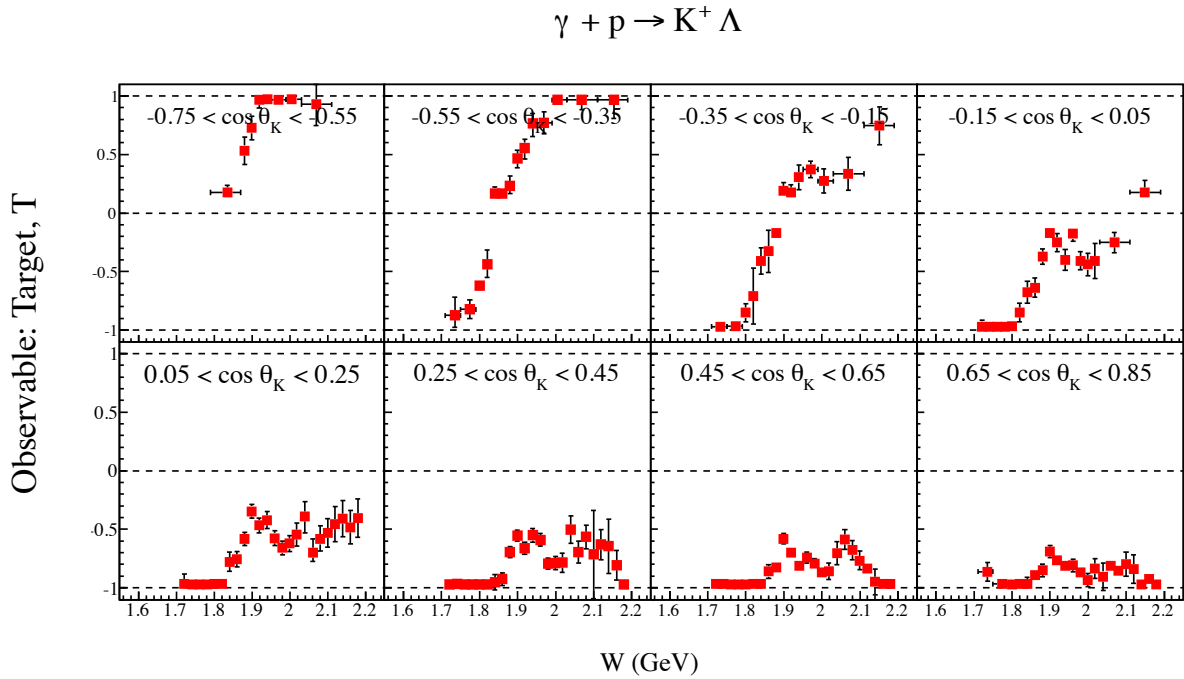

Figure 67. $\gamma p \to K^+ \Lambda$ hadronic mass W distributions of target asymmetry T, for bins in $\cos \theta_K$ as labelled in each sub-plot.

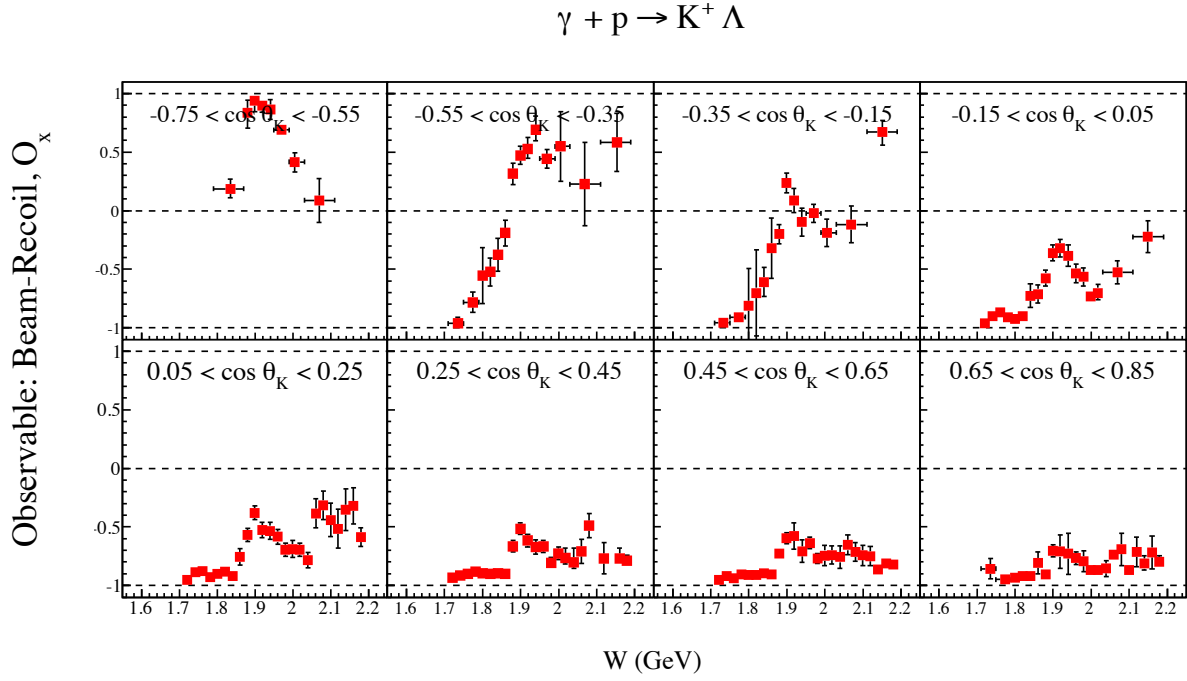$$\gamma + p \rightarrow K^+ \Lambda$$

Figure 68. $\gamma p \rightarrow K^+ \Lambda$ hadronic mass W distributions of beam-recoil asymmetry O_x, for bins in $\cos \theta_K$ as labelled in each sub-plot.
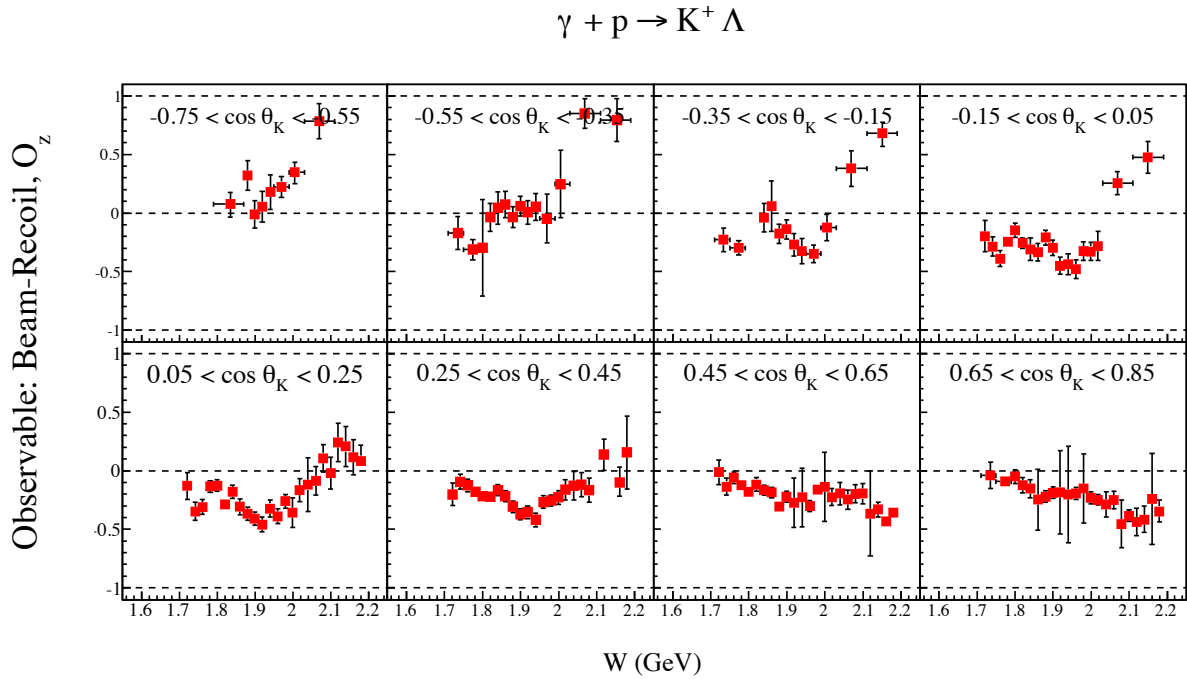
$$\gamma + p \rightarrow K^+ \Lambda$$

Figure 69. $\gamma p \rightarrow K^+ \Lambda$ hadronic mass W distributions of beam-recoil asymmetry O_z, for bins in $\cos \theta_K$ as labelled in each sub-plot.
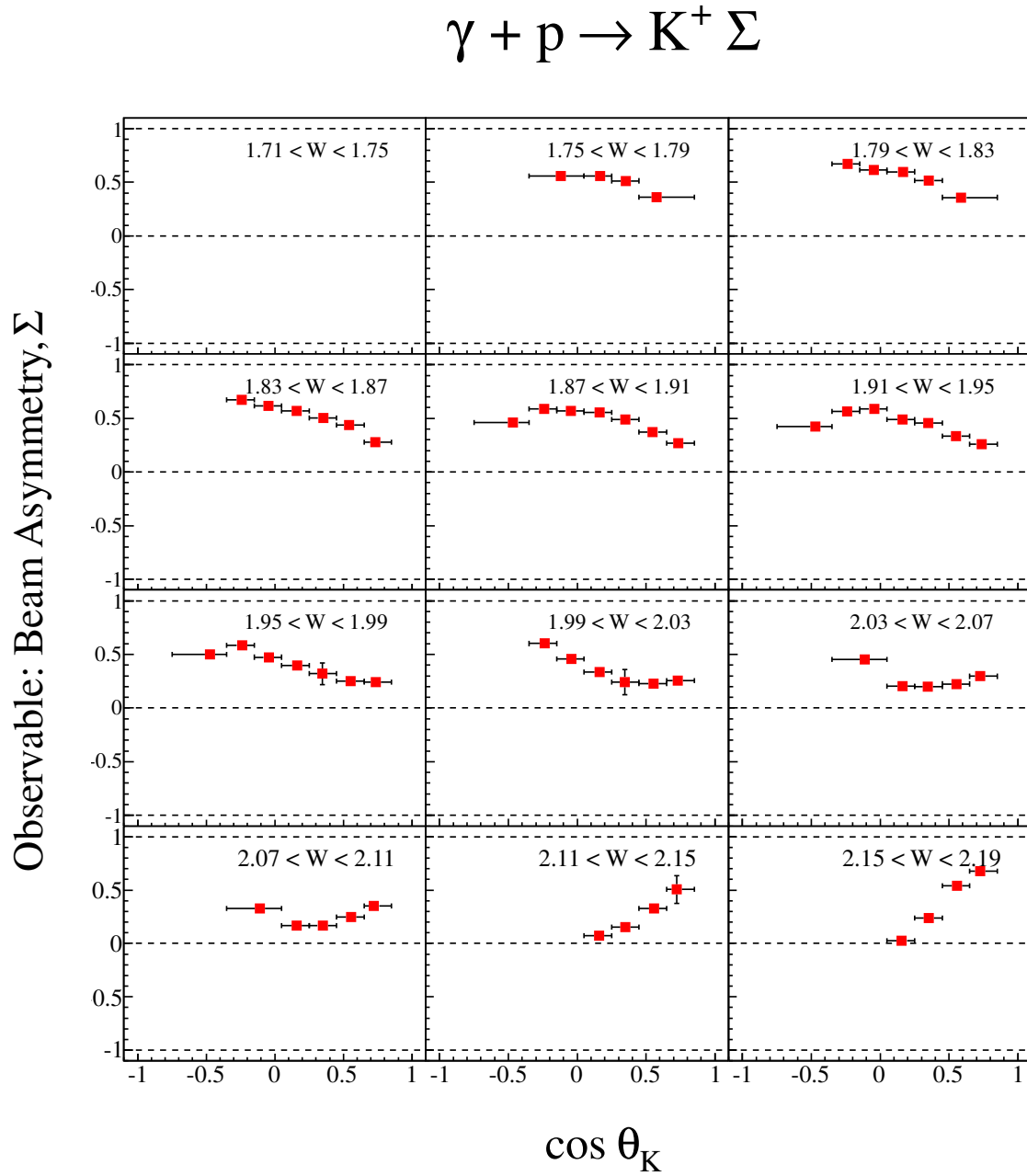
Figure 70. $\gamma p \to K^+\Sigma^0$ angular distributions of beam asymmetry Σ, for bins in W as labelled in each sub-plot.
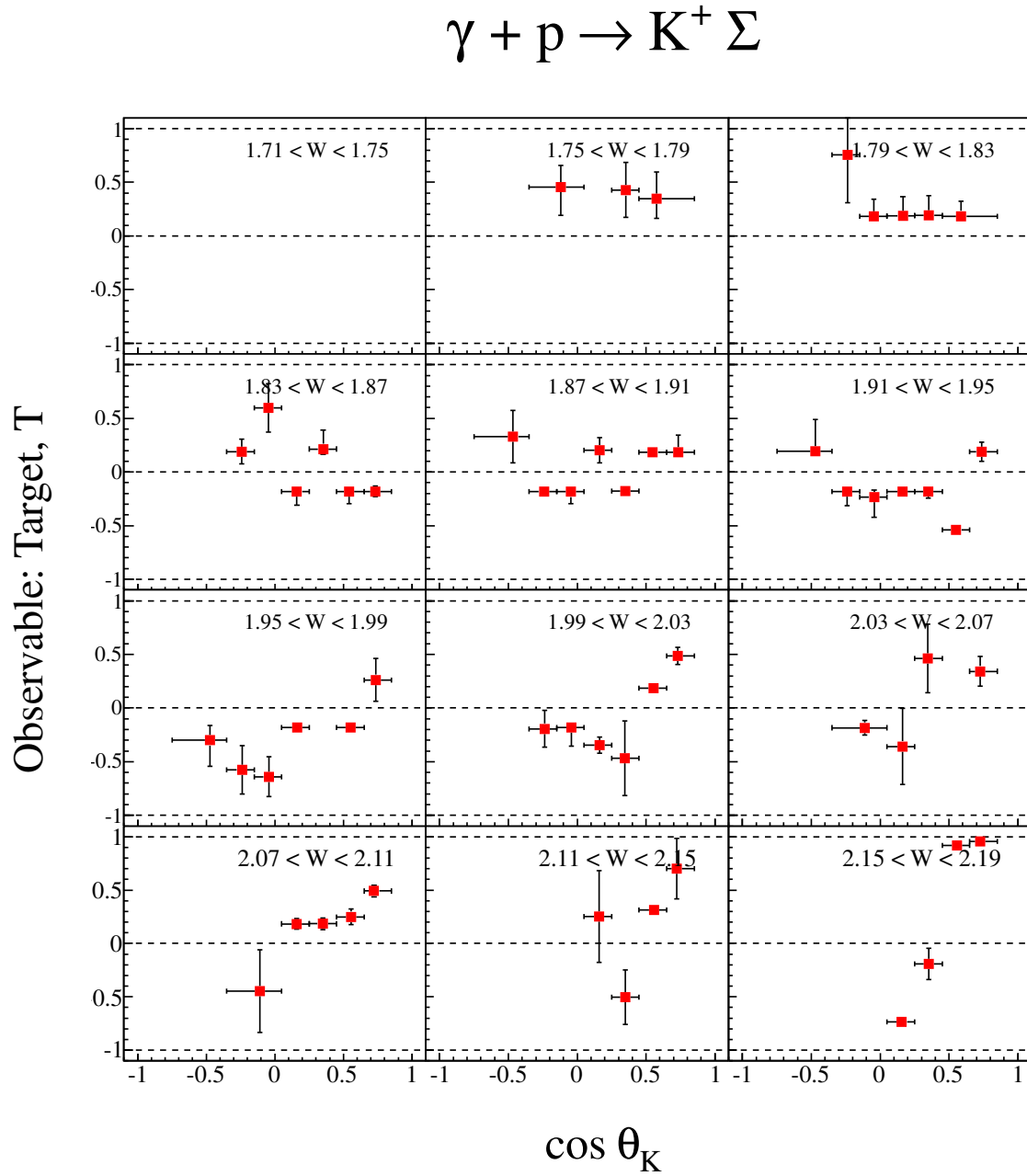
Figure 71. $\gamma p \rightarrow K^+\Sigma^0$ angular distributions of target asymmetry T, for bins in W as labelled in each sub-plot.
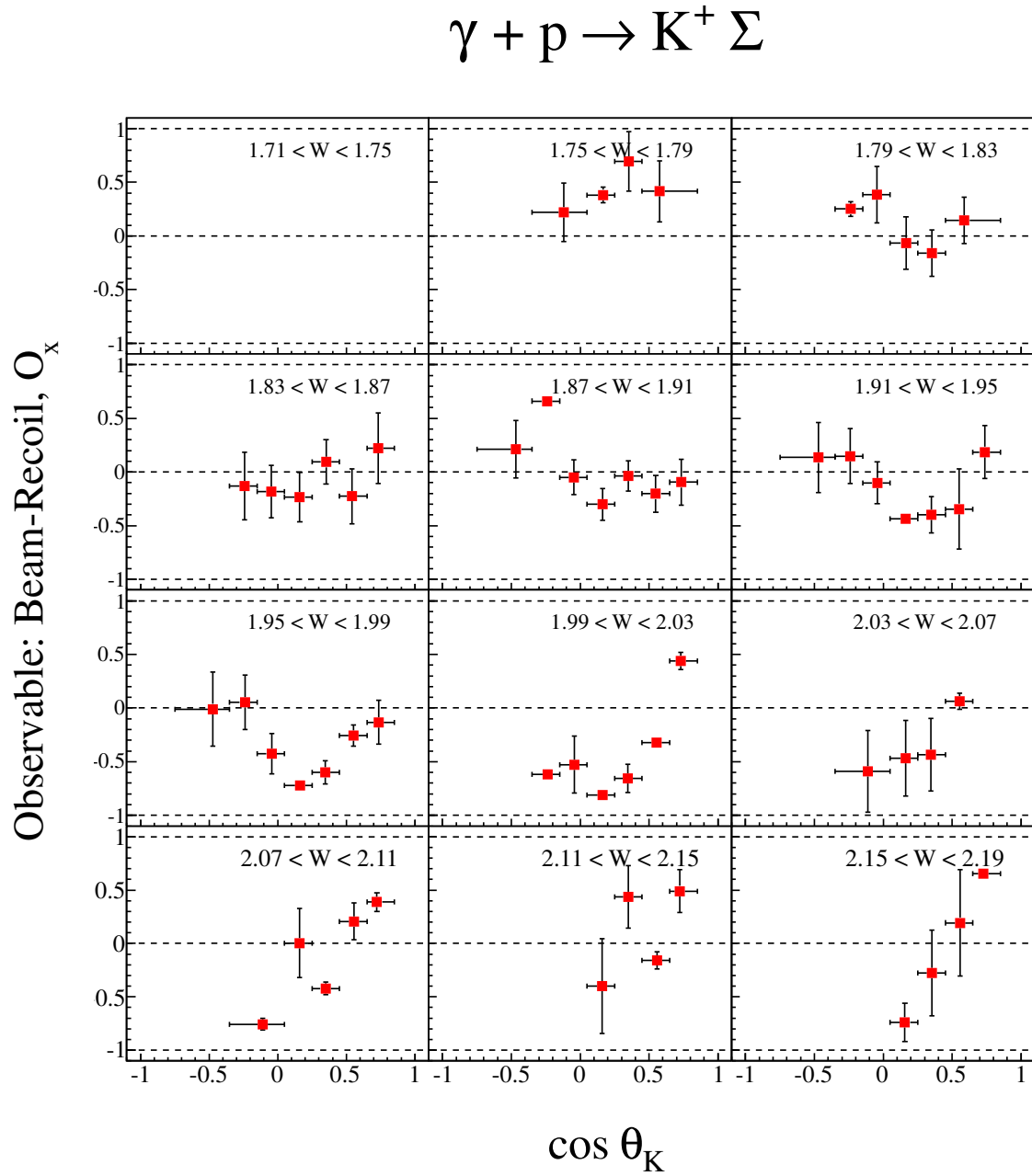
Figure 72. $\gamma p \to K^+\Sigma^0$ angular distributions of beam-recoil asymmetry O_x, for bins in W as labelled in each sub-plot.
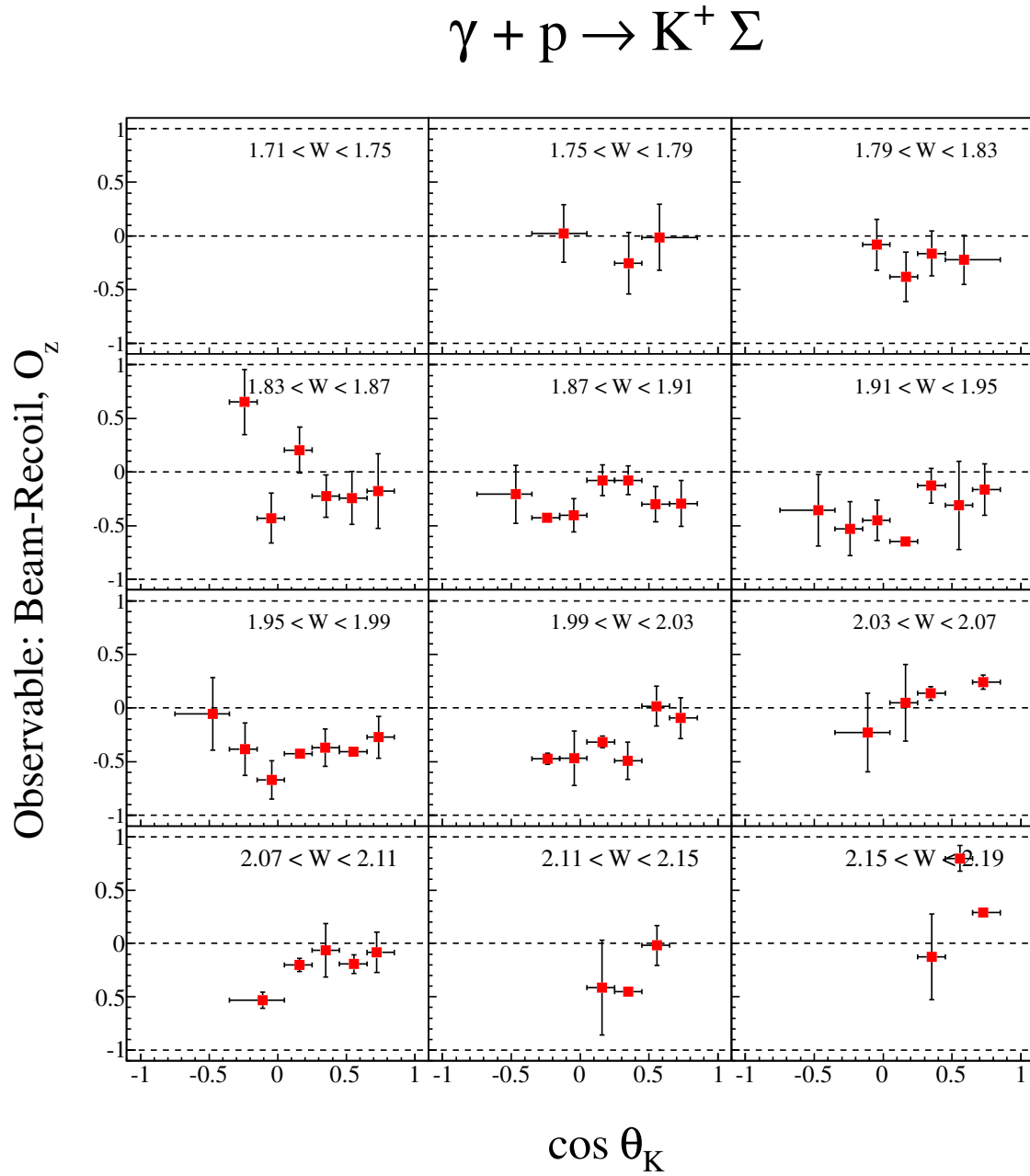
$$\gamma + p \rightarrow K^+ \Sigma$$

Figure 73. $\gamma p \rightarrow K^+\Sigma^0$ angular distributions of beam-recoil asymmetry O_z, for bins in W as labelled in each sub-plot.

$$\gamma + p \rightarrow K^+ \Sigma$$

Figure 74. $\gamma p \rightarrow K^+ \Sigma^0$ hadronic mass W distributions of beam asymmetry Σ, for bins in $\cos \theta_K$ as labelled in each sub-plot.

$$\gamma + p \rightarrow K^+ \Sigma$$

Figure 75. $\gamma p \rightarrow K^+ \Sigma^0$ hadronic mass W distributions of target asymmetry T, for bins in $\cos \theta_K$ as labelled in each sub-plot..

Figure 76. $\gamma p \to K^+\Sigma^0$ hadronic mass W distributions of beam-recoil asymmetry O_x, for bins in $\cos\theta_K$ as labelled in each sub-plot..
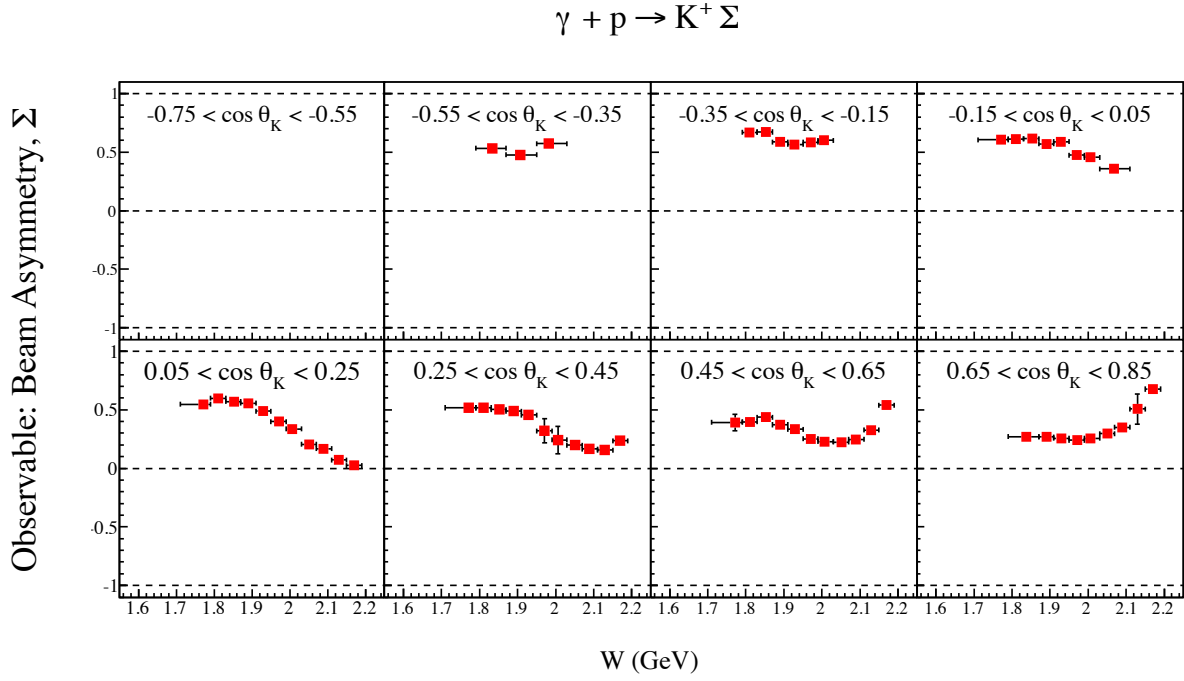

Figure 77. $\gamma p \to K^+\Sigma^0$ hadronic mass W distributions of beam-recoil asymmetry O_z, for bins in $\cos\theta_K$ as labelled in each sub-plot..
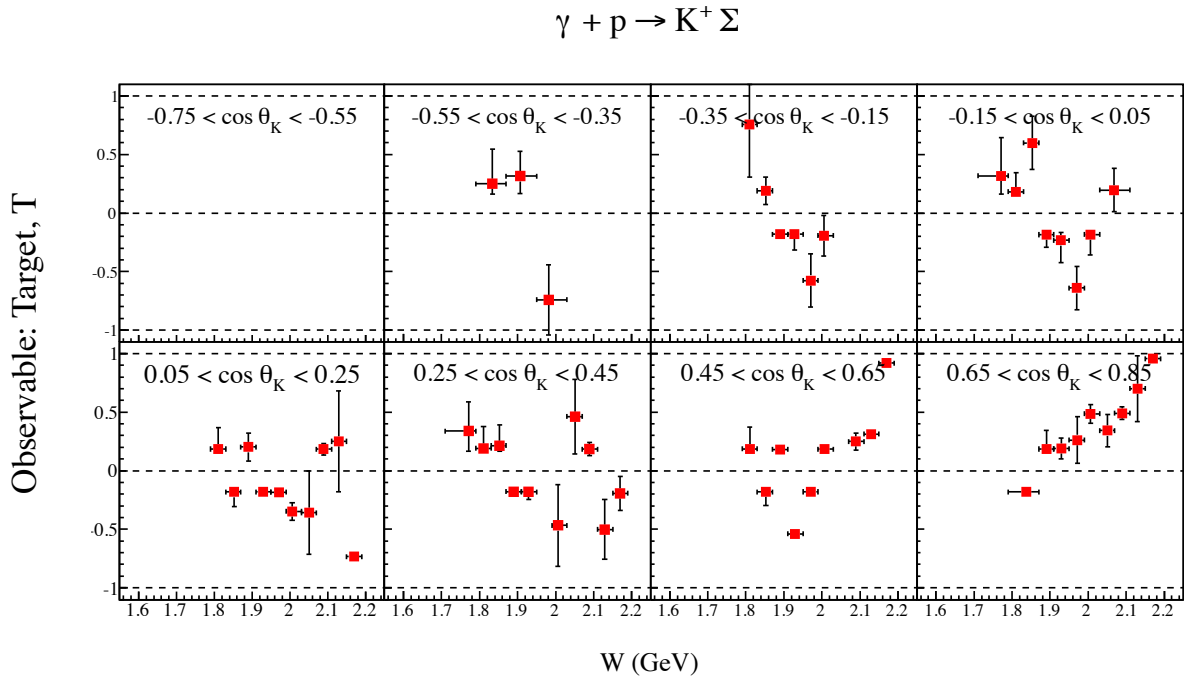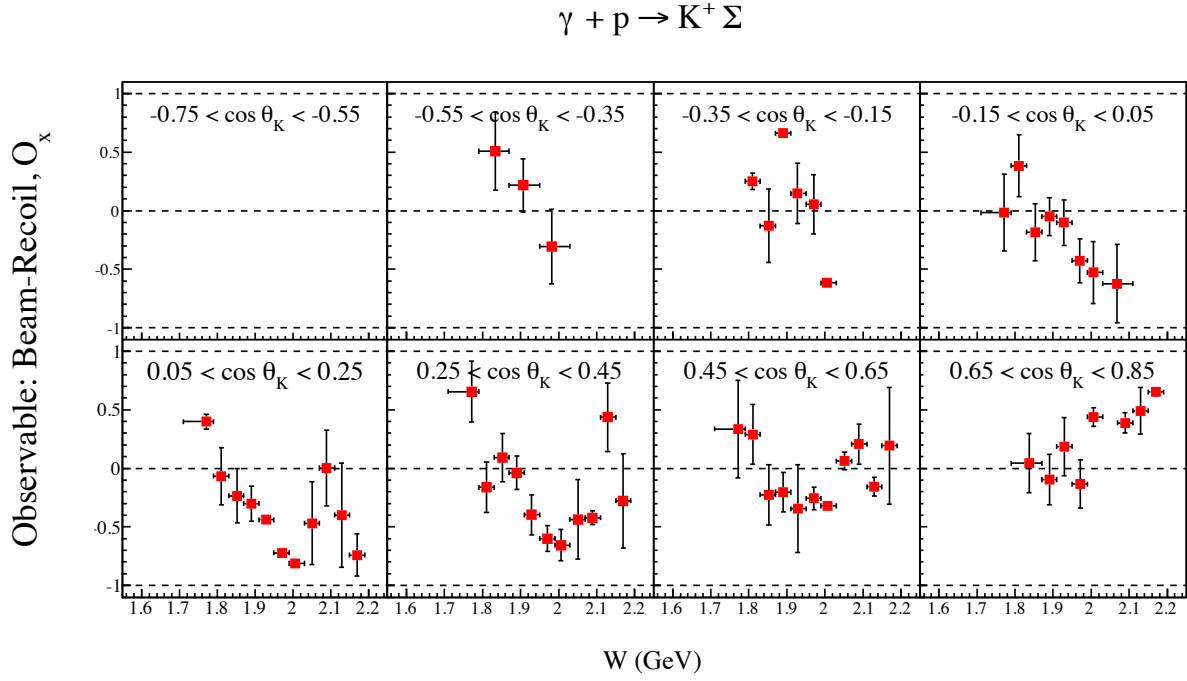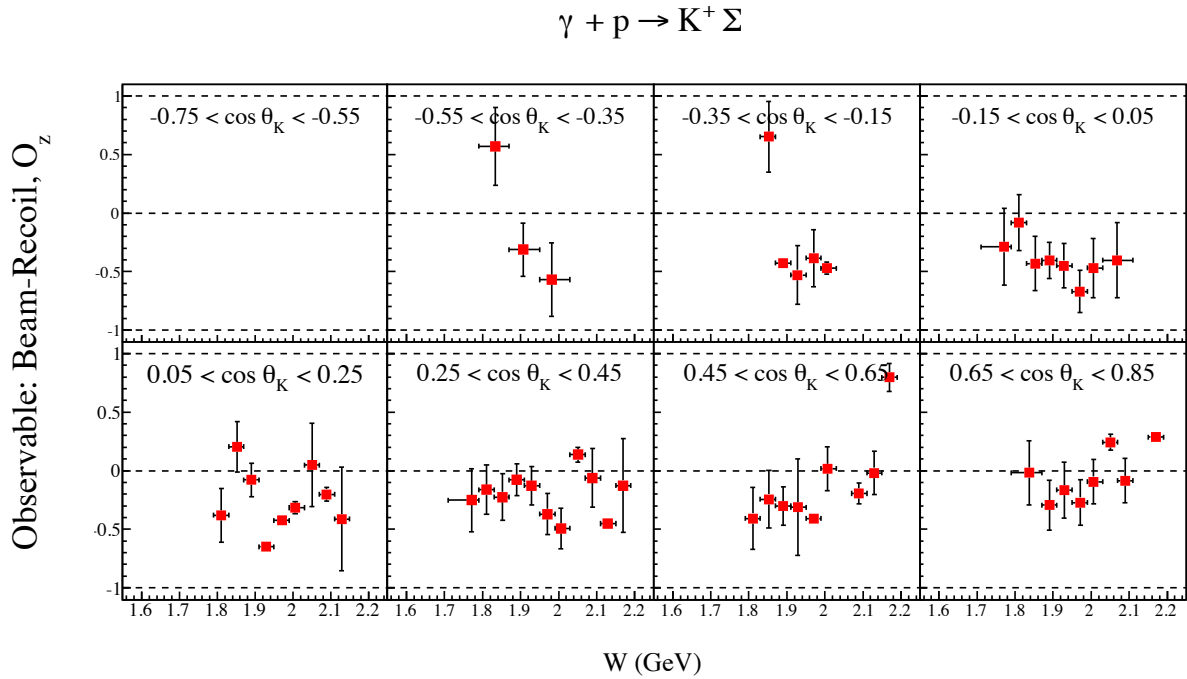
VIII.   CONCLUSION

Data from the g8b run period have been analyzed for the reactions $\vec{\gamma}p \rightarrow K^+\Lambda$ and $\vec{\gamma}p \rightarrow K^+\Sigma^0$. The polarization observables Σ, T, O_x and O_z have been extracted in an event-by-event likelihood analysis that guarantees consistency among observables, and is also consistent with previously published CLAS data on recoil polarization P from g11 data. For $\gamma p \rightarrow K^+\Lambda$ the W coverage is 1.71 - 2.19 GeV, and the $\cos\theta_K$ coverage is -0.75 - 0.85. For $\gamma p \rightarrow K^+\Sigma^0$ the W coverage is 1.75 - 2.19 GeV, and the $\cos\theta_K$ coverage is -0.55 - 0.85.

This analysis note is solely intended to describe the extraction of the experimental results. Physics interpretation and comparision with theoretical models will be carried out for draft papers.

1000   **Appendix A: Run Numbers**

1001   The following data runs are used in this analysis:

Peak (GeV)	Setting	Runs
1.3	PARA	48224, 48226, 48227, 48228, 48229, 48230, 48231, 48232, 48235, 48236, 48256, 48257, 48258, 48259, 48260, 48261, 48262, 48278, 48279, 48280, 48281, 48282, 48283, 48284, 48285, 48286, 48309, 48310, 48315, 48316, 48317, 48318, 48319, 48320
1.3	PERP	48240, 48241, 48245, 48246, 48247, 48248, 48249, 48250, 48251, 48268, 48270, 48271, 48272, 48273, 48274, 48276, 48292, 48293, 48294, 48295, 48296, 48297, 48298, 48323, 48326, 48327, 48328, 48329, 48330
1.5	PARA	48418, 48419, 48420, 48421, 48422, 48423, 48424, 48426, 48445, 48446, 48447, 48448, 48449, 48450, 48452, 48454, 48455, 48462, 48463, 48464, 48465, 48501, 48502, 48503, 48504, 48505, 48507, 48508, 48509
1.5	PERP	48431, 48432, 48433, 48434, 48435, 48436, 48437, 48438, 48439, 48440, 48441, 48442, 48443, 48444, 48466, 48467, 48469, 48477, 48478, 48479, 48482, 48483, 48484, 48485, 48486, 48487, 48488
1.7	PARA	48544, 48545, 48546, 48547, 48548, 48549, 48550, 48551, 48552, 48554, 48555, 48556, 48557, 48558, 48561, 48562, 48564, 48565, 48566, 48567, 48568, 48569, 48570, 48571
1.7	PERP	48580, 48581, 48582, 48583, 48584, 48585, 48586, 48587, 48588, 48589, 48590, 48591, 48592, 48593, 48595, 48596, 48597, 48598, 48599, 48601, 48602, 48603,48605, 48607, 48608, 48609, 48610, 48620, 48623, 48624, 48626, 48628, 48630

Table VIII. Run numbers used for the E_γ = 1.3, 1.5, and 1.7 GeV coherent peak settings.

Peak (GeV)	Setting	Runs
1.9	AUTO	48091, 48093, 48095, 48096, 48098, 48099, 48103, 48104, 48105, 48107, 48108, 48110, 48115, 48117, 48120, 48131, 48132, 48134, 48135, 48137, 48146, 48148, 48149, 48150, 48152, 48153, 48154, 48157, 48158, 48159, 48163, 48165, 48171, 48172, 48176, 48178, 48181, 48182, 48185, 48186, 48187, 48189, 48190, 48192, 48195, 48196, 48199, 48200
2.1	PARA	48357, 48358, 48359, 48360, 48361, 48362, 48363, 48364, 48365, 48387, 48388, 48392, 48393, 48394, 48395, 48396, 48397, 48399, 48400, 48405, 48406, 48407, 48408
2.1	PERP	48335, 48337, 48338, 48339, 48340, 48341, 48342, 48343, 48344, 48348, 48349, 48351, 48366, 48367, 48368, 48370, 48371, 48372, 48373, 48374, 48377
	Amorphous	48211, 48215-48217, 48237-48239, 48252-48254, 48265-48267, 48287, 48290, 48291, 48299, 48305, 48307, 48308 // 47923, 47927, 47931, 47935, 47939, 47945, 47946, 48413, 48414-48417, 48427-48429, 48456, 48460, 48461, 48489, 48492 // 47951, 47955, 47994, 48023, 48028, 48032, 48037, 48041, 48045, 48073, 48077,48083, 48528-48531, 48575, 48576, 48578, 48579, 48635, 48636, 48641-48643 // 48092, 48097, 48101, 48106, 48111, 48112, 48114, 48126, 48133, 48138, 48147, 48151, 48155, 48160, 48177, 48183, 48184, 48188, 48193, 48197 // 48352, 48355, 48381-48386

Table IX. Run numbers used for the E_γ = 1.9, and 2.1 GeV coherent peak settings, as well as the amorphous radiator runs.

1002   **Appendix B: Recoil Polarization**

1003   It was not the aim of this experiment to make a detailed measurement of recoil polar-
1004 ization. This has already been done with high precision in previous CLAS measurements
1005 [16, 17]. However, it is possible to extract P in the event-by-event likelihood method,
1006 which we do as part of the checks in the analysis by comparing with the previous mea-
1007 surements. This appendix outlines the additional considerations required.

1008   **1.   Acceptance Correction**

1009   As noted in section IV D, for event-by-event likelihood extraction, the recoil polariza-
1010 tion requires a distribution of intensities to be measured, as opposed to asymmetries. This
1011 means that an understanding of acceptance is necessary for this polarization observable
1012 only.

1013   A reaction with three particles in the final state, and a variable beam energy, is com-
1014 pletely described by six kinematic variables. The acceptance function is therefore a six-
1015 dimensional function. In the present case, the dynamics of interest are contained in dis-
1016 tributions in $\{W, \cos\theta_K\}$-space, so bins in these variables are chosen in which to extract
1017 the experimental observables, leaving four kinematic variables per bin. Now the reaction

$$\overrightarrow{\gamma} p \to K^+ \Lambda^0 \to K^+ p \pi^-$$

1018 is a series of two two-body reactions, since the hyperon has been identified in the missing
1019 mass of the kaon. The first two-body decay

$$\overrightarrow{\gamma} p \to K^+ \Lambda^0$$

1020 has only one independent variable (given $\{W, \cos\theta_K\}$). This could be taken to be ϕ_K. The
1021 subsequent decay

$$\Lambda \to p\pi^-$$

1022 is completely described by two further variables, which we could take as $(\cos\theta_P, \phi_P)$.
1023 Acceptance η can therefore be cast as a function of three measured (LAB) angles:

$$\eta = f\left(\phi_K, \cos\theta_P, \phi_P\right).$$

So from the original six variables, two define the bin in which observables will be determined, and a third is fixed because the hyperon is identified in the intermediate state.

The ideal method of correcting events for acceptance would be to calculate ratios of generated counts N_g to accepted counts N_a in small bins of the lab angles $\eta_i \, (\phi_K, \cos\theta_P, \phi_P)$, then divide events that fall in bin i by the ratio η_i. The bins have to be fine enough to allow for the "holes" in acceptance due to the magnet coils and other anisotropies. There is, however, a consequently sparse filling of bins, and it was found from initial trials that many events were not being accepted for two reasons:

1. Accepted events are smeared by GPP, which sometimes results in bins with no generated events having some accepted events.

2. The experimental data have not been subject to kinematic fitting beyond the identification of particles (i.e. setting masses to standard values and adjusting energy).

The latter problem is more severe, so one solution would be to project the acceptance in three variables $(\phi_K, \cos\theta_P, \phi_P)$ onto an acceptance in fewer variables. In doing this, for variable(s) of the experiment that is/are ignored, they are allowed to vary anywhere within the fiducial region, which is in effect a loosening of the kinematic constraint of overall energy-momentum conservation.

To study this effect, a typical photon energy bin ($1.5 < E_\gamma < 1.6$ GeV) was selected, as well as three Kaon scattering angle bins (forward, mid- and backward). The data were binned into $\cos\theta_y$ distributions (Λ rest frame) and fitted with a straight line to extract values of Recoil Polarization. The weighting given to each event in forming the $\cos\theta_y$ distributions was done in several different ways:

1. Uncorrected: Simply a straight filling of the $\cos\theta_y$ histogram with acceptance correction.

2. $\cos\theta_y$: Taking the acceptance ratios from the generated and accepted $\cos\theta_y$ distributions. Since $\cos\theta_y$ is a function of $(\phi_K, \cos\theta_P, \phi_P)$, this represents an effective smearing of kinematics over two variables.

3. $\cos\theta_p, \phi_p$: Smearing over ϕ_K.

4. ϕ_p, ϕ_K: Smearing over $\cos\theta_p$.

Correction		$0.4 < \cos\theta_K < 0.5$			$-0.05 < \cos\theta_K < 0.05$			$-0.5 < \cos\theta_K < -0.4$		
		Value	Error	Total χ^2	Value	Error	Total χ^2	Value	Error	Total χ^2
Uncorrected	1	-0.402	0.025	74.8	0.084	0.036	15.9	0.743	0.057	11.5
$\cos\theta_y$	2	-0.380	0.038	13.0	0.102	0.049	7.28	0.781	0.073	14.9
$\cos\theta_p, \phi_p$	3	-0.367	0.016	254.4	-0.005	0.021	61.2	0.656	0.022	231.1
ϕ_p, ϕ_K	4	-0.260	0.014	2508.5	0.104	0.019	449.0	0.744	0.020	65.4
$\phi_K, \cos\theta_p$	5	-0.419	0.015	347.6	0.039	0.021	61.0	0.704	0.021	227.9
ϕ_K	6	-0.425	0.013	336.4	0.046	0.018	114.5	0.758	0.019	117.5

Table X. Variations in Recoil Polarization for three different Kaon scattering angles ($1.5 < E_\gamma < 1.6$ GeV)

5. $\phi_K, \cos\theta_p$: Smearing over ϕ_p.

6. ϕ_K: Smearing over $\cos\theta_p$ and ϕ_p.

The results are summarized in table X. What is clear is that there is a spread of results, depending on which acceptance ratio is used. This spread has a standard deviation of about 0.04. If we use one of these methods, therefore, the results are likely to be subject to a systematic error of about 0.04. The total χ^2 of several results indicates that some of the corrected histograms were not well described by a straight line, and therefore that the simulation is missing some subtleties of the detector response during the g8b run period.

We choose to employ the crudest correction (2), which uses the ratio of generated and accepted $\cos\theta_y$ distributions. The error on the extracted values is larger than any of the other methods, but it is of the same size as the estimated systematic uncertainty, and the quality of fit is superior.

Implementing the acceptance correction

For unbinned likelihood fitting, each event is weighted by the ratio N_g/N_a for the *kinematic* $\cos\theta_y$ bin in which the event falls (acceptance is not done event-by event). Here N_g is the number of generated events in the bin, whereas N_a is the number of accepted events in that same bin. We only allow acceptance ratios that meet the following conditions:
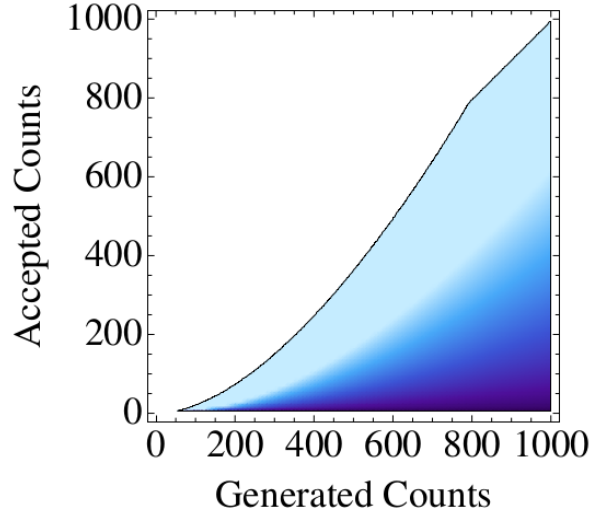
Figure 78. Shaded region that shows acceptable combinations of generated and accepted numbers of simulated events.

1. $N_a > 5$; $N_g - N_a > 5$: These are equivalent to the conditions for a binomial distribution to be approximated by a normal distribution.

2. $N_a/N_g > 0.05$: A possibly redundant condition that ensures the event is in the fiducial region.

3. $\frac{1}{N_g^2}\left(N_g N_a \left(N_g + N_a\right)\right)^{\frac{1}{2}} < 0.05$: This is the error on the acceptance ratio (assuming normal distributions). We make the cut off (arbitrarily) 5%, since this is still below the systematic uncertainty as described above.

Figure 78 illustrates conditions 1 and 3. The shaded region corresponds to the combinations of generated and accepted numbers of simulated events. The minimum required number of generated events in a bin is about 50, while the restriction on the number of accepted events is bounded by the lower limit of 5, and the number imposed by the minimum error on the ratio (condition 3).

For binned fitting, the experimental $\cos\theta_y$ histogram is multiplied by the simulated, generated $\cos\theta_y$ histogram and divided by the simulated, accepted $\cos\theta_y$ histogram, and a straight line fit is applied to the result.

A description of the extraction of recoil polarization, and comparison with previous data is given in section V A.

[1] CLAS, R. Bradford *et al.*, Phys. Rev. **C75**, 035205 (2007), nucl-ex/0611034.

[2] K. Livingston, Clas note 2006-022: Running the linearly polarized photon beam.

[3] K. Livingston, The rootbeer software package.

[4] M. Dugger and C. Hanretty, Clas note 20009-030: Correction to the incident photon energy for g8b data, 2009.

[5] E. Pasyuk, Clas note 2007-016: Energy loss corrections for charged particles in clas, 2007.

[6] U. Timm, Fortschritte Phys. **17**, 765 (1969).

[7] D. Lohmann *et al.*, Nucl. Instr. and Meth. A **343**, 494 (1994).

[8] K. Livingston, Clas note 2011-020: Polarization from coherent bremsstrahlung enhancement.

[9] K. Livingston, N. Zachariou, and M. Anderson, Clas note in preparation: Determining the degree of polarization for linearly polarized photons at clas.

[10] M. Dugger and B. Ritchie, Clas note 2011-02: Consistency corrections to the linear photon polarization for g8b data.

[11] M. Dugger *et al.*, Clas analyis note: Extraction technique for sigma and g for pseudoscalar meson photoproduction.

[12] B. Dey, M. E. McCracken, D. G. Ireland, and C. A. Meyer, Phys. Rev. C **83**, 055208 (2011).

[13] D. G. Ireland, CLAS Note Report No. 2011-010, 2011-010 (unpublished).

[14] K. Livingston, Clas note 2012-010: Binned fitting techniques for measuring photon beam asymmetry.

[15] X. Artru, J.-M. Richard, and J. Soffer, Phys. Rev. **C75**, 024002 (2007), nucl-th/0606050.

[16] M. E. McCracken *et al.*, Phys. Rev. C **81**, 025201 (2010).

[17] B. Dey *et al.*, Phys. Rev. C **82**, 025202 (2010).

[18] R. G. T. Zegers *et al.*, Phys. Rev. Lett. **91**, 092001 (2003).

[19] A. Lleres *et al.*, The European Physical Journal A - Hadrons and Nuclei **31**, 79 (2007), 10.1140/epja/i2006-10167-8.

[20] A. Lleres *et al.*, The European Physical Journal A - Hadrons and Nuclei **39**, 149 (2009), 10.1140/epja/i2008-10713-4.

[21] A. M. Sandorfi, S. Hoblit, H. Kamano, and T.-S. H. Lee, Journal of Physics G: Nuclear and Particle Physics **38**, 053001 (2011).